九州大学学術情報リポジトリ
Kyushu University Institutional Repository

Electrochemical Characterization of Novel Cathode Active Materials for Sodium-ion Battery

智原, 久仁子

https://hdl.handle.net/2324/1807080

出版情報：九州大学, 2016, 博士（工学）, 課程博士
バージョン：
権利関係：

Electrochemical Characterization of Novel Cathode Active Materials for Sodium-ion Battery

(ナトリウムイオン電池用新規正極活物質の電気化学特性)

CONTENTS

List of Figures and Table

CHAPTER 1.

CHAPTER 2.

Figure 10. (a) The charge and discharge profiles and (b) cycle performance of $Na_3V_2(PO_4)_2F_3$ with the different charge cutoff voltage of 4.6, 4.3 and 4.1 V with 2.3 V discharge. (c) The charge and discharge profiles and (d) cycle performance of $Na_3V_2(PO_4)_2F_3$ with the different charge cutoff voltage of 4.6, 4.3 and 4.1 V with 1.0 V discharge.

Figure 11. XRD profiles of the (a) initial and 15^{th}-cycled $Na_3V_2(PO_4)_2F_3$ electrodes with cycles between (b) 4.1 - 2.3 V, (c) 4.3 - 2.3 V and (d) 4.6 - 2.3 V.

Figure 12. Rate performance of $Na_3V_2(PO_4)_2F_3$. Discharge rate was changed from 0.2 to 10 C and the charge current rate in the corresponding cycle was (a) fixed at 0.2 C and (b) changed from 0.2 to 10C.

Figure 13. Charge and discharge profiles of $Na_{3-x}V_2(PO_4)_3$ and $Na_{1+x}Ti_2(PO_4)_3$ in Na cells.

Figure 14. Charge and discharge profiles of $Na_{3-x}V_2(PO_4)_3$ and hard carbon in Na cells.

Figure 15. (a) The charge and discharge profile of $Na_{3-x}V_2(PO_4)_2F_3/Na_{1+x}Ti_2(PO_4)_3$ Na-ion cell on 1^{st} and 2^{nd} cycles. (b) Cycle performance of $Na_{3-x}V_2(PO_4)_2F_3/Na_{1+x}Ti_2(PO_4)_3$ Na-ion cell.

Figure 16. Charge and discharge profile of $Na_{3-x}V_2(PO_4)_2F_3$/Hard carbon Na-ion cells on 1^{st} and 2^{nd} cycles with different electrolyte of (a) 1 M $NaPF_6$/EC:DEC

CHAPTER 3.

XRD, FT-IR, ^{23}Na and ^{13}C MAS-NMR. (I) - (III), (I), (IV) and (VI) – (X) are for XRD, (I) and (VII) – (X) are for FT-IR, and (V) - (X) are for MAS-NMR.

Figure 37. *Ex-situ* XRD patterns of $Na_2C_6O_6$ at the state of (a) initial, (b) discharge for 1 Na^+ insertion, (c) 1st discharge down to 1.8 V, (d) discharge down to 1.5 V, (e) 1st charge up to 2.9 V, (f) 2nd discharge down to 1.5 V and (g) 2nd charge up to 2.9 V.

Figure 38. FT-IR peak change behaviors for $Na_2C_6O_6$ at the state of (a) powder, (b) initial (c) 1st discharge down to 1.5 V, (d) 1st charge up to 2.9 V, (e) 2nd discharge down to 1.5 V and (f) 2nd charge up to 2.9 V.

Figure 39. ^{13}C NMR spectrum for $Na_2C_6O_6$ at the state of (a) powder, (b) initial, (c) 1st discharge down to 1.8 V, (d) 1st discharge down to 1.5 V, (e) 1st charge up to 2.9 V, (f) 2nd discharge down to 1.5 V and (g) 2nd charge up to 2.9 V. (Inset) peak assignment on $C_6O_6^{2-}$ anion of $Na_2C_6O_6$.

Figure 40. ^{23}Na solid NMR spectrum for $Na_2C_6O_6$ at the state of (a) initial, (b) discharge for 0.25 Na^+ insertion, (c) discharge for 0.5 Na^+ insertion (d) discharge for 1.25 Na^+ insertion, (e) 1st discharge down to 1.8 V, (f) 1st discharge down to 1.5 V, (g) 1st charge up to 2.9 V, (h) 2nd discharge

down to 1.5 V and (i) 2nd charge up to 2.9 V.

Figure 41. ^{23}Na MQMAS NMR spectrum for the $Na_2C_6O_6$ samples after being discharged (a) for 1.25 Na and (b) down to 1.5 V.

Figure 42. ^{23}Na NMR spectrum of discharged $Na_2C_6O_6$ sample for 1.25 Na. The sample was (a) measured immediately after dissembling a cell, and left for (b) 1, (c) 2 and (c) 3 weeks in Ar glove box and measured in Ar condition, and (e) exposed in the air and measured in Air condition.

Chapter 1. General Introduction

1.1. Background on lithium-ion and sodium-ion batteries

An electric battery is a device consisting of single or interconnected multiple cell(s) and provides power to electrical devices including consumer electronics and industrial equipment. The battery is connected to these devices on positive and negative terminal points to make an external circuit, supplying electric energy converted from chemical reaction on both terminals. The cell generally composes two electrodes facing at opposite sites; an anode at the negative terminal and a cathode at the positive terminal, and these electrodes are separated by conductive electrolyte containing salt dissolved in a solvent. The batteries are mainly classified into two groups according to their electrochemical reversibility; primary and secondary forms. Since the chemical energy irreversibly transforms to electrical energy in a primary battery system, the primary battery is not rechargeable and discarded after being discharged once. While, a secondary battery is capable to repeatedly convert the electrical energy to the chemical energy with charge supply of electric current, and hence the battery is able to be discharged to reuse multiple times.

The history of rechargeable battery has started from the invention of lead-acid batteries introduced by Gaston in 1859, and a lithium-ion battery has become a common replacement for them due to its highest energy density among commercialized secondary batteries (Table 1). Concept of a lithium-insertion material was first proposed by Exxon in the mid 1970's using TiS_2 as cathode and lithium metal as anode materials. This type of batteries are generally called as lithium batteries.[1] They stand for high voltage and large energy density due to lowest electrode potential of Li metal, and numbers of researches had been exploded to develop new type of high energy batteries. A variety of

cathodes and electrolytes can be used in the lithium battery system but all with metallic lithium as the anode. The technology of the lithium battery has been realistic in the primary system, however there ware safety problems as the secondary batteries. The metallic lithium anode leads safety issue due to its reactivity against moisture and air, and in the worst case, causes explosion and fire in normal atmospheric conditions. In 1980, John Goodenough and Koichi Mizushima discovered repeatable Li de/insertion from/into lithium cobalt oxide, $LiCoO_2$, and demonstrated a rechargeable lithium cell with a voltage in the 4 V range. [2]. $LiCoO_2$ is a stable material in air and serves as a donor of lithium ions, making it possible to assemble a cell with a negative electrode material other than lithium metal. Their works represented a first step toward realization of lithium batteries without using reactive metallic lithium. In following years, lithium deinsertion/insertions into ternary lithium-copper-oxygen system were demonstrated by Godshall et al. [3], and Michael M. Thackeray and his coworkers further developed manganese spinels. [4] As for anode materials, the reversible electrochemical intercalation of lithium in graphite were also confirmed with using solid electrolyte. [5] In 1985, Akira Yoshino demonstrated a prototype lithium-ion cells consisting of a carbonaceous material as an anode and $LiCoO_2$ as a cathode to introduce them as a safe and high energy secondary battery, and his invention has been an origin of current commercialized lithium-ion batteries in the world wide. [6] After Sony and Asahi Kasei released the first commercial lithium-ion battery in 1991, rechargeable Li-ion batteries (LIBs) have been used in portable electronic devices as the most popular energy storage technology.

Table 1. List of major commercialized primary and secondary batteries. [7]

Primary battery						
	Anode	**Cathode**	**Released year**	**Average V**	**by mass (Wh kg^{-1})**	**by volume (Wh L^{-1})**
Zinc battery	Zn	Carbon	1898	1.5	36	92
Zinc-air	Zn	Oxygen	1932	1.45-1.65	442	1673
Alkaline	Zn	MnO_2	1949	1.5	85-190	250-434
Lithium battery	Lithium metal	MnO_2	1976	3	150-330	300-710
		Li-(CF)	1976	3	260-780	440-1478
Secondary battery						
	Anode	**Cathode**	**Released year**	**Average V**	**by mass (Wh kg^{-1})**	**by volume (Wh L^{-1})**
Lead-acid	Pb	PbO_2	1881	2.1	30 - 40	60 - 75
Nickel-hydrogen	Hydrogen		1975	1.55	45-65	60
Nickel-metal	Metal	$Ni(OH)_2$	1990	1.2	100	401
Lithium ion battery	Graphite or $Li_4Ti_5O_{12}$	$LiCoO_2$	1991	3.7	195	560
		$LiFePO_4$	1996	3.2	90-130	333
		$LiMn_2O_4$	1999	3.9	150	420
		$LiNiCoAlO_2$	1999	3.6	220	600
		$LiNiMnCoO_2$	2008	3.6	205	580

The electrochemical reactions in LIBs take place on the negative and positive electrode sides, and lithium ions move between the two electrodes through a conductive electrolyte medium. The driving force of the Li^+ ion mobility is redox (oxidation and reduction) reaction of transition metals, and the redox reaction occurs when electrons flow through a closed external circuit.

For example, reaction equations between the $LiCoO_2$ cathode and graphite (C) anode are described as follows;

The reaction on cathode:

$$Li_{(1-x)}CoO_2 + xLi + x e^- \leftrightarrow LiCoO_2$$

The reaction on anode:

$$xLiC_6 + x e^- \leftrightarrow xLi + x e^- + xC_6$$

The overall reaction:

$$Li_{(1-x)}CoO_2 + xC_6 \leftrightarrow LiCoO_2 + xLiC_6$$

Figure 1 shows the diagram of LIBs. In the charging process, Li^+ ions are extracted from a positive electrode material to move into a negative electrode material, and the ions on the negative side move back to the positive side during following discharge process.

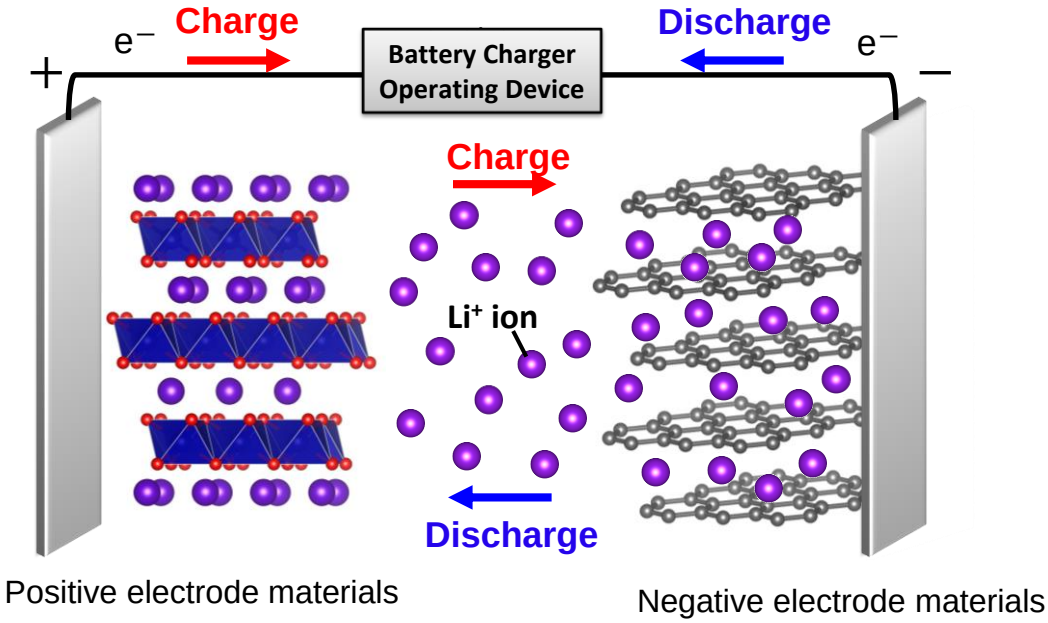

Figure 1. Schematic description of lithium-ion batteries.

Nowadays, the application fields of LIBs have been expanding to larger scale devices such as electric vehicles (EVs) and a smart grid system due to its high energy density, low memory effects, and long cycle life requiring less maintenance. These movement has been considered as a viable solution to take a step toward more environmentally friendly society, and regarded to be truly helpful for relieving energy crisis and global energy gap between countries. Under this circumstances, tremendous amount of researches have been conducted to introduce LIBs into the systems to advance clean energy technologies. However, when the energy storage system gains in popularity, cost performance becomes a more dominant factor rather than electrochemical performance, and hence, inexpensive batteries, which can be derived from low cost and abundant materials, become more and more desirable. Lithium resource are not uniformly distributed within the Earth's crust. As a result, the increasing demand for lithium associated with new and large-scale applications raises future concern on the price of lithium as well as even political conflict on lithium reserves. Rechargeable sodium-ion batteries (SIBs) have been, therefore, actively studied for the past few years and recognized as an alternative candidate to LIBs due to the abundant reserves and even-distribution of Na resources.

Table 2 shows cost and atomic weight of Li and Na. As for lithium resources, there is no Li reserve bases in Japan, and hence we have to completely rely on import from other countries in South America region and China etc.. On the other hand, sodium resources is available everywhere, and technology to produce chemical raw material of caustic soda and sodium carbonate has been established in Japan since 1880's. The abundance of sodium resources and the much lower production cost leads a rationale idea to use SIBs as an alternative to LIBs. [7] In addition, since sodium-aluminum alloy dose not form in sodium cells, aluminum can be used as current collectors instead of expensive copper

foils for both cathode and anodes, leading additional cost reduction.

Table 2. Cost and atomic weigh of lithium and sodium. [8]

	Lithium	Sodium
Cost of carbonate salt	5,000 \$ t^{-1}	150 \$ t^{-1}
Atomic weight	6.9 g mol^{-1}	23 g mol^{-1}

A cathode material for SIBs was first proposed by the Delmas group in parallel with the development of LIBs between 1970's and 1980's. [9] A few Japanese companies actually developed SIBs in full cell configurations before the commercialization of LIBs, where a sodium-lead alloy composite and a P2-type Na_xCoO_2 were used as the anode and cathode, respectively. [10] Although SIBs fell into the shadow of great commercial success of LIBs, they have reserved gained attention 30 years after the research on electrochemical de/sodiation in Na_xCoO_2. [9] SIBs have been developed rapidly for the recent past few years, because electrical storage mechanism of SIBs and LIBs are basically the same except ion carriers and the intercalation chemistry of sodium can be discussed based on that of lithium. [11] The technology and knowledge developed in LIBs facilitates the development of SIBs. However, the ion size of Na^+ is 1.02 Å and much larger than that of Li^+ ion with 0.76 Å, which affects phase stability, transport properties, and interphase formation. As show in table 3, sodium are also heavier than lithium and have higher standard electrode potential; thus, SIBs would be always less attractive in terms of energy density compared to LIBs.

Table 3. Physical property of lithium vs. sodium. [8]

	Ionic Volume	Theoretical Capacity	Standard Electrode Potential
Li	1.84 $Å^3$	3,829 mAh g^{-1}	−3.045 V
Na	4.44 $Å^3$	165 mAh g^{-1}	−2.714 V

Various cathode materials for SIBs have been reported such as layered transition metal oxides, transition metal sulfides and fluorides, oxyanionic compounds, prussian blue analogues, and organic carboxylates and polymers. On the other hand, there are not many materials proposed as an anode for SIBs. Hard carbons is the most promising anode candidate for SIBs with large reversible capacity with long cycle life, and they delivers 200 to 300 mAh g^{-1} with the working voltage close to Na/Na^+. [12]

1.2. Inorganic cathode materials for SIBs

1.2.1. General information

One would easily come up with ideas that cathode materials for SIBs can be explored based on the knowledge developed in LIBs, however established cathode materials for LIBs such as $LiCoO_2$ and $LiFePO_4$ [13] cannot be simply applied to the sodium system. For example, continuous structural evolution is normally observed during Na^+ ion de/intercalation or de/insertion from/into a host structure as step-wise charge/discharge profiles probably due to the large Na^+ ion-size.

Na^+ ion-size is considered to have impact on resultant electrochemical performance, and hence cathode materials for SIBs have to have a structure capable to accept large sodium extraction and insertion. The reported cathode active materials with relatively

large capacity for SIBs are mainly categorized to some special material groups with two- and three-dimensional open structures. These materials are obtained as oxides, polyanions of phosphate, pyrophosphase, fluorosulfates, and NASICON (Na super ionic conductor) types, and organic compounds. Figure 2 summarizes the energy density map of SIBs consisting of representative reported inorganic cathode materials based on hard-carbon anodes. The highest energy density of the layered tradition metal oxide reaches to 300 mhA g^{-1} which is equal to the value obtained from $LiMn_2O_4$. As seen in the density map, layer tradition metal oxides and vanadium- or iron-based polyanion compounds show relatively good electrochemical performance with large discharge capacity.

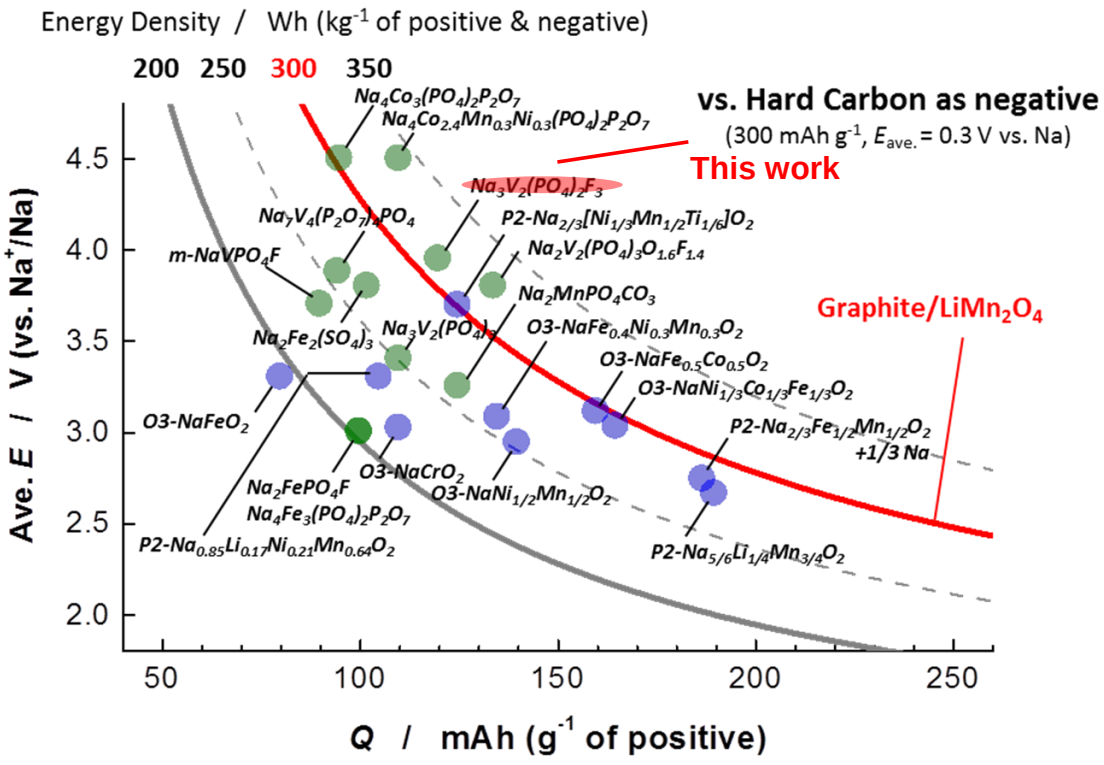

Figure 2. Energy density map of sodium-ion batteries consisting of representative positive materials with hard-carbon anodes.

1.2.2. Two-dimensional layer transition metal oxides cathode

The history of two-dimensional layer oxides in the sodium system can be traced back to the research on sodium de/intercalation into Na_xCoO_2 demonstrated by Delmas in the early 1980s. [9, 14] In accordance with the Delmas' notation [15], the crystal structure of layered oxides can be categorized based on MO_6 (M: transition metal) octahedral stacking manner along with *c*-axis. For example, the structure of $Na_{1-x}MO_2$ are divided into two main groups such as O3 type and P2 type as show in Figure 3. Edge-sharing MO_6 octahedrons form layers between which Na^+ ions are inserted in an octahedral (O) or prismatic (P) environment. The number after octahedral (O) or prismatic (P) indicates the packing number of Na octahedral or prismatic layers within each unit cell. In addition, their polymorphs with in-plane distortion are distinguished by adding a prime symbol (').[16,17] The O3 type is relatively stable throughout cycles and Na^+ in $Na_{1-x}MO_2$ is able to be repeatedly extracted and inserted between $0<x<1$. The O3 structure, hence, reversibly transform O3 ↔ O'3 ↔ P3 ↔ P'3 during electrochemical de-/sodiation. With increased desodiation, Na^+ ions energetically favor a prismatic environment, which leads transformation to P3 from O3 and creates Na^+ vacancies. This extraction induces strong repulsion between oxygen Na layers, and the interlayer distance thus expands. Hence, Na^+ diffusion becomes faster in the P'3 phase compared to O3. [9] The P2 type has Na vacancies in the structure, leading strong repulsion from oxygen in the Na layers. As a result, interlayer distance expands to create two different Na prismatic sites. The structure is usually stable as long as the Na content is in the range of 0.3 - 0.7 in $Na_{1-x}MO_2$. The P2 phase is maintained up to $Na_{0.46}MO_2$. The P2 phase transforms towardO2 by further desodiation due to gliding of the MO_6 octahedra, reducing interlayer distance. Na amount in the structure brings distortion and vacancy, resulting in diverse transformation during

cycles, and it is consider to impact on overall electrochemical property. Recently, Kumakura et al. have investigated electrochemical difference between P2- and P'2-$Na_{2/3}MnO_2$ with successful phase separation in P2- and P'2-phases under the strictly controlled synthetic condition. They found that strongly distorted P'2-$Na_{2/3}MnO_2$ delivers better electrochemical performance than that of non-distorted P2-$Na_{2/3}MnO_2$. [19] The P2-phase maintains during Na^+ extraction with charge up to 4.4 V, while the P'2-phase transforms to a PO4 phase through P'2-I as involving with four sub-phase transformations due to interaction between Na/vacancy and $Mn^{III/IV}$ charge orderings. As expected from their initial structural features, P'2-$Na_{2/3}MnO_2$ exhibits stepwise charge profiles due to phase transformation, and P2-$Na_{2/3}MnO_2$ shows smooth charge and discharge profiles. They have suggested that Mn defect influences electrochemical performance rather than distortion due to co-operative Jahn–Teller distortion (CJTD). Their funding also implies the phase transformation due to Na^+ insertion and extraction is not a direct factor to determine the electrochemical performance.

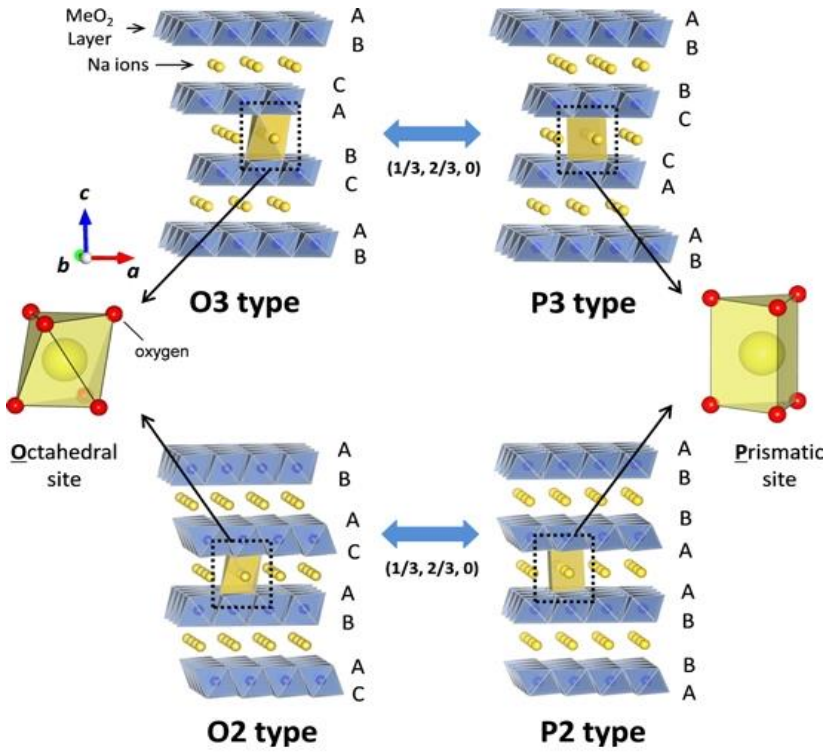

Figure 3. Phase evolution of Na–Me–O layered materials with the sheets of edge-sharing MeO_6 octahedra. [18] *

*Reprinted from N. Yabuuchi, S. Komaba, Science and Technology of Advanced Materials, Review, Copyright (2014) with permission from pro. Komaba in Tokyo university of science.

1.2.3. Three-dimensional polyphosphate compounds cathode materials

Iron phosphate positive material - maricite and olivine type $NaFePO_4$

Generally speaking, structures made up covalently bonded PO_4 and MO_6 (M = tradition metal) bring an open 3D framework advantageous for ion mobility and structural stabilization efficient for enduring prolonged electrochemical cycles. In addition, oxygen evolution is commonly observed for the layered materials above 200 ^oC [20, 21], while polyanion compounds are mostly thermally-stable due to covalently bonded PO_4 framework. [22] Although electric conductivity in polyanion-based materials is usually

very low compared to that of layered transition metal oxide components, particle modification by applying carbon coting or downscaling of partial size, contributes to a dramatic increase in electrical conductivity to improve electrochemical performance. $LiFePO_4$ have been applied in commercialized cells since 1996, and it is one of the well-established cathode material for LIBs. $LiFePO_4$ has an olivine structure where strongly distorted FeO_6 and PO_4 make frameworks to create cation diffusion paths along with *b*-axis. [23] Its sodium form of $NaFePO_4$ is known to have two different polymorphs with maricite and triphylite (olivine) structures. Crystal structures of both polymorphs consist of PO_4 tetrahedras and distorted FeO_6 octahedras as seen in Fig. 4, and the FeO_6 unites connect each other to make [FeO_5] chains with corner sharing in triphylite and with edge sharing in maricite. The tetrahedral PO_4 units connect to neighboring FeO_6 units with corner both in the maricite and triphylite. Triphylite $NaFePO_4$ cannot be directly synthesized, but only obtained by electrochemical ion-exchange from olivine $LiFePO_4$. There are no cationic channels for Na^+ movement in maricite $NaFePO_4$, while a one-dimensional Na^+ diffusion path is created along the *b*-axis in the triphylite $NaFePO_4$ structure. This structural difference causes distinct difference in electrochemical performance. Maricite $NaFePO_4$ is electrochemically inactive, [24] as the structure blocks Na^+ extraction and insertion. [25] Olivine $NaFePO_4$ shows a relatively high discharge operating voltage of 2.7 V after two charge plateaus at 2.7 V and 3.2 V with reversible capacity over 125 mAh g^{-1}. [26, 27] The electrochemical reaction in olivine $NaFePO_4$ is considered to originate from a redox reaction of Fe^{3+}/Fe^{2+}, which have been confirmed by the XAS studies performed by Ali et al. [28, 29] In 2015, Kisuk and his coworkers prepared nano-sized maricite $NaFePO_4$ by simple ball-milling synthesis, and they demonstrated surprisingly good electrochemical performance of the maricite $NaFePO_4$

with the 1st discharge capacity of 142 mA h g^{-1} and extremely stable cycle performance over 200 cycles. Their *ex-situ* XRD patterns after discharge suggest transformation of maricite $NaFePO_4$ to amorphous $FePO_4$, and they proposes the reversible sodiation/disodiation mechanism between amorphous $FePO_4$ and $NaFePO_4$ after first discharge. [30]

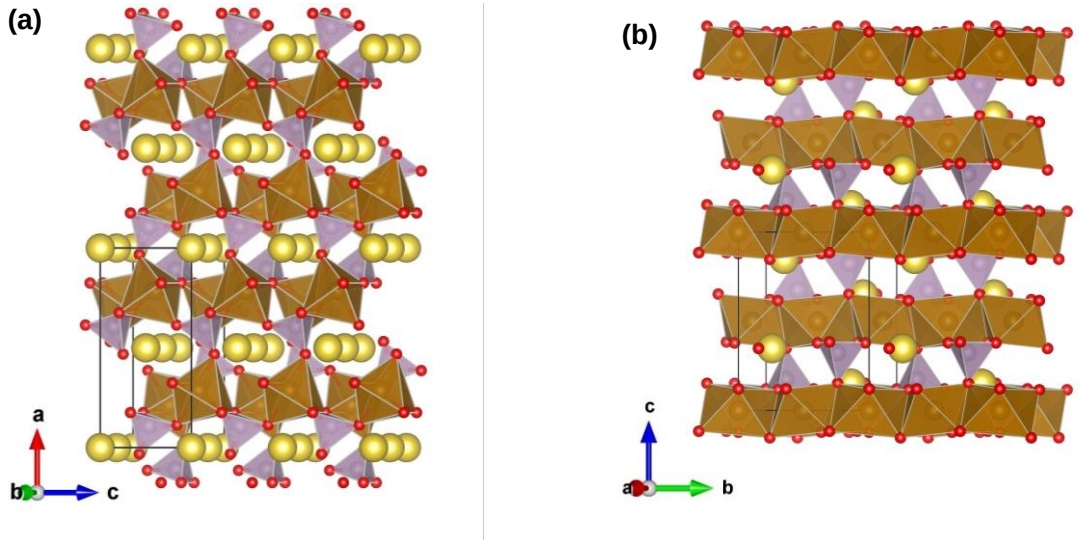

Figure 4. Illustrations of crystal structures of (a) olivine and (b) maricite $NaFePO_4$.

Fluorophosphates positive material

As another approaches to improve electrochemical performance in phosphates active materials, there are several examples for substitution or introduction of F into O atoms in tradition metal octahedras (MO_6). H. Yaghoodnejad found the influence from electronegativity of fluoride by replacing OH with F position in $LiFePO_4(OH)_xF_{1-x}$ [x = 0, 0.32, and 1], confirming increase in the operating voltage and fast Li^+ ion movability in the fluoride-substituted phase. [31] Another successful example of fluorophosphates includes a Na_2FePO_4F a cathode material introduced by the Trascon group. [32]

Na_2FePO_4F have orthorhombic structures with a space group of *Pbcn*, where two octahedral $Fe_2O_7F_2$ units face-share with FeO_4F_2 octahedra via F. PO_4 tetrahedras connect with corner-sharing to form $FePO_4F$ layers. [33] There are two Na^+ cation sites in the interlayer and this structure creates two-dimensional cation paths. [34] Na_2FePO_4F has been modified by carbon-treatment and thus fabricated carbon composite Na_2FePO_4F delivers approximately 110 mAh g^{-1} which corresponds to 90% of theoretical capacity. [35]

Vanadium phosphate positive materials

Vanadium phosphate materials are regarded as promising cathode materials for LIBs because of its stable cycle performance and high working potential above 4.0 V. One of the most well-known vanadium phosphorus cathode materials for LIBs is a NASICON-type $Li_3V_2(PO_4)_3$ component reported by Goodenough. [36] $Li_3V_2(PO_4)_3$ can be prepared by sol-gel method [37-39] as well as electrochemical ion-exchange from $Na_3V_2(PO_4)_3$. [36] It typically exhibits three plateaus at 3.6, 3.7 and 4.1V with discharge capacity of 120 mAh g^{-1}, which varies on partial morphology of the materials depending on their synthetic condition. The fourth plateau is also observed at 4.6 V when conductivity is added by treatments such as carbon coating. [40] The average capacity obtained in three lithium extraction/insertion reactions is ca. 180 mAh g^{-1}. [40, 41] NASICON-type rhombohedral $Na_3V_2(PO_4)_3$ also serves as a cathode in Na system, delivering 110 mhA g^{-1} with one plateau at 3.4 V. Chemical oxidation reaction of $Na_3V_2(PO_4)_3$ has been already reported in 1992, [42] and in the following years, electrochemical Na^+ extraction was investigated by Masquelier. [43] $Na_3V_2(PO_4)_3$ has a rhombohedral structure with space group *R*-3*c*, and an isolated VO_6 octahedra builds up the framework by corner-sharing

with PO_4 tetrahedral units (Fig. 5). [44] $Na_3V_2(PO_4)_3$ functions as an anode material since $Na_3V_2(PO_4)_3$ shows V^{III}/V^{II} redox response at 1.6 V. A full symmetric cell consisting of $Na_3V_2(PO_4)_3$ in both cathode and anode sides has been tested with Na electrolyte. [45, 46] The symmetric cell showed stable and long-term cycle performance over 30,000 cycles under 40C. In association with structural change of $Na_3V_2(PO_4)_3$ during charge and discharge, many studies have been conducted since $Na_{3-x}V_2(PO_4)_3$ brings unique structural diversity in $0<x<2$. $Na_3V_2(PO_4)_3$ shows several flat plateaus during desodiation, which are relevant with a two-phase reaction caused by V^{3+}/V^{4+} redox. Na^+ ions are located at two different sites of M1 and M2 in $Na_3V_2(PO_4)_3$, and Na^+ at the M2 site is responsible for ion movability in $Na_3V_2(PO_4)_3$, whereas a Na^+ ion at the M1 site is immobile.

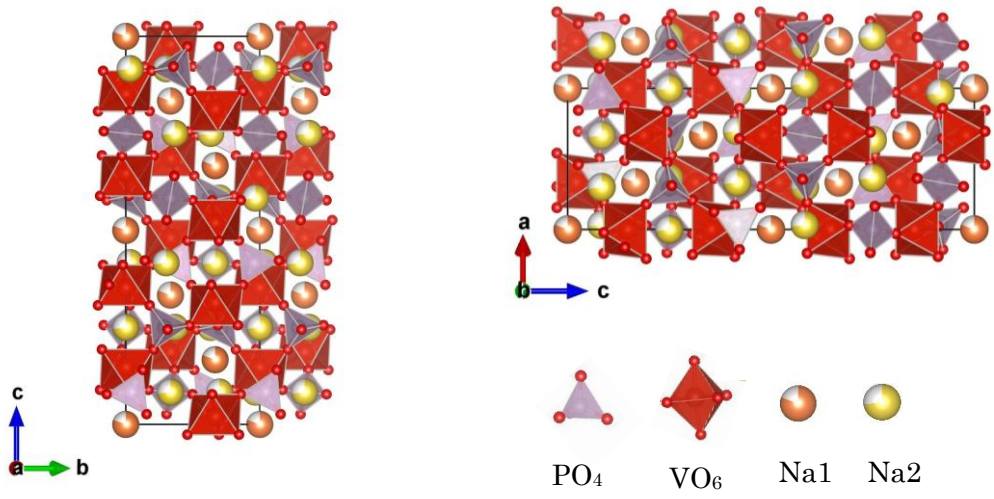

Figure 5. Illustrations of crystal structures of $Na_3V_2(PO_4)_3$ along with *a* and *b* axes.

Barker et al. first introduced $NaVPO_4F$ as a cathode material for SIBs with a hard carbon anode electrode in $NaClO_4$/PC electrolyte. [47] They also demonstrated the

electrochemical comparison between $LiVPO_4F$ and $NaVPO_4F$ in Li cells, where $LiVPO_4F$ has a single plateau while $NaVPO_4F$ exhibits two-step plateaus despite of their similarity in chemical formula and delivering capacity. [48] $NaVPO_4F$ has tetragonal symmetry with a space group of *I*4/*mmm*, [49] where Na^+ ion diffuses along the *c*-axis in a 3D framework consisting of VO_4F_2 octahedra and PO_4 tetrahedra. Sauvage et al. further determined the crystal structure of $NaVPO_4F$ by Reliable refinement based on a crystal structure of $Na_3V_2(PO_4)_2F$ and proposed that $NaVPO_4F$ can be presented as $Na_{1.5}VOPO_4F_{0.5}$, because the structure is assumed to be between $NaVPO_4F$ and $Na_3V_2(PO_4)_2F$ phases and quantitate analysis is difficult on $NaVPO_4F$. [50] In the structure of $Na_{1.5}VOPO_4F_{0.5}$, Na^+ ions are disordered across two sites (8h and 8j) and the oxidation state of V is 4^+. The crystal structure is composed of a VO_5F octahedral and PO_4 tetrahedra sharing O vertices parallel to the *a*-*b* plane. Along the *c*-axis direction, VO_5F octahedras are connected via F in *cis* and *trans* configuration located in the same *a*-*b* plane. Similar like to $Na_{1.5}VOPO_4F_{0.5}$, $Na_{1.5}VPO_{4.8}F_{0.7}$ provided a discharge capacity of ca. 137 mAh g^{-1} arising from the $V^{3.8+/5+}$ redox reaction with excellent cycle performance over 500. [51] $Na_{1.5}VPO_{4.8}F_{0.7}$ is comprised of tetrahedral PO_4 and VO_5F/VO_4F_2 octahedral units with corner-sharing, which forms a three-dimensional open framework with Na^+ ions located at interstitial sites. Although structural refinements on these $Na_{1.5}VOPO_4F_{0.5}$ and $Na_{1.5}VPO_{4.8}F_{0.7}$ were performed based on space group *P*42/*mnm*, the XRD pattern turns out to be the same for both formulas. These works are notable because variation in the anion configuration and content of oxygen and fluorine dramatically improved electrochemical performance. Several research gropes have explored isostructural $NaVOPO_4$ form where F in $NaVPO_4F$ is replaced with O, and consequently, the electrochemical process proceeds with the redox reaction of V^{4+}/V^{5+} in

$NaVOPO_4$. [52, 53] Unfortunately these materials do not work well in the sodium system as $LiVOPO_4$ [54, 55] in Li system.

1.3. Organic Na insertion active materials

Commonly used cathodes for LIBs such as $LiCoO_2$ are synthesized from limited mineral resources, and thus minor-metal free or low-cost materials that can be derived from more abundant resources have become increasingly desirable along with the world's growing ecological concerns. Studies of organic active materials can be started from the discovery of conductive polymers in 1970's and Macinnes et al proposed application of semiconducting materials as light weight rechargeable storage batteries [56]. So far, many organic-based electrode active materials for LIBs are reported, including organic sulfide polymers [57-60] and organic radicals [61-63]. However, organic compounds have received less attention because of their low conductivity and low volume density. Nevertheless, there are increasing number of organic cathode or anode active materials for SIBs and several organic compounds with redox active functional group are successful for SIBs. Table 4 summarizes representative organic electrode active materials, and their molecular structures are shown in Fig. 6.

Table 4. Reported organic Na-insertion compounds in the literature.

	Formula	No. in Fig.6	Experimental capacity ($mAh\ g^{-1}$)	Working voltage (V vs. Na/Na^{+})	Ref.
Disodium Terephthalate and its derivatives (Na_2TP)	$Na_2C_8H_4O_4$	(1)	220	0.4	[64]
	NH_2-Na_2TP	(2)	200	0.5	[65]
	Br-Na_2TP		200	1.1	[65]
	NO2-Na_2TP		300	1.0	[65]
Disodium rhodizonate	**$Na_2C_6O_6$**	**(3)**	**170**	**2.18**	**[66]**
4,4-1-Biphenyldicarboxylate	$NaC_{14}H_6O_4$	(4)	200	0.5	[67]
	$Na_2C_{14}H_8O_4$		220	0.4	
Benzenediacrylates	$Na_2C_{12}H_8O_4$	(5)	100	0.65	[68]
Disodium croconate	**$Na_2C_5O_5$**	**(6)**	**150**	**1.3**	**[69-71]**
Indigo carmin	$C_{16}H_8N_2Na_2O_8S_2$	(7)	90	1.8	[72]
Disodium pyromellitic diimidate	$Na_2C_{10}H_2N_2O_4$	(8)	90	1.2	[73]
Tetrasodium salt of 2,5-dihydroxyterephthalete	$Na_4C_8H_2O_6$	(9)	175	0.3	[74]
9,10-anthraquinone	$C_{14}H_8O_2$	(10)	190	1.8	[75]
2,5-dihydroxy-1,4-benzoquinone	$Na_2C_6H_2O_4$	(11)	200	1.25	[76] [77]

Compounds with bold are the material in this work.

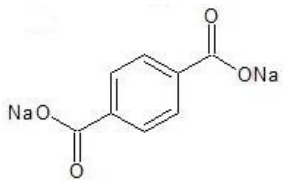

(1)

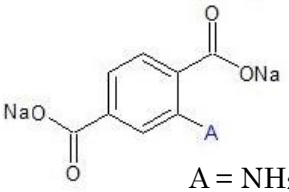

A = NH_2, NO and Br

(2)

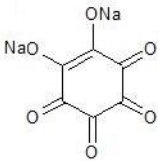

(3)

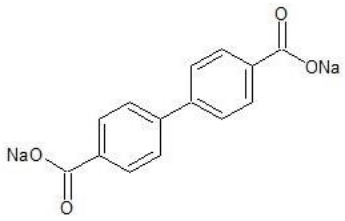

(4)

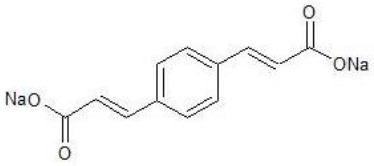

(5)

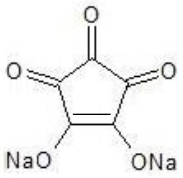

(6)

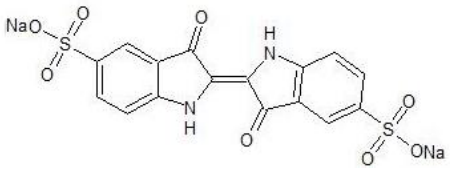

(7)

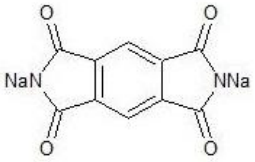

(8)

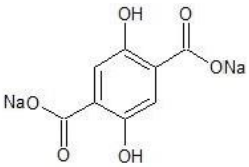

(9)

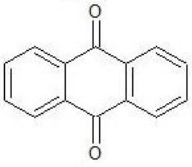

(10)

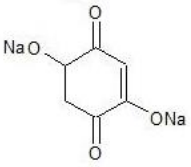

(11)

Figure 6. Molecular structures for organic electrode active materials for SIBs.

One of the most promising organic materials includes $Na_2C_8H_4O_4$ having a telephthalate functional group. Zhao et al. fund $Na_2C_8H_4O_4$ is suitable for an anode for

SIBs in 2012, [64] and further researches by other groups demonstrated that related carboxylate aromatic dicarboxylates group compounds usually exhibit reversible redox-reactions at 0.2 - 0.5 V vs. Na/Na^+ [78-79] and stable charge/discharge behavior over multiple cycles. $Na_2C_8H_4O_4$ itself shows a reversible capacity of 220 mAh g^{-1}, corresponding to two electron transfer with excellent cycle performance. [64] In the same year, Park et al. reported disodium terephthalate and its derivatives having amino-, bromo-, and nitro- functional groups on the phenyl ring. [65] The bromo-, and nitro-substituted $Na_2C_8H_4O_4$ electrodes delivered a high capacity of 300 mAh g^{-1}, while, amino- substituted one showed the relatively lower capacity of 200 mAh g^{-1}. They also fund the regio-isomerism form in phthalates greatly affects the thermodynamic and kinetic properties of their redox intermediates. This finding implies that the chemical modification of benzene decarboxylates by adding another functional groups can control the electrochemical outcomes, which make a significant advantage for organic materials.

As given the new requirements in the development of SIBs, such as low production costs and structure limitation for large sodium ions, organic compounds have several advantages, including multiple electron reaction, their structural diversity, layer stacking structure, and cost-effective aspects [80]. Organic materials have been considered to be useful counterparts for rechargeable batteries because they are accessible and free of minor metals. Although relatively few studies have been conducted in the research for SIBs so far, organic components could become strong candidates for SIBs.

1.4. Purpose of this study

As the most popular energy storage technology, rechargeable Li-ion batteries have been widely used in portable electronic devices. Their application fields have been expanding to larger scale devises such as electric vehicles (EVs) and a smart grid system utilizing renewable and sustainable green energies. These movement has been considered as a solution to take a step toward more environmentally friendly society, and regarded to be truly helpful for relieving energy crisis and global energy gap between countries. Under this circumstances, researches have been actively conducted to introduce LIBs into the systems to facilitate clean energy technologies. However, when the energy storage system is enlarged, cost performance becomes a more dominant factor rather than electrochemical performance, and hence, inexpensive batteries, which can be derived from low cost and abundant materials, become more and more desirable. Rechargeable sodium-ion batteries have been, therefore, studied for past few years and regarded as an alternative candidate to LIBs due to the abundant reserve and even-distribution of Na resources. Nonetheless, the highest energy density of SIBs with long cycles is still 115 Ah/kg equal to $LiMn_2O_4$, further development are required to bring them to the market. Since the energy density of SIBs always fells in short compared to that of LIBs because Na has higher standard electrode potential and heavier atomic weight than Li, development on performance of known materials and/or research of new active materials for SIBs is needed to be emphasized on whether they show high working voltage and/or large discharge capacity.

The reported cathode active materials with relatively good electrochemical properties for SIBs can be categorized to some special material groups, and their common features are an open structure capable enough to accept large sodium ions. Among them,

fluorophosphates materials shows higher working voltage than other materials such as layered tradition metal oxides because of inductive effect from PO_4 units and high electronegativity of F. We hence have taken a particular interest in $Na_3M_2(PO_4)_2F_3$ [M = tradition metal], which have an open structure consisting of corner-sharing matrix made up MO_6 octahedras and PO_4 tetrahedras with connecting with F, as a high voltage cathode material for SIBs.

In addition, we also search cathode materials with large discharge capacity from organic components with multi redox functional groups. Lamellar stacking structures of organic compounds would also play as suitable sodium insertion host frameworks due to their low density and stacking structure.

In this paper, we will present electrochemical property and structural evolution of $Na_3M_2(PO_4)F_3$ (M = Ti, V, and Fe) during cycles. In addition, $Na_2C_6O_6$ and their analog will be discussed as a new cathode materials for SIBs and their structure change during cycle will be also presented.

Chapter 1 described the basic principles of secondary batteries, and the brief introduction of lithium and sodium-ion batteries including methodologies and previous studies.

Chapter 2 will discuss the synthesis and electrochemical properties of $Na_3M(PO_4)F_3$ (M = Ti, V, and Fe) materials in half and full cell configurations. The structural evolution of $Na_3V_2(PO_4)F_3$ investigated by *ex-situ* XRD measurements will be shown to account for the good reversibility of this material.

In chapter 3, the motivation for applying organic cathode materials to sodium ion batteries will be briefly introduced, and then electrochemical properties of $Na_2C_6O_6$ will be discussed in half and full cell conditions. Since $Na_2C_6O_6$ shows large reversible capacity over 200 mAh g^{-1} possibly due to its multiple electron reaction, the electrochemical property of $Na_2C_6O_6$ analogs including $Na_2C_5O_5$, $Na_2C_4O_4$, and $K_2C_6O_6$ will be additionally described for comparison.

In chapter 4, the structural change of $Na_2C_6O_6$ during electrochemical cycle (sodiation/ disodiation) will be discussed based on Fourier transform infrared spectroscopy, X ray diffraction, and solid nuclear magnetic resonance to discuss charge and discharge mechanism of $Na_2C_6O_6$.

In chapter 5, the summary of this thesis and conclusions will be noted in this chapter.

Chapter 2. Synthesis and Electrochemical Property of $Na_3M_2(PO_4)_2F_3$ for Na-ion Batteries

2.1. Introduction

As already mentioned in Chapter 1, sodium-ion batteries (SIBs) have been aggressively investigated as a promising alternative to lithium-ion batteries (LIBs) for resent past years, and they are expected to bring economic and environmental advantages because sodium is abundant, inexpensive, and nontoxic. However, the standard electrode potential of sodium (-2.71 V vs. SHE) is lower than that of lithium (-3.05 V vs. SHE), and its ionic volume is twice the lithium ion and the molecular weight is triple.[8] Hence, it have to be well considered in the selection of an insertion host for large Na^+ ions. With taking into account for the studies in cathode materials for LIBs, vanadium phosphates components such as $Li_3V_2(PO_4)_3$ [36] α/β-$VOPO_4$ [81-83], and $LiVPO_4Z$ (Z=O and F) [55, 56, 84-87] have exhibited excellent electrochemical performance with the reversible capacity close to their theological capacity and 4V-class working voltage attributed to inductive effect from PO_4 [93]. These electrochemical characteristics are considered to be originated from their 3D frameworks which bring an open structure advantageous for ion mobility and structural stabilization efficient for enduring prolong electrochemical cycles. Among the past studies in the sodium system, the reported cathode active materials with relatively good electrochemical properties are mainly categorized to some special material groups such as two-dimensional layered chalcogenides with van der Waals gaps, e.g., TiS_2 [88], layered rocksalt oxides, [89 - 92] e.g., $NaFeO_2$ [93] and three-dimensional polyanion materials with corner sharing matrix. In addition fluorophosphates materials [31, 32, 47] shows higher working voltage compared to another groups including oxide, phosphate

and even fluoride, and hence, $Na_3M_2(PO_4)_2F_3$ [M = Ti, Fe, V] were focused in this thesis as a high voltage cathode material for SIBs. Originally, Meins et al. first synthesized $Na_3M_2(PO_4)_2F_3$ ($M = Al^{3+}$, V^{3+}, Cr^{3+}, Fe^{3+}, Ga^{3+}) family to investigate their thermal phase tradition and magnetic susceptibility [94], and Barker introduced $Na_3V_2(PO_4)_2F_3$ as cathode materials for so-called hybrid LIBs in 2005. [95] In the hybrid LIBs system, Na^+ in $Na_3V_2(PO_4)_2F_3$ is extracted during first charge, and Li^+ inserts to empty sodium sites in $Na_{3-x}V_2(PO_4)_2F_3$ instead of Na^+ during following discharge process to form $Na_{3-x}Li_xV_2(PO_4)_2F_3$ at the end of discharge. In 2011, we have first proposed $Na_3M_2(PO_4)_2F_3$ [M = Ti, Fe, V] as promising cathode materials for SIBs [96]. In this chapter, electrochemical properties of the $Na_3M_2(PO_4)_2F_3$ [M = Ti, Fe, V] family in SIBs will be discussed, and *ex-situ* XRD measurements for the electrodes after charge or discharge at selected voltages were carried out in order to examine the structural change accompanying Na^+ extraction/insertion. For an advanced discussion, we performed a structure energy calculation using the Vienna ab initio simulation package (VASP) to elucidate the Na^+ extraction/insertion mechanism in the $Na_3V_2(PO_4)_2F_3$ structure during the first cycle.

2.2. Experimental

Synthesis of $Na_3M_2(PO_4)_2F_3$ [M = Ti, Fe, V]

$Na_3M_2(PO_4)_2F_3$ [M = Ti, Fe, V] was prepared by a conventional solid-state synthesis for a metal phosphate compound [94]. V_2O_5 (Nacalai Tesque Inc.) or Ti_2O_3 (SIGMA-Aldrich) and $(NH_4)_2HPO_4$ (Wako Pure Chemical Industries) were mixed with a stoichiometric ratio, placed in a crucible, and heated at 650 - 950 ˚C for 15 h under 5% H_2 + Ar flow. $FePO_4 \cdot 2H_2O$ (SIGMA-Aldrich) was pretreated at 100 ˚C under vacuum

for 3 h to dehydrate. The obtained MPO_4 [M = Ti, Fe, V] was palletized after mixing with a stoichiometric ratio of NaF (Wako Pure Chemical Industries) and calcined again at 600 ˚C for 2 h under Ar flow.

Characterization of $Na_3M_2(PO_4)_2F_3$ [M = Ti, Fe, V]

X-ray diffraction (XRD) measurements were performed on a Rigaku RINT2500 powder diffractometer using Cu-Kα radiation (50 kV and 300 mA) from 2θ = 10 - 80° with 0.02° step scan at a rate of 1.0° min^{-1}. The cell parameters were calculated by Rietveld method using RIETAN-FP software (Rigaku) based on β-$Na_3V_2(PO_4)_2F_3$ [94].

Cell preparation and electrochemical measurement of $Na_3M_2(PO_4)_2F_3$ [M = Ti, Fe, V]

For the electrochemical studies, the 70 wt. % obtained $Na_3M_2(PO_4)_2F_3$ [M = Ti, Fe, V] powder was first dry-ball-milled with 25 wt. % acetylene black (DENKA) in Ar. The $Na_3M_2(PO_4)_2F_3$/C composite powder was mixed with a 5 wt. % PTFE teflon binder (Daikin Industries) to fabricate cathode pellets. The pellets were punched in the form of disks with approximately 15 mg in weight and 10 mm in diameter, and then dried at about 110 ˚C overnight in vacuum before assembling cells. For the case of a rate capability test, sheet type cathodes were prepared with 5 wt. % polyvinyl difluoride (PVdF/NMP) (Kureha) binder and N-methylpyrrolidone (NMP) (Wako Pure Chemical Industries). The obtained slurry was coated on Al sheets. The cathode sheet was dried at 80 ˚C for 30 min and cut to a diameter of 15 mm, and then dried at about 110 ˚C overnight in vacuum. The electrochemical performance of $Na_3M_2(PO_4)_2F_3$ [M = Ti, Fe, V] was evaluated by a 2032 coin-type cell using a non-aqueous electrolyte (1 M $NaClO_4$/PC, Tomiyama Pure Chemicals Industries) and a polypropylene separator (Celgard 3501) against sodium metal (SIGMA-Aldrich). To avoid any influence from air, all cell assembling processes

were conducted in an Ar-filled glovebox. The charge/discharge measurement was carried out in galvanostatic mode with a current rate of 0.2 mA cm^{-2} within the various potential windows. All electrochemical tests were done in 25 ˚C.

Investigation for sodiation and desodiation process of $Na_3V_2(PO_4)_2F_3$

***Ex-situ* XRD measurement**

To investigate the structural change during the charge/discharge measurement, the charged or discharged electrodes were carefully taken out from the cells, washed, and soaked in propylene carbonate (PC, Tomiyama Pure Chemicals Industries) for overnight to remove the electrolyte. They were then dried in the Ar-filled grove-box under vacuum. The *ex-situ* XRD measurements were performed for the various charged or discharged states using Cu-Kα radiation (50 kV and 300 mA) from 2θ = 10 - 80° with 0.02° step scan at a rate of 0.15 ° min^{-1}. All of the *ex-situ* XRD data were taken under Ar condition using an air-tight specimen holder (Bruker) in order to avoid any influence from air.

Calculation

The crystal structure model of β-$Na_3V_2(PO_4)_2F_3$ was built up based on to the reported crystallographic data [94] as illustrated in Fig. 7. The structure has a three-dimensional framework consisting of a PO_4 tetrahedra and VO_4F_2 octahedra linked at their corners through F atoms. Na atoms are layered along the *a-b* plane in the tetragonal *P*42/*mnm* unit cell. To obtain a reasonable Na^+ extraction mechanism and geometrical information, the density functional theory calculations were performed with VASP [97] using plane waves as a basis set and β-$Na_3V_2(PO_4)_2F_3$ [94] as an initial standard compound. A super-cell with four molecular formula units was used for this calculation. The geometry optimization and band structure calculations were performed using the projector augmented wave (PAW) method [98] and the generalized gradient approximation (GGA)

[99] expressed by Perdew-Burke-Ernzerhof (PBE) functional [100]. *β*-$Na_3V_2(PO_4)_2F_3$ has 2 molecular formulas in the tetragonal unit cell. In the matrix, the Na atoms occupy at the 8*i* site which has two different coordinates; 2 Na atoms in Na1 site and 1 Na atom in Na2 site (Table. 5). To estimate the possible 1 Na^+-extracted state compound of $Na_{(3-1)}V_2(PO_4)_2F_3$, two presumable patterns were simulated, as followed; Pattern1: half of Na1 atoms in the 8i site-1 were symmetrically eliminated from the super cell. Pattern 2: all of Na2 atoms in the 8i site-2 were symmetrically eliminated from the super cell.

Table 5. Structure parameters of Na in β-$Na_3V_2(PO_4)_2F_3$.

Na site	Occ.	x	y	Z
8i site-1	1.0	0.0234(2)	0.7299(1)	0.0000
8i site-2	0.5	0.3030(1)	0.5512(3)	0.0000

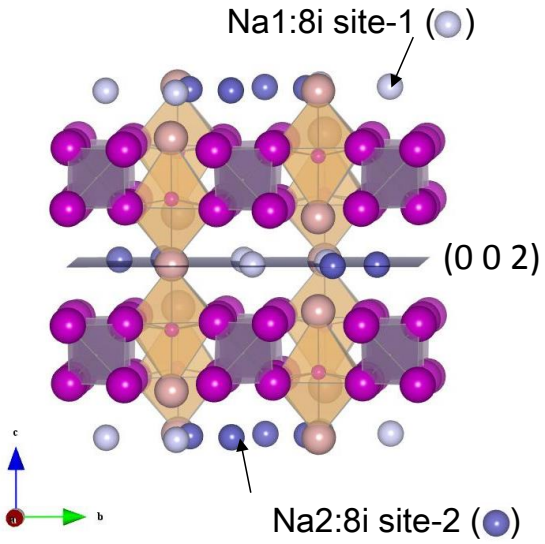

Figure 7. Illustration of crystal structure of $Na_3V_2(PO_4)_2F_3$ along *a*-axis.

2.3. Results and discussion

2.3.1. Characterization

The crystal structure of the obtained $Na_3M_2(PO_4)_2F_3$ [M = Ti, Fe, V] was characterized by XRD. The XRD profiles for the obtained $Na_3M_2(PO_4)_2F_3$ [M = Ti, Fe, V] powders are shown in Fig. 8. Their XRD patterns were all identified to the tetragonal structure with the space group *P*42/*mnm* and they were isostructural with β-$Na_3V_2(PO_4)_2F_3$ (ICDD No. 089-8485) [94], although recent studies based on a high-resolution diffraction using synchrotron radiation have suggested the possible existence of F and O mixing in the structure. [101]. No major impurity phases were found from the analysis for $Na_3Ti_2(PO_4)_2F_3$ and $Na_3V_2(PO_4)_2F_3$, while $Na_3Fe_2(PO_4)_2F_3$ contained $Na_3Fe(PO_4)_2$ (ICDD No 01-088-1236) as an impurity. Their cell parameters calculated by means of the RIETAN-FP software were a = 9.1314 and c = 10.759 in $Na_3V_2(PO_4)_2F_3$, a = 9.0381 and c = 10.723 in $Na_3Ti_2(PO_4)_2F_3$, and a = 9.050 and c = 10.68 in $Na_3Fe_2(PO_4)_2F_3$.

Table 5. Lattice parameter of $Na_3M_2(PO_4)_2F_3$ with the space group of *P4₂/mnm*

	β-$Na_3V_2(PO_4)_2F_3$*	$Na_3Ti_2(PO_4)_2F_3$	$Na_3V_2(PO_4)_2F_3$	$Na_3Fe_2(PO_4)_2F_3$
a (=b)/Å	9.047(2)	9.1314(7)	9.0381(7)	9.050(1)
c/Å	10.705(2)	10.759(1)	10.723(1)	10.68(1)

*β-$Na_3V_2(PO_4)_2F_3$ ICDD No: 01-089-8485 [94]

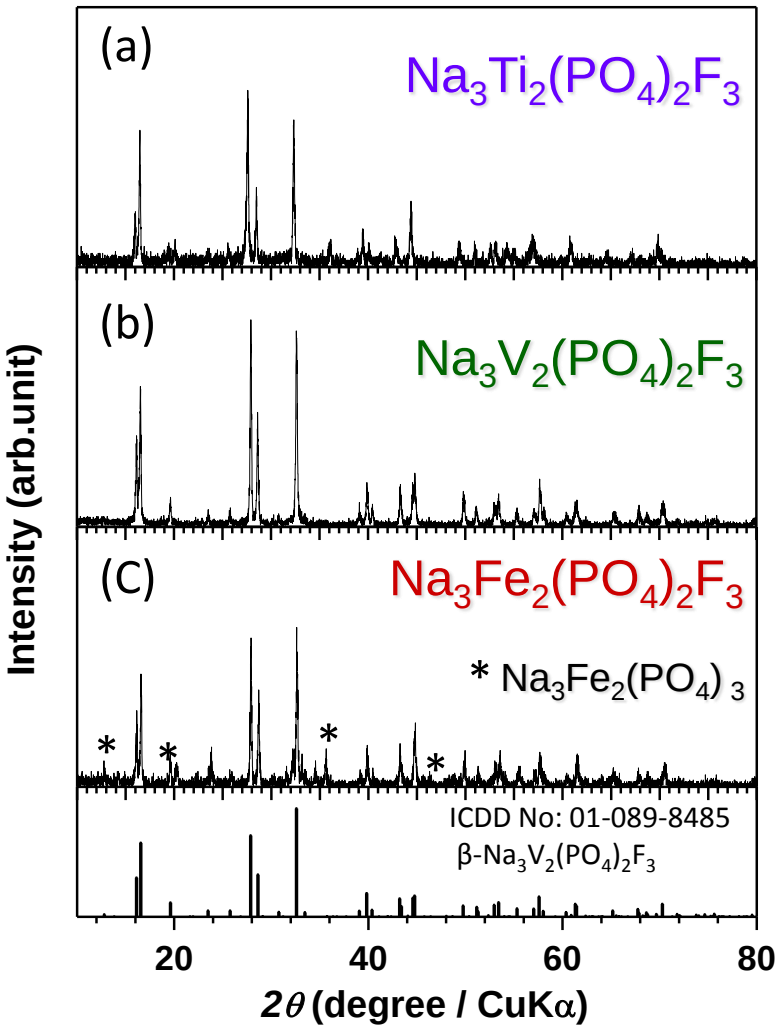

Figure 8. XRD patterns of (a) $Na_3Ti_2(PO_4)_2F_3$, (b) $Na_3V_2(PO_4)_2F_3$, and (a) $Na_3Fe_2(PO_4)_2F_3$.

2.3.2. Electrochemical investigation of $Na_3M_2(PO_4)_2F_3$ [M = Ti, Fe, V]

Electrochemical properties of $Na_3M_2(PO_4)_2F_3$ [M = Ti, Fe, V] in Na cells

The charge/discharge cycles of $Na_3Ti_2(PO_4)_2F_3$, $Na_3V_2(PO_4)_2F_3$ and $Na_3Fe_2(PO_4)_2F_3$ were carried out in voltage ranges of 3.2 - 1.5 V, 4.3 - 2.3 V and 2.3 - 4.3 V, respectively. Figure 9(a), (b), and (c) show the first and 2nd charge and discharge curves of $Na_3Ti_2(PO_4)_2F_3$, $Na_3Fe_2(PO_4)_2F_3$, and $Na_3V_2(PO_4)_2F_3$, respectively. $Na_3Ti_2(PO_4)_2F_3$

showed the first discharge capacity of 57.7 mAh g^{-1} with two extraction/insertion plateaus at 2.7 V and 2.4 V during cycles in which stable cycle performance was observed in the both of the regions. Although the confirmed reversible Na reaction amount was only ca. 0.5, $Na_3Ti_2(PO_4)_2F_3$ exhibited less irreversible capacity with a small voltage gap between charge and discharge. On the other hand, the first discharge capacity of $Na_3Fe_2(PO_4)_2F_3$ was less than 30 mAh g^{-1}, and very small plateaus corresponding to Fe^{2+}/Fe^{3+} redox reaction was observed at 2.5 V. This poor electrochemical property would be attributable to the low conductivity, and further modifications, such as a carbon-coating method reported in the $LiFePO_4$/C composite [102], might be effective. Among the $Na_3M_2(PO_4)_2F_3$ [M = Ti, Fe, V] family, $Na_3V_2(PO_4)_2F_3$ showed the largest rechargeable capacity of 120 mAh g^{-1}, which corresponded to the capacity from 2 Na^+ extraction/insertion reaction. $Na_3V_2(PO_4)_2F_3$ exhibited two-step discharge voltage plateaus at 4.1 V and 3.6 V in charging up to 4.3 V and these plateaus originated to V^{3+}/V^{4+} redox reaction. Unfortunately, third Na^+ was not able to extracted even in the increased voltage range between 4.6 – 2.3 V, although 3 Li^+ ions in NASICON-type $Li_3V_2(PO_4)_3$ can be reversibly extracted and inserted. [20]

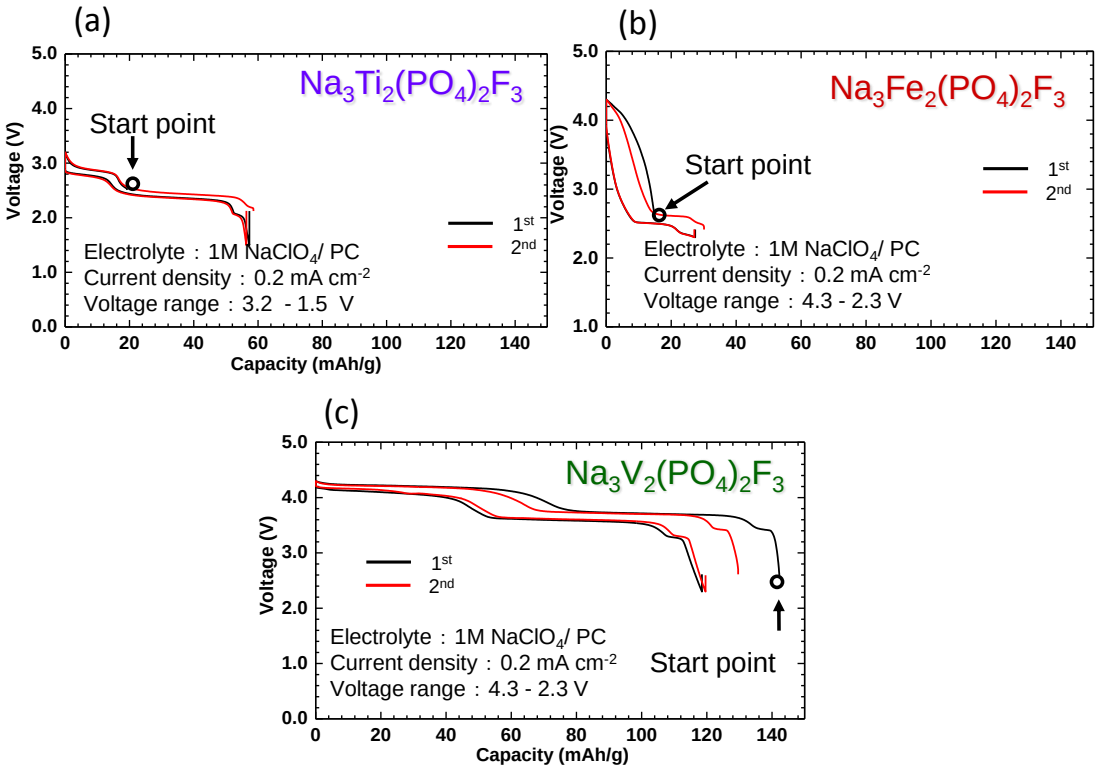

Figure 9. Charge and discharge profiles of $Na_3M_2(PO_4)_2F_3$ [M = (a) Ti, (b) Fe, and (c) V] in Na cells.

Figure 10 shows the charge/discharge profiles and cycle performance of $Na_3V_2(PO_4)_2F_3$ with the different cutoff voltage from 1.0 V to 4.6 V. Surprisingly, $Na_3V_2(PO_4)_2F_3$ showed stable cycle performance even between high voltage range from 2.3 V to 4.6 V, achieving discharge capacity of 115.12 mAh g^{-1} at the 40th cycle corresponding to 94% from the initial discharge capacity. In addition, another discharge plateau was seen at ca. 1.2 V in the potential window down to 1.0 V, which was attributable to the V^{2+}/V^{3+} redox reaction (Fig. 10(b)). In order to check structure degradation of $Na_3V_2(PO_4)_2F_3$, *ex-situ* XRD measurements were performed with the electrode after 15 cycles. Figure. 11 shows the XRD profiles of the initial (Fig. 11(a)) and 15th-cycled $Na_3V_2(PO_4)_2F_3$ electrodes in the voltage range of 4.1 - 2.3 V (Fig. 11(b)), 4.3

- 2.3 V (Fig. 11(c)) and 4.6 - 2.3 V (Fig. 11(d)). The tetragonal structure of $Na_3V_2(PO_4)_2F_3$ was completely maintained even with the high charge voltage to 4.6 V and no other distinct phase or impurity phase were generated during the repeated cycles. This result suggested that $Na_3V_2(PO_4)_2F_3$ structure was flexible enough to accommodate the structure change accompanied by the extraction/insertion of large sodium ions.

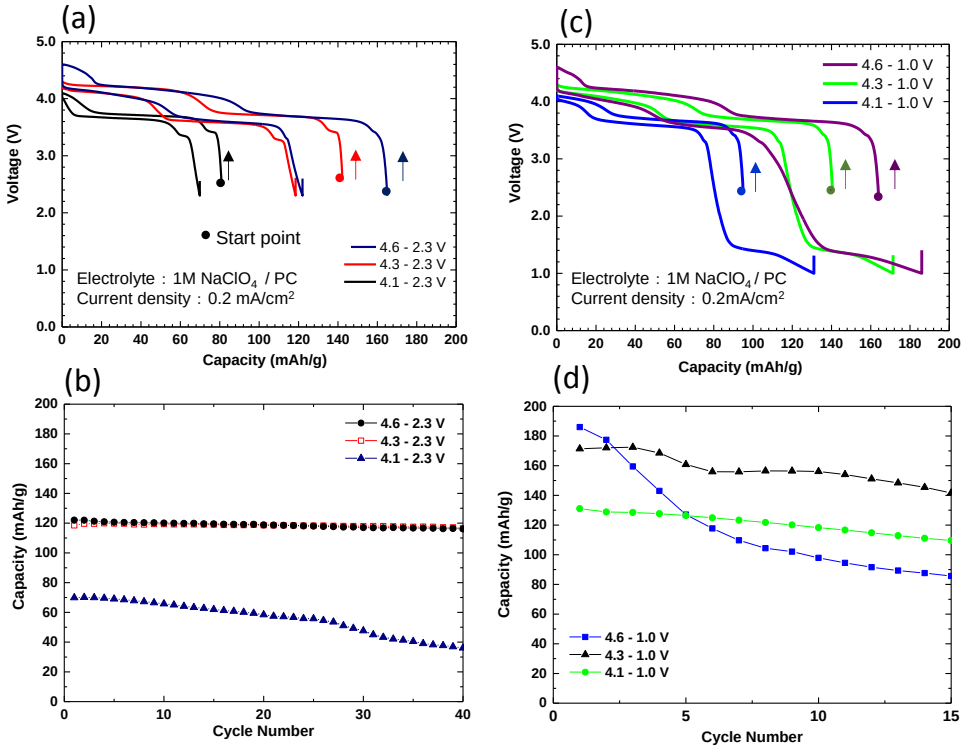

Figure 10. (a) The charge and discharge profiles and (b) cycle performance of $Na_3V_2(PO_4)_2F_3$ with the different charge cutoff voltage of 4.6, 4.3 and 4.1 V with 2.3 V discharge. (c) The charge and discharge profiles and (d) cycle performance of $Na_3V_2(PO_4)_2F_3$ with the different charge cutoff voltage of 4.6, 4.3 and 4.1 V with 1.0 V discharge.

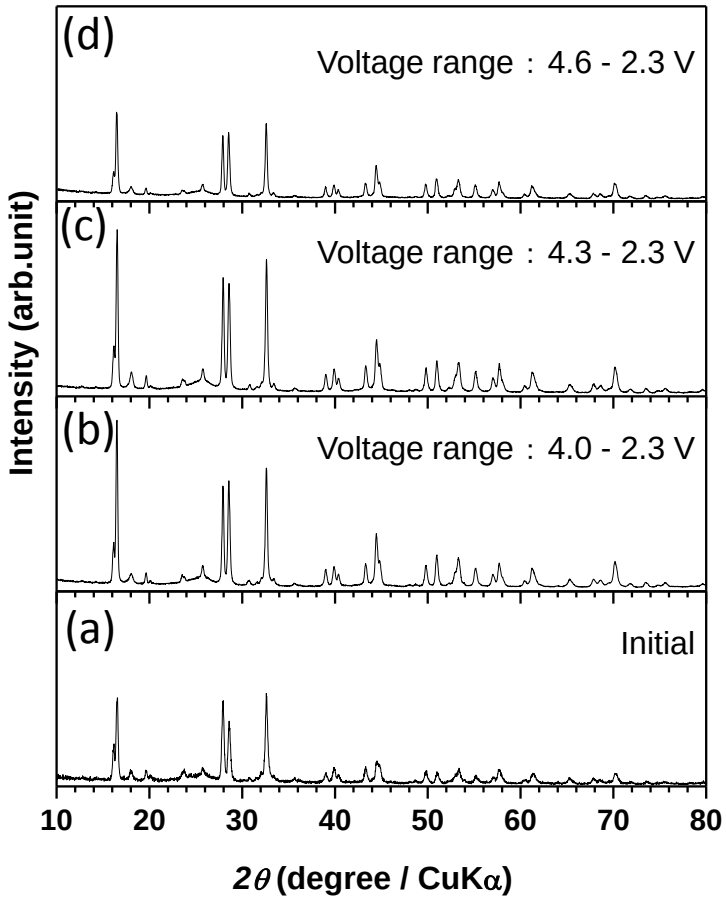

Figure 11. XRD profiles of the (a) initial and 15th-cycled $Na_3V_2(PO_4)_2F_3$ electrodes with cycles between (b) 4.1 - 2.3 V, (c) 4.3 - 2.3 V and (d) 4.6 - 2.3 V.

The rate capability of $Na_3V_2(PO_4)_2F_3$ was evaluated with sheet type electrodes prepared through the process as described in the experimental section. The sheet type electrodes with about 5 mg in total weight including about 3.5 mg of $Na_3V_2(PO_4)_2F_3$ were carefully selected for the test, and different rates were applied on a single cell. The charge/discharge measurement was performed in galvanostatic mode. Figure 12(a) and (b) show the $Na_3V_2(PO_4)_2F_3$ discharging behaviors dependent upon current rates against sodium metal with the voltage range of 4.3 - 2.3 V. In Fig. 12(a), the current density for the charge was fixed to 0.2C and the current density for discharge was adjusted to

approximate rates of 0.5C, 1C, 4C, 8C and 10C based on the theoretical capacity of 2 Na^+ extraction/insertion of 128.3 mAh g^{-1}. In Fig. 12(b), on the other hand, both charge and discharge rate was changed to 0.5C, 1C, 4C, 8C and 10C at the same time. $Na_3V_2(PO_4)_2F_3$ showed good rate capability with fixed charge current of 0.2C and the cathode reversible capacity at 10C discharge was more than 75% of the 2 Na^+ extraction/insertion capacity of 128.3 mAh g^{-1}. While, the capacity fade was obvious under the increased charge and discharge current (Fig. 12(b)), and the charge kinetic is rather poor as always seen in phosphate materials.

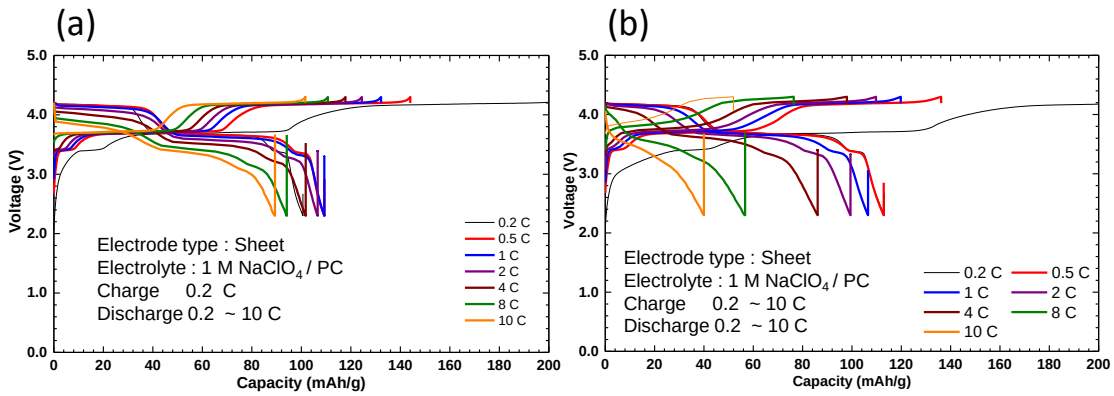

Figure 12. Rate performance of $Na_3V_2(PO_4)_2F_3$. Discharge rate was changed from 0.2 to 10 C and the charge current rate in the corresponding cycle was (a) fixed at 0.2 C and (b) changed from 0.2 to 10C.

Electrochemical properties of $Na_3V_2(PO_4)_2F_3$ in sodium-ion batteries.

In order to confirm the functionality of $Na_3V_2(PO_4)_2F_3$ as secondary batteries, the $Na_3V_2(PO_4)_2F_3$ cathodes were coupled with anode materials to configure a sodium-ion cell. In this time, hard carbon [103] and $NaTi_2(PO_4)_3$ [104, 105] were used as anodes. The hard carbon exhibits discharge capacity of ca. 200 - 300 mAh g^{-1} at lower voltage close

to Na/Na^+, while $NaTi_2(PO_4)_3$ shows the capacity of ca.130 mAh g^{-1} with a flat single plateau at 2.0V. Although, the working potential voltage of $NaTi_2(PO_4)_3$ is relatively high as anode materials, passivation layer and dendrite formation do not occurs, enabling to safe and stable electrochemical cycles. Typical cycle profiles of $Na_3V_2(PO_4)_3$ - $Na_1Ti_2(PO_4)_3$ and $Na_3V_2(PO_4)_3$ - hard carbon in half cells against sodium metal are presented in Fig. 13 and 14, respectively. The cathode-to-anode molar ratio was adjusted to 2.5:1 in $Na_3V_2(PO_4)_2F_3$ / hard carbon cells and 1 : 2 for $Na_3V_2(PO_4)_2F_3/NaTi_2(PO_4)_3$ after optimization of the cathode : anode ratio, and the cell capacity was restricted by the cathode. The $Na_{3-x}V_2(PO_4)_2F_3/Na_xTi_2(PO_4)_3$ sodium ion cells were cycled with a current density of 0.2 mA cm^{-2} in the voltage range of 2.3 - 0.3 V, while the $Na_{3-x}V_2(PO_4)_2F_3$/hard carbon sodium-ion cell was cycled with a current density of 0.1C in the voltage range of 4.29 - 2.29 V.

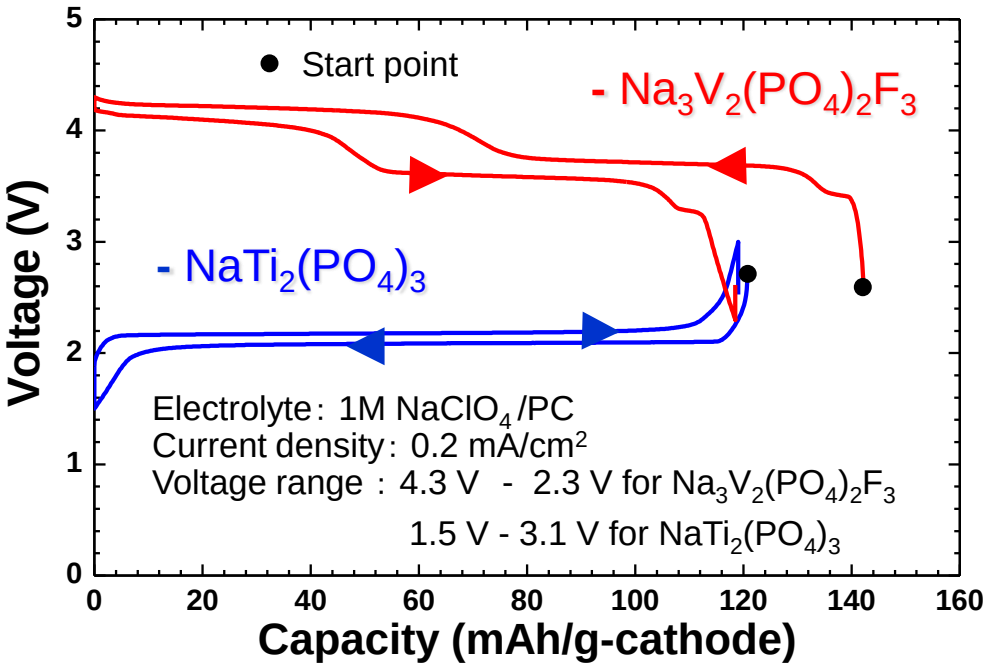

Figure 13 Charge and discharge profiles of $Na_{3-x}V_2(PO_4)_3$ and $Na_{1+x}Ti_2(PO_4)_3$ in Na cells.

Na reaction with each electrode are as follows:

Cathode

Charge: $Na_3V_2(PO_4)_2F_3 \rightarrow Na_{3-x}M_2(PO_4)_2F_3 + xNa^+ + xe^-$

Discharge: $Na_{3-x}M_2(PO_4)_2F_3 + xNa^+ + xe^- \rightarrow Na_3M_2(PO_4)_2F_3$

Anode

Charge: $NaTi_2(PO_4)_3 + xNa^+ + xe^- \rightarrow Na_{1+x}Ti_2(PO_4)_3$

Discharge: $Na_{1+x}Ti_2(PO_4)_3 \rightarrow NaTi_2(PO_4)_3 + xNa^+ + xe^-$

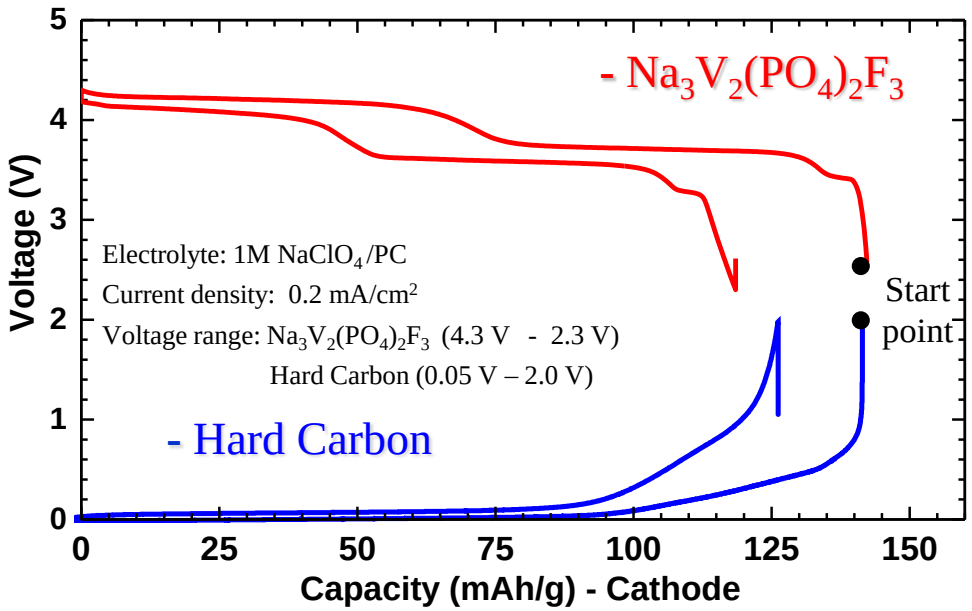

Figure 14 Charge and discharge profiles of $Na_{3-x}V_2(PO_4)_3$ and hard carbon in Na cells.

Na reaction with each electrode are as follows:

Cathode

Charge: $Na_3V_2(PO_4)_2F_3 \rightarrow Na_{3-x}M_2(PO_4)_2F_3 + xNa^+ + xe^-$

Discharge: $Na_{3-x}M_2(PO_4)_2F_3 + xNa^+ + xe^- \rightarrow Na_3M_2(PO_4)_2F_3$

Anode

Charge: $C + xNa^+ + xe^- \rightarrow Na_xC$

Discharge: $Na_xC \rightarrow C + xNa^+ + xe^-$

Figure 15(a) shows the charge/discharge profile of the $Na_3V_2(PO_4)_2F_3/NaTi_2(PO_4)_3$ sodium-ion cell. The first discharge capacity was 119.8 mAh g^{-1} and the stable cyclability around 110 mAh g^{-1} of the cathode in the sodium-ion cell could be confirmed with good capacity retention, 89.4% even at the 50th cycle of the prolonged charge/discharge measurement as shown in Fig. 15(b).

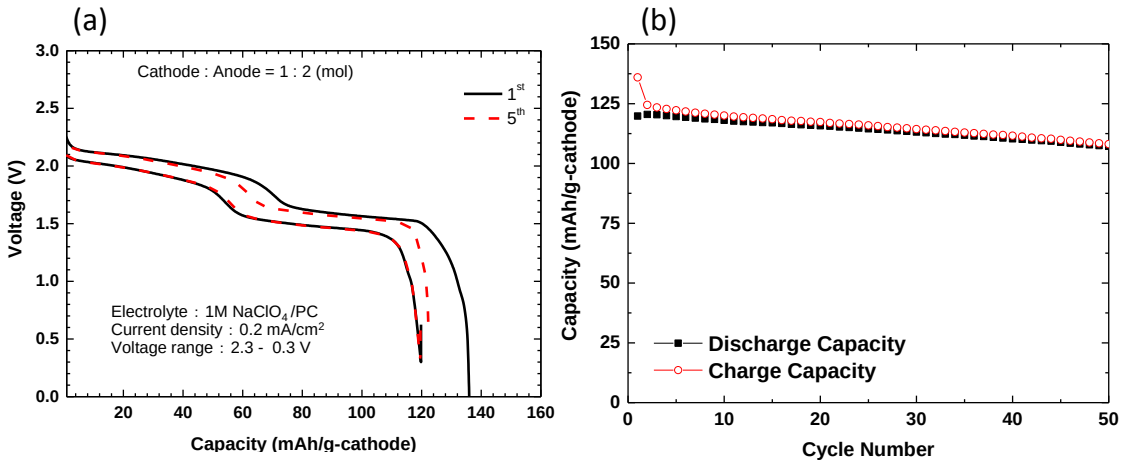

Figure 15. (a) The charge and discharge profile of $Na_{3-x}V_2(PO_4)_2F_3/Na_{1+x}Ti_2(PO_4)_3$ Na-ion cell on 1st and 2nd cycles. (b) Cycle performance of $Na_{3-x}V_2(PO_4)_2F_3/Na_{1+x}Ti_2(PO_4)_3$ Na-ion cells.

Figure 16(a) shows the charge/discharge profile of the $Na_3V_2(PO_4)_2F_3$/hard carbon sodium-ion cell with different electrolyte. Although the $Na_3V_2(PO_4)_2F_3$ electrode exhibited similar electrochemical performance with any electrolyte with $NaTi_2(PO_4)_3$ and sodium metal anodes, electrolyte dependency was observed only in the full cell condition with the hard carbon anode. The reason of this difference dependent on anodes is still unknown, however, since $NaPF_6$ is rater sensitive against water than $NaClO_4$, it may lead some influence to hard carbon anode. The best and stable performance was obtained by using the 1 M $NaClO_4$/PC:EC electrolyte. The first discharge capacity was 115.8 mAh g^{-1} and the stable cyclability around 110 mAh g^{-1} of the cathode in the sodium-ion cell could be confirmed with good capacity retention, 89.4% even at the 40th cycle of the prolonged charge/discharge measurement as shown in Fig. 15(b).

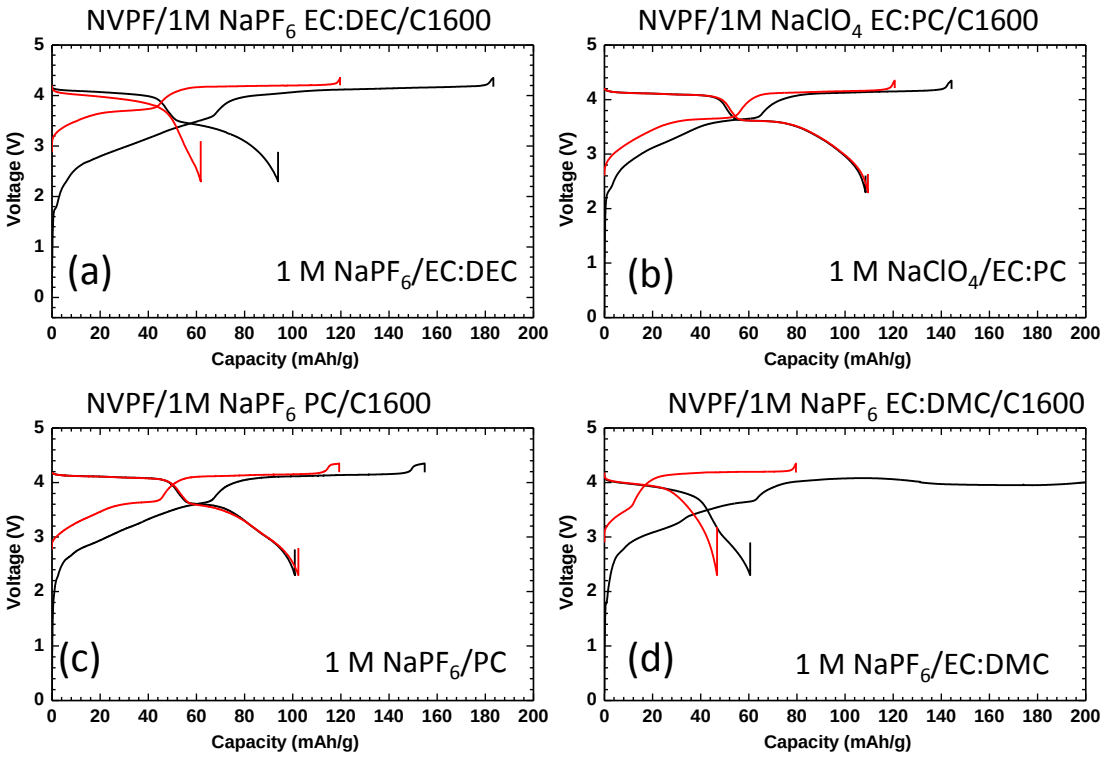

Figure 16. Charge and discharge profile of $Na_{3-x}V_2(PO_4)_2F_3$/Hard carbon Na-ion cells on

1st and 2nd cycles with different electrolyte of (a) 1 M $NaPF_6$/EC:DEC (b) 1 M $NaClO_4$/EC:PC, (c) 1 M $NaPF_6$/PC and (d) 1 M $NaPF_6$/EC:DMC.

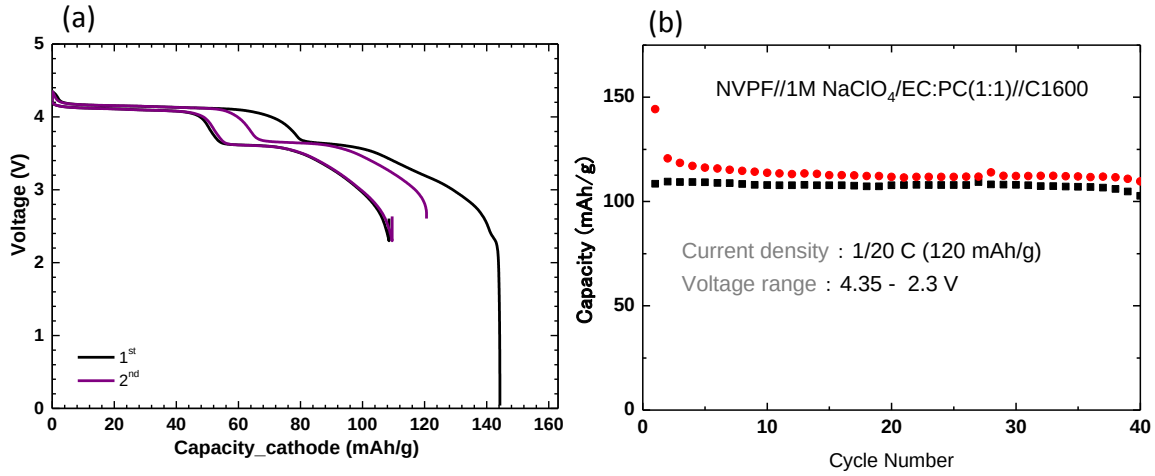

Figure 17. (a) The 1st and 2nd charge and discharge profile and (b) cyclability of $Na_{3-x}V_2(PO_4)_2F_3$/Hard carbon Na-ion cells with 1 M $NaPF_6$/EC:PC electrolyte.

2.3.3. Structural study on $Na_3V_2(PO_4)_2F_3$ during cycle

The crystal structure changes of $Na_3V_2(PO_4)_2F_3$ accompanying the Na^+ extraction/insertion processes were investigated by performing an *ex-situ* X-ray diffraction study on the cathodes in an initial state, charged states up to 3.2 V, 4.1 V and 4.3 V, and a cycled state to 2.3 V. Fig. 18(a) shows the *ex-situ* XRD profile at the each point. All peaks were indexed in the space group *P*42/*mnm*. The obtained data of XRD pattern change suggested the charge and discharge process was carried out by solid solution reaction, and the diffraction peaks of the cathode at the end of the first cycle (charged and then discharged) (Fig. 18(a-5)) were back to almost the same position as that of the initial electrode (Fig. 18(a-1)). Table 7 gives the refined cell parameters of the four phases at the state of the initial, 4.0 V and 4.3 V charge, and 2.3 discharge (1cycle).

Both *a* and *b* decreased during charge (Fig. 18(a-2, a-3 and a-4)) and increased after the first cycle (Fig. 18(a-5)), while the *c* shrank contrary to the behaviors seen in *a* and *b*. Enlarged *ex-situ* XRD profiles are show in Fig. 18(b). During charge (Fig. 18(b-2, b-3 and b-4)), the (00c) peak shifted to lower angles, and the other reflections without involvement from *c*-axis were shifted toward wider angles. This anisotropic lattice behavior on cycling arisen from coulomb repulsive force between oxygen layers along *a*-*b* plane as a result of Na^+ extraction in the two-dimensional Na^+ sheets (Fig. 19). The lattice volume changes listed in Table 7 were small less than 2.5% despite of large Na^+ extraction and insertion, leading its good cycle performance.

Table 7. Lattice parameter $Na_3M_2(PO_4)_2F_3$ at initial state, charged states up to 4.1 V and 4.3 V, and a cycled state to 2.3 V.

Lattice parameter	ICDD	Initial	4.0 V	4.3 V	2.3 V
a = *b*	9.047(2)	9.038 (1)	8.91(1)	8.886(1)	9.0294(6)
c	10.705(2)	10.727(1)	10.779(1)	10.830(2)	10.725(1)
Cell volume	876.2(3)	876.2(3)	855.7(2)	855.2(2)	874.4(2)
Δv (%)			-2.3	-2.4	-0.2

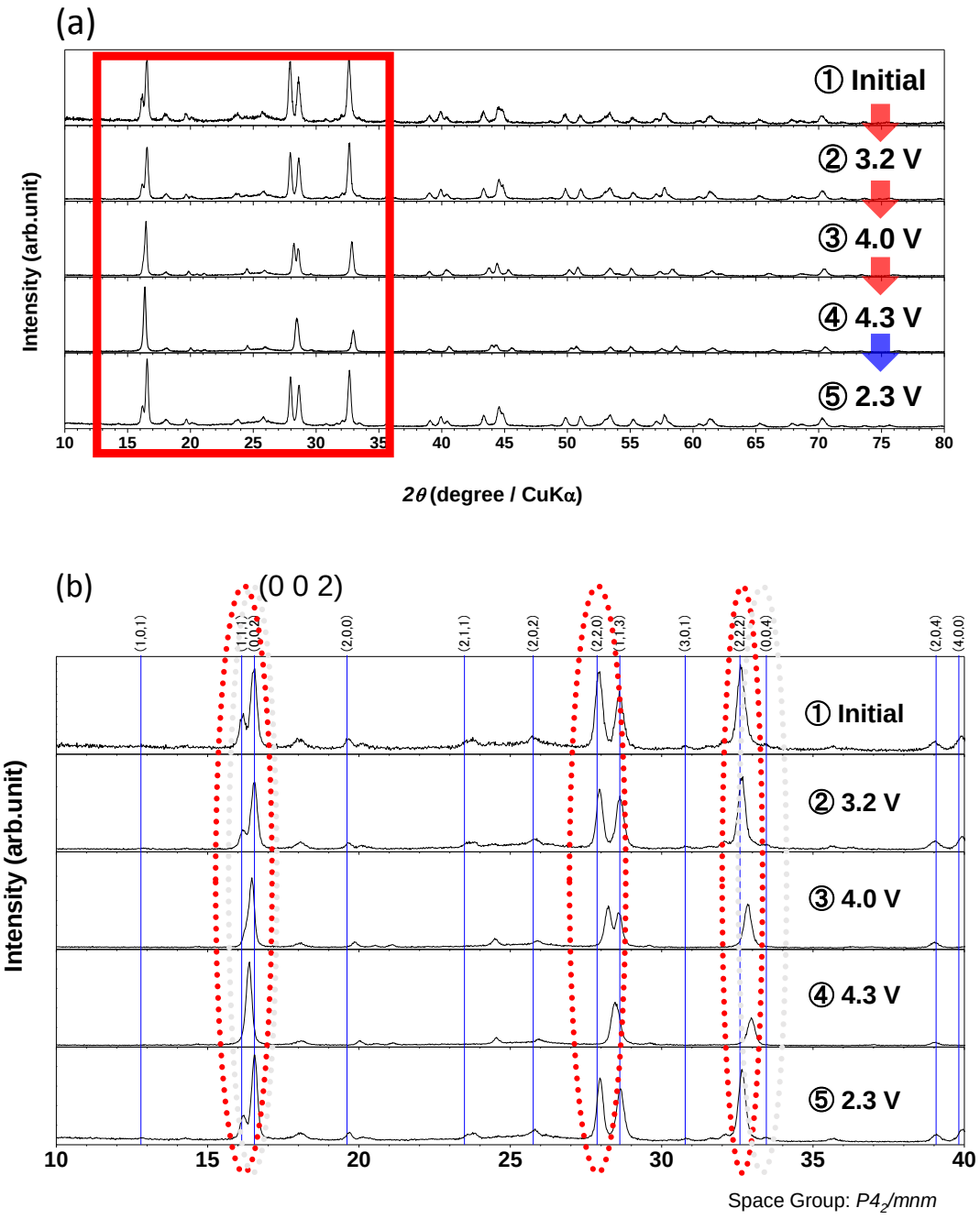

Figure 18. (a) *Ex-situ* XRD patterns of the electrodes at an initial state, charged states up to 4.1 V and 4.3 V, and a cycled state to 2.3 V. (b) The enlarged profiles of *ex-situ* XRD patterns. Red circles indicate the change of the diffraction peaks involving (00c) diffraction.

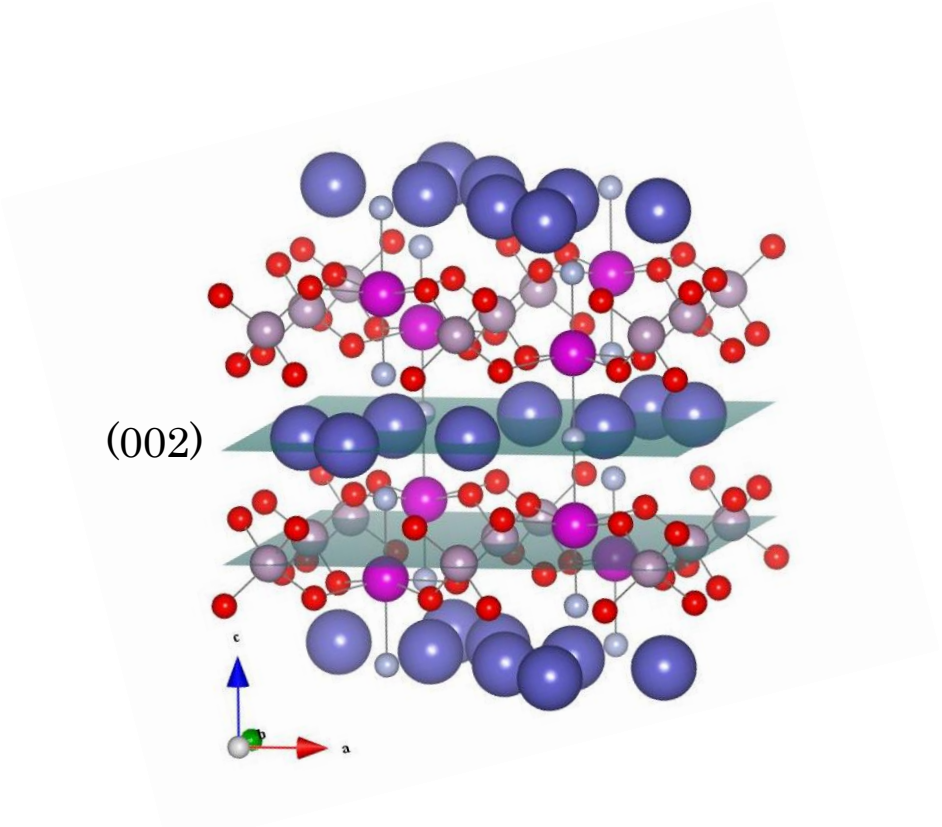

Figure 19. (002) Na layers in $Na_3V_2(PO_4)_2F_3$.

To simulate extractable sodium ions, we built 1 or 2 Na^+-extracted $Na_3V_2(PO_4)_2F_3$ models by removing the four Na1 or Na2 atoms from the tetragonal unit cell and performed structure optimization by VASP (Fig. 20(a)). When removing the 1 Na atom from $Na_3V_2(PO_4)_2F_3$, the calculated lattice energies in the cases of pattern 1 (1 Na^+ extraction from Na1 site) and pattern 2 (1 Na^+ extraction from Na2 site) were -1006.00 kJ mol^{-1} and -1009.05 kJ mol^{-1}, respectively. This result suggested that the Na at Na2 site is more extractable than that of Na1 site in the viewpoint of the structure energy. Figure 20 (b) shows simulated XRD patters based on the patterns 1 and 2, and experimental XRD patterns of electrochemically sodiated $Na_3V_2(PO_4)_2F_3$ for 1 Na are shown in Fig. 20(c). As comparison of experiment and simulated XRD patterns, obvious difference was seen in the diffraction peak at ca. 12^0, and experimental pattern was close to the pattern obtained by simulating based on the pattern 2.

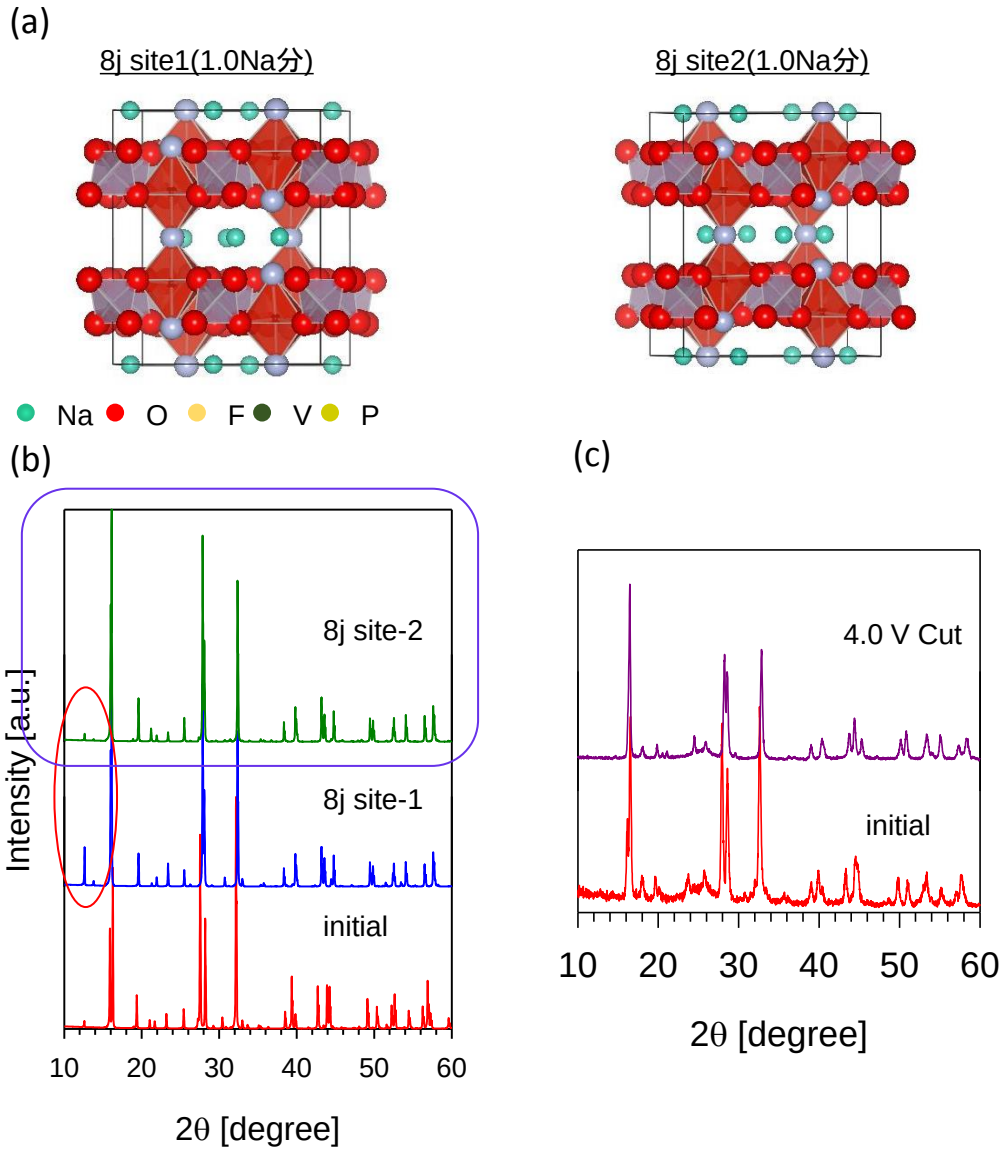

Figure 20. (a) 1 Na^+-extracted $Na_3V_2(PO_4)_2F_3$ models by removing the four Na1 or Na2 atoms from the tetragonal unit cell. (b) Simulated XRD palters based on the patterns 1 and 2, and (c) experimental XRD patterns of $Na_3V_2(PO_4)_2F_3$ at the state of initial and electrochemically sodiated for 1 Na.

2.4. Conclusion

$Na_3M_2(PO_4)_2F_3$ [M = Ti, Fe, V] was prepared by a conventional solid-state synthesis and their electrochemical properties were evaluated in Na half cells. The charge/discharge capacity of $Na_3Ti_2(PO_4)_2F_3$, $Na_3V_2(PO_4)_2F_3$ and $Na_3Fe_2(PO_4)_2F_3$ were 57.7 mAh g^{-1}, 120 mAh g^{-1} and 28 mAh g^{-1}. Especially, $Na_3V_2(PO_4)_2F_3$ exhibit repeatable 2 Na^+ extraction/insertion reaction with two-step discharge voltage plateaus at 4.1 V and 3.6 V. $Na_3V_2(PO_4)_2F_3$ was further investigated in Na full cell configuration with $NaTi_2(PO_4)_3$ and hard carbon anode, achieving promising performance as cathode materials for SIBs. One of the reason for this good electrochemical properties of $Na_3V_2(PO_4)_2F_3$ lays on its open structure characteristic, resulted in less than 2.5% volume change after large Na^+ ion extraction.

Chapter 3. Study on Electrochemical Property of $Na_2C_6O_6$ for Na-ion Batteries

3.1. Introduction

LIBs have been widely used due to their broad applicability as a power storage for portable electronic devices and electric vehicles. However, commonly used cathodes for LIBs such as $LiCoO_2$ are synthesized from limited mineral resources, and thus miner-metal free or low-cost materials that can be derived from more abundant resources have become increasingly desirable along with the world's growing demand. As a strategy to solve this ecological concern, researchers have devoted themselves to find new battery technology with using alternative materials. Among them, sodium-inserted materials and organic compounds are considered to have great advantages because they are obtained from abundant materials and free of rare metals. In addition, as already mentioned in Chapter 1, multi electron reactions originating from functional grope would bring large capacity. Organic materials could become strong candidates for SIBs not only due to cost aspect but also their low density and stacking structure which would be able to accept repeated insertion and extraction of the large sodium-ion. However, organic materials usually require a high volume of carbon as a conductive material, because most of them are regarded as insulators due to lack of free electrons. Organic semiconductors are exception and they generally consist of π conjugated chains with alternating C-C single and double bonds, and this chain formation brings conductivity. Hence, in the selection of organic cathode materials for secondary batteries, it would be reasonable to search a candidate from π conjugated compounds.

A π-conjugated compound of $Li_xC_6O_6$ was reported as a cathode active material for

LIBs in 2007 [106], and it have shown a stable reversible capacity around 300 mAh g^{-1}. $Li_xC_6O_6$ has larger gravimetric and volumetric capacities than those of commonly used inorganic lithium-inserted materials such as $LiMn_2O_4$ and $LiFePO_4$. Figure 21 shows the $Na_2C_6O_6$ structure based on a report registered in ICSD (No: 170805) [107]. In this structure, layers of hexagonally packed Na^+ alternate with layers of similarly packed $C_6O_6^{2-}$, where Na^+ lies *a*/4 above $C_6O_6^{2-}$. All sodium cations are coordinated by 8 O atoms from four different rhodizonate dianions, forming a layer structure with delocalized π-electrons that can be suitable for the Na^+ insertion/extraction.

In this chapter, a sodium-organic coordinated compound, $Na_2C_6O_6$ is discussed as a cathode active material for SIBs and its feasibility for practical use is further evaluated in a full cell configuration.

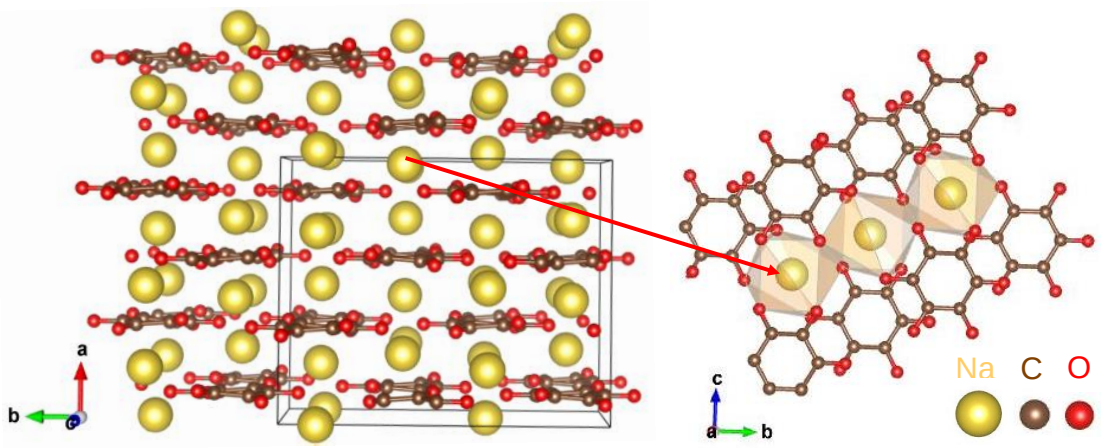

Figure 21.Crystal structure of $Na_2C_6O_6$. [106]

3.2. Experimental

Electrode preparation for electrochemical measurement

$Na_2C_6O_6$ was purchased and used without further purification. For the electrochemical studies, the 70 wt. % $Na_2C_6O_6$ powder was first dry-ball-milled with 25 wt. % acetylene black (AB, DENKA) under an Ar condition. The $Na_2C_6O_6$/C composite powder was mixed with 5 wt. % polyvinyl difluoride (PVDF, Kureha Corp.) binder in N-methylpyrrolidone (NMP, Wako Pure Chemical Industries, Ltd.). The obtained slurry was coated on Al sheets, dried under a vacuum at 80˚C for 30 min and cut to a diameter of 10 mm. The disc was then dried under a vacuum at about 110 ˚C overnight before assembling cells. The electrochemical performance of $Na_2C_6O_6$ was evaluated using a 2032 coin-type cell with a non-aqueous electrolyte (1 M $NaClO_4$/PC; Tomiyama Pure Chemicals Industries, Ltd.) and a polypropylene separator (model 3501; Celgard) against Na metal (Sigma-Aldrich). To avoid any influence from air, all cell-assembling processes were conducted in an Ar-filled glovebox. The electrodes were approximately 4 mg in total weight (including about 2.8 mg of $Na_2C_6O_6$ as an active material) and 10 mm in diameter. The discharge/charge measurements were carried out in galvanostatic mode with a current rate of 0.1C based on the practical capacity at second discharge of ca. 180 mAh g^{-1}. For investigating electrochemical performance of $Na_2C_6O_6$ under the condition with less conductive carbon additives or even without AB, $Na_2C_6O_6$ powder and AB were hand-milled for 15 min and the carbon pellet electrodes were fabricated with PTFE. The pellets were punched in the form of disks with approximately 15 mg in weight and 10 mm in diameter. The coin cell was assembled as described above, and the discharge/charge measurement was carried out in galvanostatic mode with a current rate of 0.2 mA cm^{-2}. For rate performance measurement, the discharge/charge current density was set to 0.1C

for the first cycle and then changed to 0.2C, 0.5C, 1C, 2C and 5C with a single cell. All the discharge/charge tests were measured at 25 ˚C.

Cell preparation for electrochemical study in the sodium-ion cell configuration

Anodes of non-graphitazable carbon, such as hard carbon, for SIBs have been developed by several groups and its electrochemical properties [12, 108] and the electrochemical insertion mechanism [109] have been well studied. Since the $Na_2C_6O_6$ cathode has to be started from discharging, A Na-containing hard carbon anode is necessary to clarify characteristics of $Na_2C_6O_6$ in a sodium-ion cell configuration. Hard carbon named as C1600 was obtained by Sumitomo Chemical Co., Ltd. and [103] and Na-predoped hard carbon was prepared thereof as follows: 95 wt. % hard carbon was mixed with 5 wt. % PVDF or carboxymethyl cellulose ammonium salt (CMC, Sigma-Aldrich) binder in NMP or purified water, respectively. The obtained slurry was coated on Cu sheets, dried under a vacuum at 100 ˚C for 30 min and cut to a diameter of 15 mm. After the electrodes were dried under a vacuum at about 110˚C overnight, the electrode was introduced into the Ar-filled glovebox. Na metal was sliced into a disc-shape with diameter of 15 mm and weight of more than 1.47 mg. They were placed directly on the hard carbon electrode, and then the two were placed together into a laminate pack with 1M $NaClO_4$/PC. The laminate pack was sealed with heat to avoid electrolyte deterioration. After 1 to 14 days, the electrode was taken out from the pack and washed with dimethyl carbonate (DMC, Tomiyama Pure Chemicals Industries, Ltd.). The pictures of Na-predopoing process are presented in Fig.22. Electrochemical measurements for the obtained Na-predoped hard carbon were studied in both half- and full-cell configurations. Weight of the hard carbon electrode was approximately 6 mg in total mass (including

about 5.7 mg of hard carbon as an active material) and 15 mm in diameter. The charge/discharge measurement was carried out in galvanostatic mode. In the half-cell configuration, a current rate was set to 0.1C based on the practical capacity of 300 mAh g^{-1}. The specific capacity (mAh g^{-1}) was calculated based on the mass of the pristine hard carbon anode.

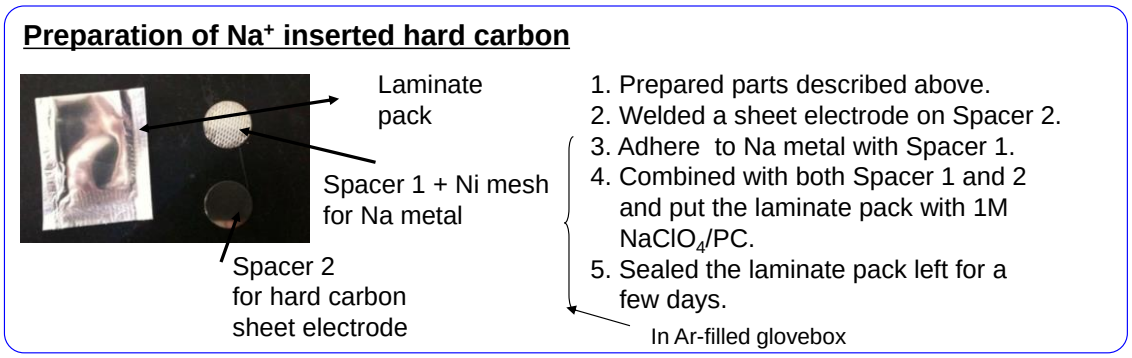

Figure 22. Description of preparation for Na^+ predoped hard carbon.

Synthesis of $Na_2C_4O_4$ and $Na_2C_5O_5$ and Electrochemical measurement

$H_2C_4O_4$ (D/399, >98 %) and $H_2C_5O_5$ (C1483, >98%) were purchased from Tokyo chemical industry Co., Ltd. $Na_2C_4O_4$ and $Na_2C_5O_5$ were synthesized by following substitution reaction; $H_2C_xO_x + 2NaOH \rightarrow Na_2C_xO_x + H_2O$ [x = 4 and 5] as described in the patent [110]. $Na_2C_6O_6$ (Marek KGaA, > 90%) and $K_2C_6O_6$ (Wako pure chemical industries, Ltd. , > 95%) were purchased and used without further purification.

The prepared $Na_2C_XO_X$ [x = 4 and 5] and purchased $K_2C_6O_6$ powders were first dry-ball-milled with acetylene black (AB) (DENKA Co., Ltd.) under an Ar condition with the weight ratio of active material : AB = 70 : 25. The active material and carbon composite powders were mixed with 5 wt% Polytetrafluoroethylene (PTFE) binder to fabricate pellet electrodes with a diameter of 10 mm. The obtained pellets were then dried under

ca. 110 ˚C overnight before assembling cells. The electrode was electrochemically sodiated and disodiated with a non-aqueous electrolyte of 1M $NaPF_6$/PC (Kisida Chemical Co., Ltd.) or 1M $NaClO_4$/PC (Tomiyama Pure Chemicals Industries, Ltd.) and a polypropylene separator (model 3501; Celgard, LLC.) against Na metal (Sigma-Aldrich Co. LLC.) in a 2032 coin-type cell. Electrochemical measurements for the cells were carried out in galvanostatic mode under the constant current of 0.2 mA cm^{-2}. In order to prepare samples for investigation of structure changes after sodiation and desodiation, the electrochemical measurement was stopped at pre-set voltage, and the charged or discharged electrodes were carefully taken out from the cells after being left for 24 h in the cells to reach an equilibrium state. After aging, the electrodes were washed and soaked in dimethyl carbonate (DMC, Tomiyama Pure Chemicals Industries, Ltd.). They were then dried in the Ar-filled grove- box under vacuum.

3. 3. Results and discussion

3.3.1. Electrochemical properties of $Na_2C_6O_6$

The discharge/charge cycle of $Na_2C_6O_6$ was carried out with the various voltage ranges between 1.0 and 3.2 V. Figure 23 (a) - (d) shows the first and second discharge/charge curves of $Na_2C_6O_6$ within the voltage range of 1.0 - 3.2 V, 1.0 - 2.9 V, 1.5 – 3.2 V, and 1.5 - 2.9 V, respectively. The plateau appeared at 2.0 V in the first discharge process and the profile changed to stepwise curves from the following charge. The first discharges were over 200 mAh g^{-1} in all voltage range, and repeatable 2.6 Na insertion/extraction of 320 mAh g^{-1} was confirmed in the voltage range of 1.0 – 3.2 V. Overall electrochemical properties were promising results accompanying multi electron reaction, and the over voltage gap between charge and discharge was relatively smaller compared to that of

inorganic materials. The electrochemical characteristics of multi electron reaction and small voltage gap would be a one of the advantage originative from organic nature in low density.

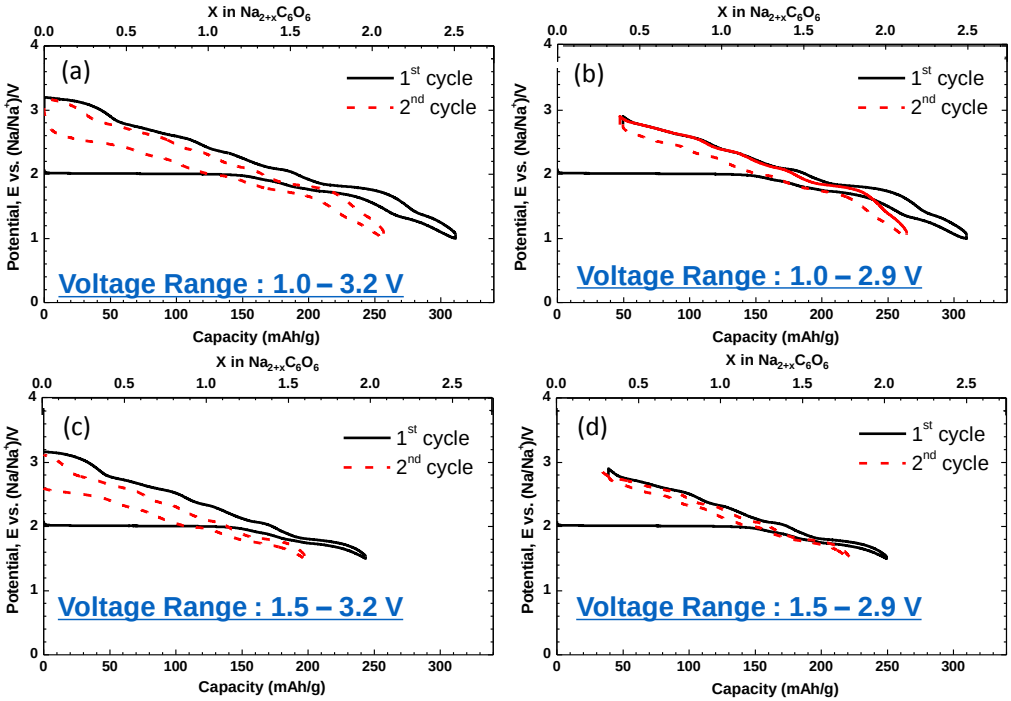

Figure 23. Charge and discharge profiles of $Na_2C_6O_6$ in (a)1.0 – 3.2 V, (b)1.0 – 2.9 V, (c)1.5 – 3.2 V, and (b)1.5 – 2.9 V. Electrolyte used is 1 M $NaClO_4$/PC in all cells and current density was 0.1C based on 2nd discharge capacity in 1.5 -2.9 V of 180 mAh g^{-1}.

Figure 24 shows the cycle performance of $Na_2C_6O_6$ with different cut off voltage, and good cycle performances were confirmed within the voltage range of 1.5 - 2.9 (or 2.8) V and 1.8 - 2.9 (or 2.8) V, while a gradual capacity fade was observed in cycle with the charge cutoff voltage above 3.2 V. Since the color of electrolyte and electrode turned red on charging over 3.2 V (Fig. 25), the capacity decrease war attributable to the dissolution of disodiated $Na_2C_6O_6$ to the organic electrolyte. In deeper discharge under 1.0 V, a

discharge capacity was also gradually decreased with repeating cycles, although there was no sign of dissolution of $Na_2C_6O_6$ after several cycles. However, the electrode became relatively easy to remove from the Al sheet after 1.0 V discharge. The adhesive property of the PVDF binder to hold $Na_2C_6O_6$ electrodes probably because of large volume expansion resulted from more than 2 Na^+ insertion. Unfortunately, $Na_2C_6O_6$ is very soluble in water and CMC type binder, which have been reported to have strong adhesion in Si anode materials, [111] is not able to be applied in the $Na_2C_6O_6$ electrode fabrication. It is thus necessary to find another binder with strong adhesion or electrolyte with low solubility of organic compounds. Although further modification of binder and/or electrolyte is required to achieve a better cycle performance in a large capacity range over 250 mAh g^{-1}, stable cycle performance of 180 mAh g^{-1} is confirmed.

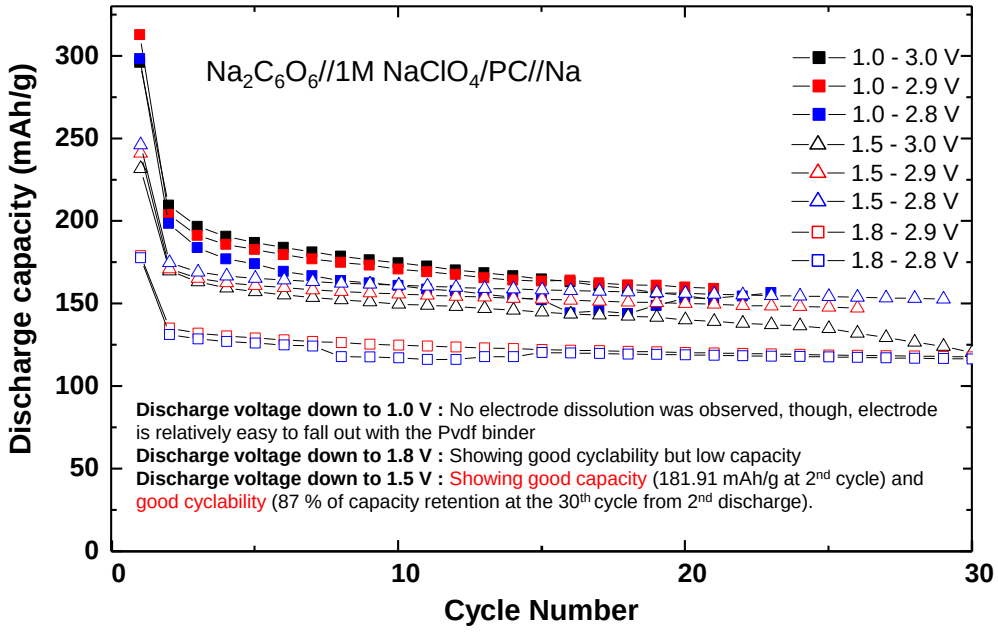

Figure 24. Cycle performances of $Na_2C_6O_6$ electrodes with variety cut off voltage range. Electrolyte used is 1 M $NaClO_4$/PC in all cells and current density was 0.1C based on 2nd

discharge capacity in 1.5 -2.9 V of 180 mAh g^{-1}.

Charged up to 2.9 V **Charged up to 3.2 V** **Charged up to 3.5 V**

Figure 25. Pictures of electrode and electrolyte condition after charging to 2.9 V, 3.2 V, and 3.5 V.

Conductivity is especially a big concern of organic cathode active materials and they usually require a high volume of carbon as a conductive material, which results in less total cell energy. In order to check conductivity and practicality of $Na_2C_6O_6$ as rechargeable batteries, the mass ratio of $Na_2C_6O_6$ powder : AB : binder was changed from 70 : 25 : 5 to 95 : 0 : 5 and 90 : 5 : 5. In this test, PTFE teflon binder (Daikin Industries) was used instead of PVDF, because it is easy to fabricate the cathode under carbon less condition. Figure 26 shows the discharge/charge profile of $Na_2C_6O_6$ electrodes with 25 wt. %, 5 wt. % and 0 wt. % AB. The first discharge capacities for 5 wt. % and no AB-added electrode were 229 mAh g^{-1} (Fig. 26 (b)) and 188 mAh g^{-1} (Fig. 26 (c)), respectively, which correspond to approximately 97 and 80 % of the discharge capacity obtained from 25 wt. % AB-added electrodes (Fig. 26 (a)). The obtained reversible capacity after 1st discharge for the 5 wt. % AB-added electrodes was almost same as that for 25 wt. % AB-added electrodes, and $Na_2C_6O_6$ was able to show the rechargeable capacity more than 90 mAh g^{-1} even in the AB-free pellet. Unlike other organic materials, [64, 65] the $Na_2C_6O_6$

electrodes functioned even in the configuration without any conductive carbon additives, and this property is quite rare among the organic active materials. Yamashita et al. performed DFT calculation and reported small HOMO-LUMO gap in $Na_2C_6O_6$. [112]

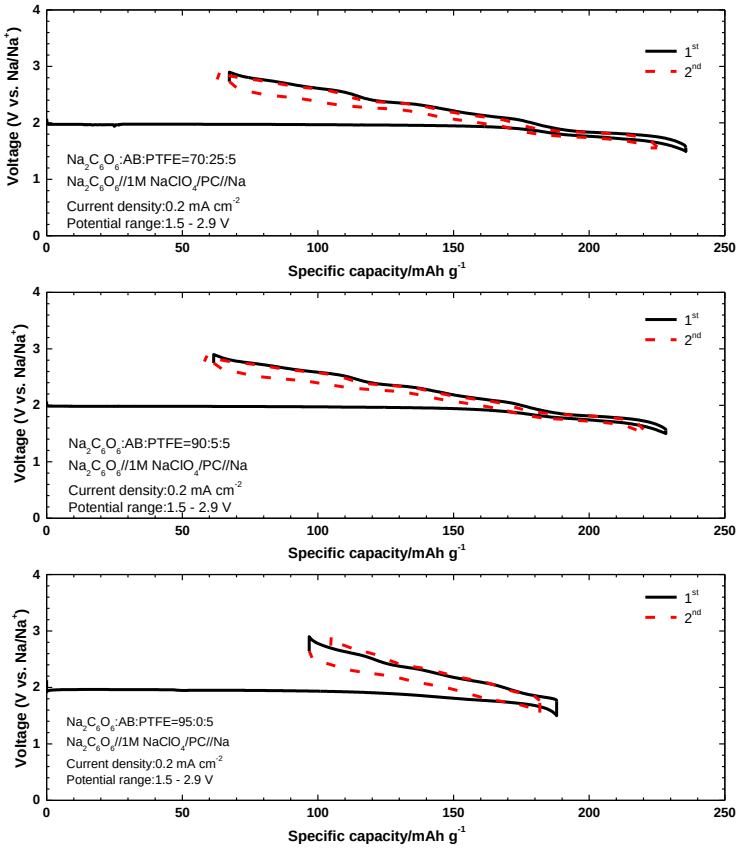

Figure. 26 Electrochemical performance of $Na_2C_6O_6$ with less or no AB. The weight ratio of active material:AB:PTFE was (a) 70:25:5, (b) 90:10:5, or (c) 95:5:5.

The rate capability of $Na_2C_6O_6$ was evaluated within the voltage range of 1.5 - 2.9 V. The test electrodes were adjusted to approximately 4 mg in total weight (including about 2.8 mg of $Na_2C_6O_6$ as an active material), and the current density for discharge was set to approximate rates of 0.2C, 0.5C, 1C, 2C and 5C, based on the second discharge capacity

between 1.5 - 2.9 V of 180 mAh g^{-1}, with the charge current density fixed at 0.1C. The discharge/charge measurement was performed in galvanostatic mode. Figure 27 shows the $Na_2C_6O_6$ discharge cycle performance with varying current rates against Na metal. $Na_2C_6O_6$ showed good rate capability and the discharge capacity at a rate of 5C was more than 87% of the discharge capacity with 0.2C. Given the practical usage of organic materials, this fast movability of Na^+ ions into/from $Na_2C_6O_6$ was strong feature as active materials for secondary batteries. The good rate performance would originate from not only the structural factor of $Na_2C_6O_6$ but also Na^+ interaction in electrolyte, surface and structure of $Na_xC_6O_6$. In the research on electrolyte, some additives have been investigated as an anion receptor to weaken Lewis-acids and Lewis-base interaction, bringing increase of conductivity in electrolyte and transport number of ion carriers. [113] Lewis acidity of Na^+ ion is, while, generally lower than that of Li, and hence lower Lewis acidity of Na^+ leads less interaction from Lewis base in electrolyte and interface, and probably Na^+ involves with less electrostatic attraction in the open structure, resulting in fast mobility and diffusion of Na^+ ions.

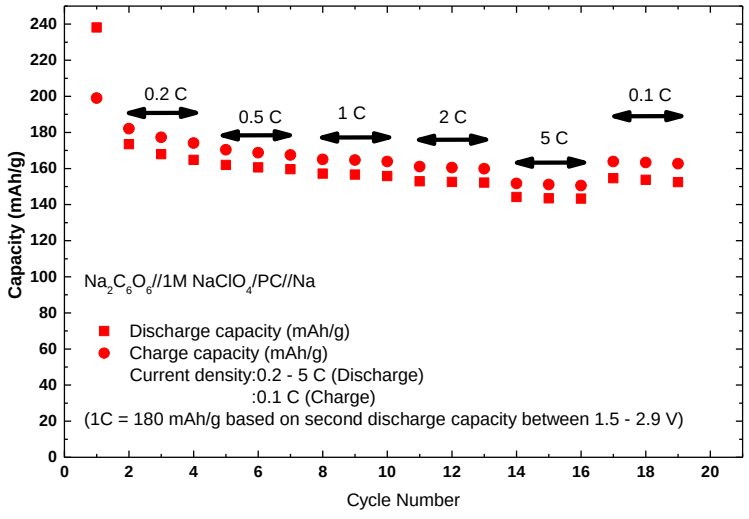

Figure 27. Rate performance of $Na_2C_6O_6$ between 1.5 – 2.9 V in Na cells.

3.3.2. Electrochemical properties of $Na_2C_6O_6$ in sodium-ion batteries

Na-predoped hard carbon electrodes were prepared as described in the experimental section, and its electrochemical properties against Na metal were evaluated. Figure 28 shows a typical discharge/charge profile of hard carbon, which was started from the Na^+ insertion. On the other hand, Fig. 29 (a-d) shows the charge/discharge profiles of Na-predoped hard carbon, which was started from Na^+ extraction. Na-predoped hard carbon showed almost the same profile as that from the second cycle of hard carbon, and consequently its irreversible capacity was small. The first charge capacity was not dependent on the immersion time or the amount of mounted Na metal but rather on the contact surface area between hard-carbon and Na metal. Any excessive predoped events were not observed even in the sample immersed for 14 days (Fig. 29 (d)), however, the best immersing time in terms of achieving a stable electrochemical performance was over 7 days (Fig. 29(c)). The reason for the voltage fluctuations during the 1^{st} charge in 3 days immersed samples was not clarified, however this phenomenon happened only when the following two conditions coincide; (i) if the distance between the separator and Na metal was close or Na metal anode was too thick, and (ii) if the open circuit voltage of the Na pre-doped hard carbon electrodes was close to 0 V. Therefore, we considered this unstable voltage fraction was due to Na metal rather than the Na-predoped hard carbon electrodes.

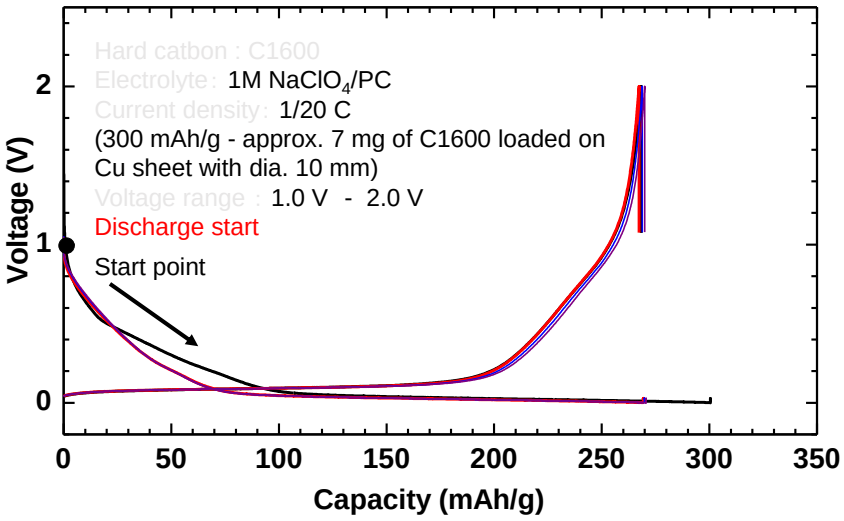

Figure 28. Typical charge and discharge profiles of hard carbon (C1600) in 2.0 – 0.1 V.

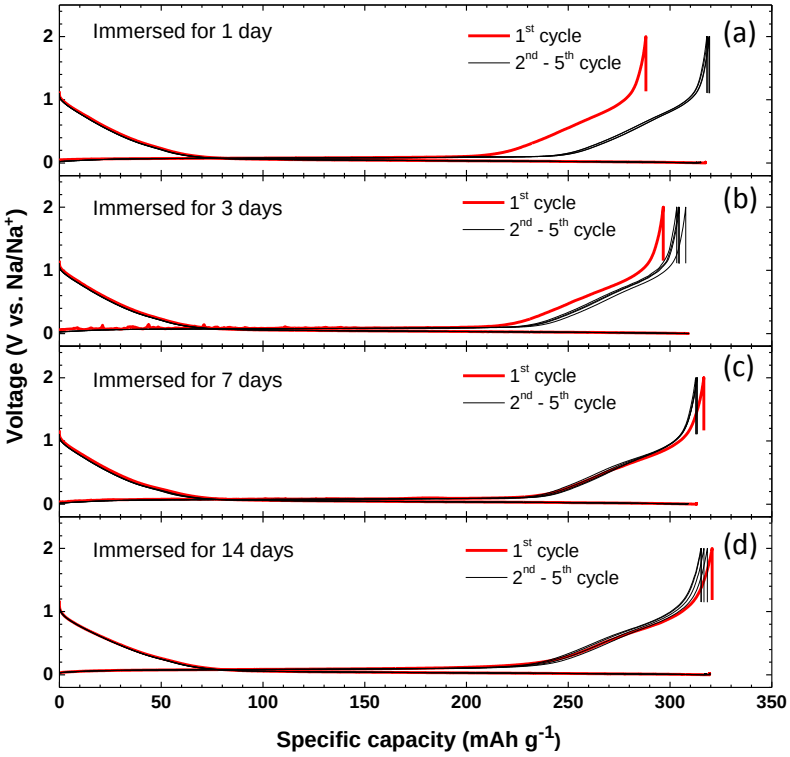

Figure 29. Charge and discharge profiles of predoped hard carbon (C1600) after being immersed in cells for (a) 1day, (b) 3days, (c) 7days, and (d) 14days. Voltage range and current density were set to 0.1 V - 2.0 V and C/20 based on 300 mAh g^{-1}.

$Na_2C_6O_6$ was coupled with the Na-predoped hard carbon anodes to configure a sodium-ion cell. The sodium-ion cell ($Na_2C_6O_6$/Na-predoped hard carbon) was cycled at a current density of 0.1C within the voltage range of 1.5 - 2.9 (or 2.8) V and 1.8 - 2.9 (or 2.8) V. The cathode-to-anode mass ratio was 1:1. In this configuration, the cell capacity was restricted by the cathode. Fig. 30 shows the discharge/charge profile of the $Na_2C_6O_6$/Na-predoped hard carbon sodium-ion cell with the typical discharge/charge profiles of Na-predoped hard carbon and $Na_2C_6O_6$ in a half cell against a Na metal anode. The irreversible capacity and charge/discharge over-potential were further reduced and better rechargeable performance was obtained in the full cell rather than in the half cell; the second discharge capacity was 179 mAh g^{-1}.

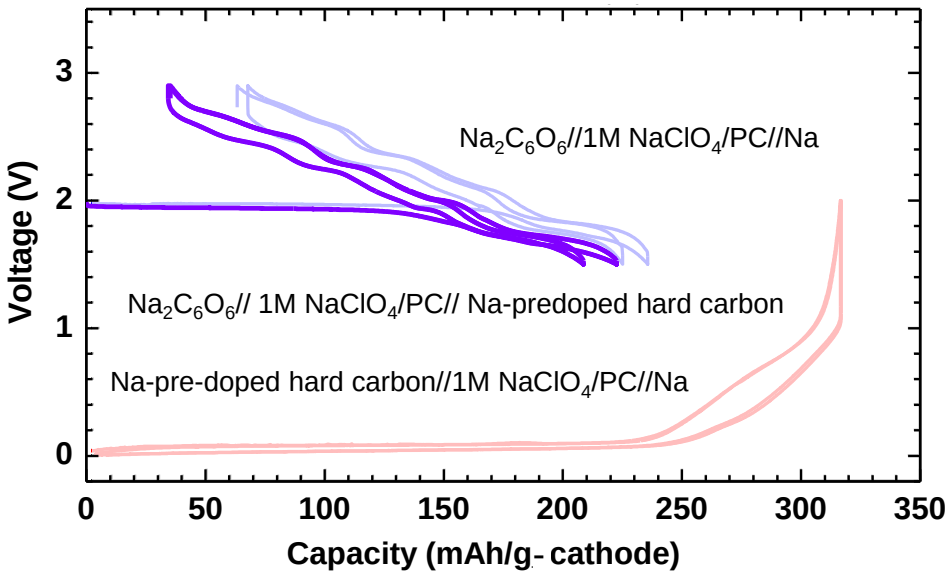

Figure 30. Charge and discharge profiles of $Na_2C_6O_6$//1M $NaClO_4$/PC//Na-predope hard carbon. Voltage range and current density were set to 1.5 V – 3.0 V and C/20 based on 180 mAh g^{-1}. The charge and discharge profiles of $Na_2C_6O_6$ and Na-predoped hard carbon in Na cells are also presented as reference.

The stable cyclability around 170 mAh g^{-1} of the cathode in this sodium-ion cell configuration was also confirmed with capacity retention of 85%, even at the 40th cycle of the prolonged discharge/charge measurement within 1.5 - 2.8 V (Fig. 31). Disodium rhodizonate showed multi-electron reaction and surprisingly high sodium ion movability in charge and discharge processes, promising outcome as a cathode material for SIBs. These results have shown the possibility of organic active material for SIBs, especially in functionality of oxocarbonyl-based active materials. Hence, $Na_2C_6O_6$ analogs of $Na_2C_5O_5$, $Na_2C_4O_4$, and $K_2C_6O_6$ were evaluated as new cathode active materials for additional works and their cathode performance are compared in half cell configuration.

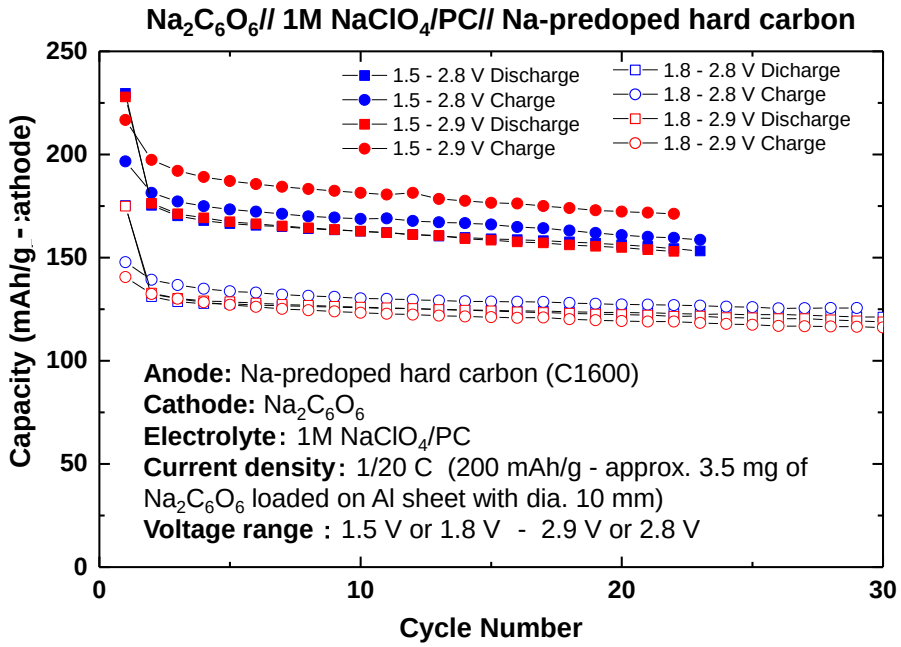

Figure 31. Cycle performance of $Na_2C_6O_6$// 1M NaClO4/PC// Na-predoped hard carbon ion cells.

3.3.3. Electrochemical properties of $Na_2C_6O_6$ analog of $Na_2C_5O_5$, $Na_2C_4O_4$, and $K_2C_5O_5$.

Electrochemical properties of $Na_2C_xO_x$

Figure 32 (a - c) shows the discharge and charge profiles of $Na_2C_xO_x$ [x = 4, 5, and 6] against Na metal in 1 M $NaClO_4$/PC. The cut off voltage ranges were optimized to 0.1 - 2.0, 1.0 - 2.0, and 1.5 - 2.9 V for $Na_2C_4O_4$, $Na_2C_5O_5$, and $Na_2C_6O_6$, respectively. $Na_2C_4O_4$ showed first discharge capacity of ca. 100 mAh g^{-1} with a small plateau at 0.6 V and $Na_2C_4O_4$ was not electrochemically active in the following cycles. While, $Na_2C_5O_5$ and $Na_2C_6O_6$ delivered large first discharge capacity of 207 mAh g^{-1} and 236 mAh g^{-1} corresponding to $1.44Na^+$ and $1.89Na^+$ insertion, respectively. Although $Na_2C_6O_6$ showed excellent reversibility as already mentioned, its irreversible capacity was relatively large. On the other hand, $Na_2C_5O_5$ exhibited smaller irreversible capacity than that of $Na_2C_6O_6$, and showed the good cyclability as shown in Fig. 33. In the dQ/dV curves in Fig. 34 (a) and (b), large reductive peaks appeared at 1.5 V for $Na_2C_5O_5$ and 1.97 V for $Na_2C_6O_6$, and several corresponding oxidative peaks were seen in the following charge process. After the first cycle, the reversible reductive/oxidative redox peaks were observed in the both cathodes and each polarization between the anodic/cathodic peaks was less than 0.2 V. A promising result was obtained in the energy efficiency, $Na_2C_6O_6$ and $Na_2C_5O_5$ can be therefore deemed as attractive active materials for secondary batteries. Their congestive C=O carbon-oxygen double bonds should serve as a redox center to promote charge and discharge processes in those materials. Although all $Na_2C_xO_x$ [x = 4, 5, and 6] oxocarbons have C=O bonds, they exhibited different electrochemical performance including redox potential, suggesting an anion formula influences to its electrochemical behavior.

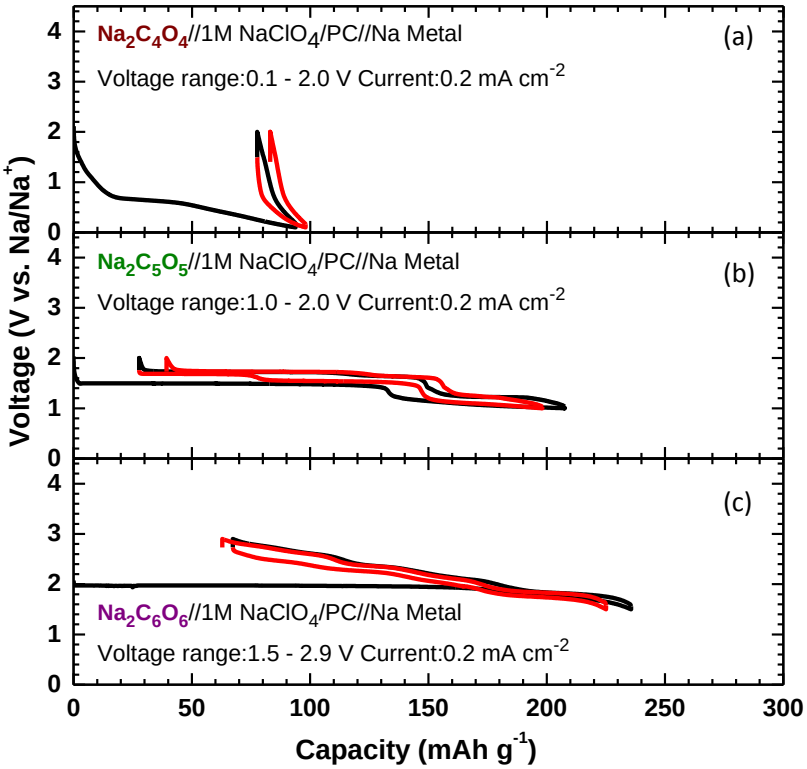

Figure 32. Charge and discharge profiles of (a) $Na_2C_4O_4$, (b) $Na_2C_5O_5$, and (c) $Na_2C_6O_6$ with 1M $NaClO_4$/PC electrolyte in Na cells.

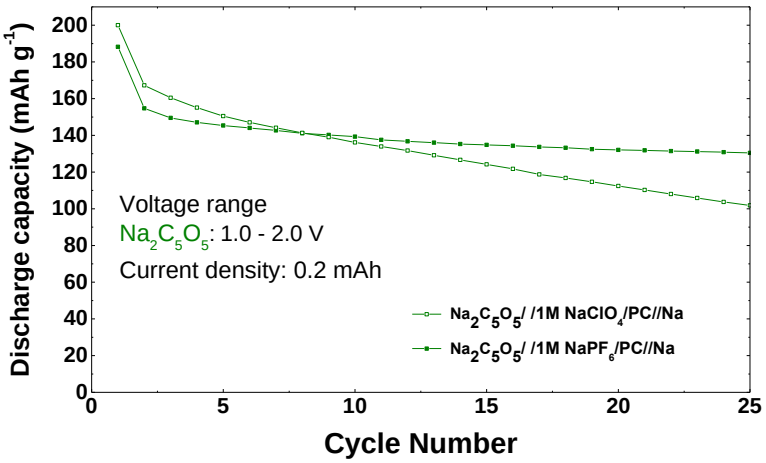

Figure 33. Cycle performance of $Na_2C_6O_6$ with 1M $NaClO_4$/PC and 1M $NaPF_6$/PC electrolytes.

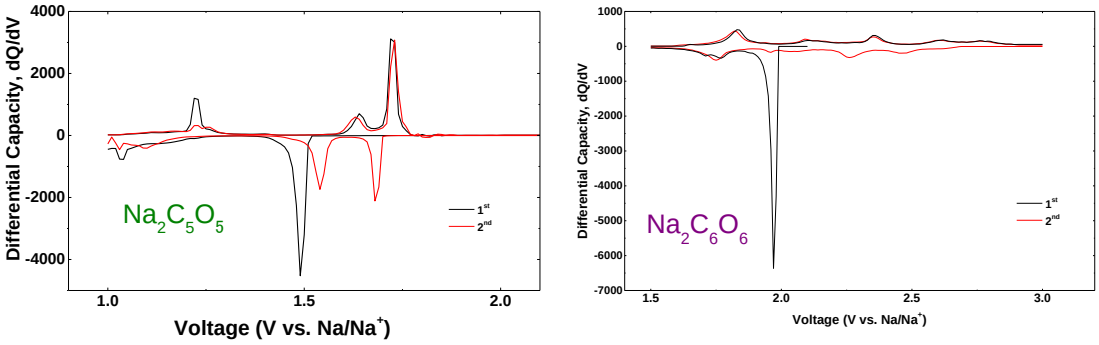

Figure 34. dQ/dV curves of $Na_2C_5O_5$ in 1.0 - 2.0V and $Na_2C_6O_6$ in 1.5 - 2.9 V.

Electrochemical properties of $Na_2C_6O_6$ and $K_2C_6O_6$

Not only $Na_2C_6O_6$ but also $K_2C_6O_6$ is historically significant as one of the oldest synthetic organic compounds [114-117] and they have been well-known materials as a series of a rhodizonate salt due to their unique resonance-stabilized structure. However, $K_2C_6O_6$ has received less attention as functional materials until recently [118]. Figure 35 compares electrochemical property of $Na_2C_6O_6$ and $K_2C_6O_6$ in 1M $NaClO_4$/PC electrolyte. The discharge cutoff voltage was set down to 1.0 V in both cases. The first discharge capacity of $Na_2C_6O_6$ increased to 312 mAh g^{-1} corresponding to 2.5 Na^+ insertion, and reversible capacity reached to 267 mAh g^{-1} of more than 2 Na^+ reaction. Although the capacity decreased after few cycles, $Na_2C_6O_6$ displayed an attractive feature of large capacity as cathode materials. On the other hand, $K_2C_6O_6$ showed large reversible capacity more than 200 mAh g^{-1} and small irreversible capacity compared with $Na_2C_6O_6$, however its capacity continuously decreased on cycles.

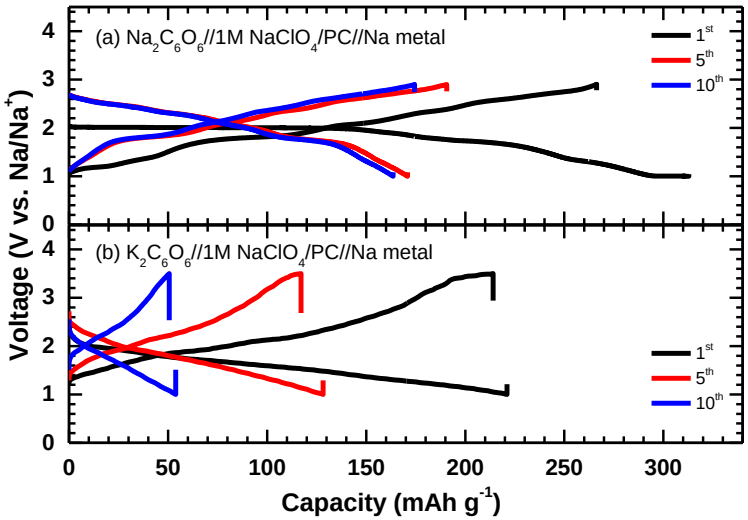

Figure 35. Charge and discharge profiles of (a) $Na_2C_6O_6$ and (b) $K_2C_6O_6$. $Na_2C_6O_6$ and $K_2C_6O_6$ were charged and discharged in 1.0 - 2.9 V and 1.0 - 3.5 V, respectively, with 1M $NaClO_4$/PC and Na metallic anode.

The difference observed in the electrochemical performance among $Na_2C_6O_6$ analogs suggested that the cathode properties depend on both of the anion and cation in $A_2C_xO_x$ rhodizonate-type cathodes although their electrochemical redox reactions would originate to the C=O functional group. As for the cation difference, similar difference have been also observed even in inorganic materials such as $LiCoO_2$ and $NaCoO_2$ [11, 119].

3.4. Conclusion

The electrochemical performances of $Na_2C_6O_6$ were investigated as an organic cathode for SIBs. In general, organic compounds are not suitable for cathode active material, because of the poor conductivity and low density. However, $Na_2C_6O_6$ well functioned as a host for Na^+ insertion and it exhibited good electrochemical properties even without conductive additives. The repeatable capacity of 170 mAh g^{-1} was confirmed at an

average working voltage of 2.18 V. The energy density about 370 $mWhg^{-1}$ was almost comparable to conventional inorganic cathode active materials for LIBs. Hence the minor-metal free $Na_2C_6O_6$ can be considered as a promising cathode candidate for SIBs with low cost. In addition, electrochemical properties of oxocarbon Na_2CxOx [x = 4 and 5] and $K_2C_6O_6$ were studied as cathode active materials for SIBs, and we confirmed rechargeable multi-electron reaction of $Na_2C_5O_5$ with delivering the large discharge capacity of 180 mAh g^{-1}. $Na_2C_5O_5$ showed stable cycle performances with small discharge/charge over-potential. $Na_2C_5O_5$ can be also deemed as very attractive active materials for SIBs, while $Na_2C_4O_4$ and $K_2C_6O_6$ were less attractive as active materials for secondary batteries.

Chapter 4. Structural Change of $Na_2C_6O_6$ through Electrochemical Reaction in Sodium-ion Battery

4.1. Introduction

LIBs have been widely used due to their broad applicability for a power storage, however, LIBs have been composed of costly elaborated materials including cathodes such as $LiCoO_2$, and hence low-cost materials without minor-metal have become increasingly desirable in association with the world's growing demand for LIBs. Under this circumstances, SIBs have now attracted attention after 20 years of the discovery on electrochemical sodium extraction/insertion from/into Na_xCoO_2 in 1980's [9, 14]. In contrast with inorganic materials, a few organic materials have been studied as the host for sodium insertion/extraction so far. Given the crystal structure of organic materials, some organic compounds displaying π-stacking interactions would provide a space for large sodium ions, which may serve as a new host for SIBs. Since the redox chemistry has been well understood in the six-membered ring compound, we have focused on sodium rhodizonate ($Na_2C_6O_6$) as a new electrode active material for SIBs [66] and demonstrated its promising electrochemical property including its exceptionally high conductivity in charge and discharge processes. Since monocyclic oxocarbon anions including deltate, squarate, croconate, and rhodizonate have been recognized as members of an aromatic series and they are stabilized by electron delocalization of π-electron around the ring, [114, 120] the electrochemical performance of $Na_2C_4O_4$, $Na_2C_5O_5$, and $K_2C_6O_6$ were investigated as additional works for search new organic active materials in the previous chapter. $Na_2C_4O_4$ was almost no electrochemically active in the Na system and $K_2C_6O_6$ did not show stable cycle performance, while $Na_2C_5O_5$ and $Na_2C_6O_6$ shows large reversible capacity close to 200 mAh g^{-1}. The dQ/dV curves of $Na_2C_5O_5$ and

$Na_2C_6O_6$ exhibited large reductive peaks appear 1.97 V for $Na_2C_6O_6$ and 1.5 V for $Na_2C_5O_5$, and several oxidative peaks appeared in corresponding charge process. Each of those oxocarbon has possessed characteristic charge and discharge profiles although their electrochemical redox reaction are all considered to be driven by C=O functional groups, remaining a question whether there is a factor to determine their electrochemical performance besides chemical redox activity. Although organic active materials have long history, the investigation on electrochemical mechanism have been less actively discussed compared to inorganic materials. Their electrochemical redox behaviors in cells are usually explained by chemical reaction based on a single molecules. For example, electrochemical behaviors of $Na_2C_6O_6$ should be able to be fully explained by carbon-oxygen double bonds in a conjugated system. The presenting charge and discharge profiles, however, are rather complicated than the other organic materials with C=O redox functions such as the terephthalate materials. [64, 65] These terephthalate electrodes exhibit flat plateaus corresponding to redox reaction of carbon-oxygen double bond, while $Na_2C_6O_6$ has step wise profiles after 1st discharge. Moreover, the research on carbonyl compounds is mainly focusing on the exploration for new materials and the improvement of their electrochemical performance, and there are limited comprehensive works on changes in crystal structures and redox functional groups of organic materials during charge and discharge.

In this work, the crystal and local structure change of $Na_2C_6O_6$ during charge and discharge were investigated by using X-ray powder diffraction (XRD), Fourier transform infrared spectroscopy (FT-IR), as well as solid state ^{23}Na and ^{13}C magic angle spinning nuclear magnetic resonance (MAS-NMR) in order to investigate detailed electrochemical sodium insertion and extraction process in $Na_{2+x}C_6O_6$.

4.2. Experimental

Sample Preparation

The electrode materials of $Na_2C_6O_6$ were prepared as described in Chapter 3. The fabricated pellet was then dried under about 110 ˚C overnight before assembling cells. The electrochemical test was carried out using a 2032 coin-type cell with a non-aqueous electrolyte (1 M $NaClO_4$PC; Tomiyama Pure Chemicals Industries) and a polypropylene separator (model 3501; Celgard) against Na metal (Sigma-Aldrich). The electrode was electrochemically sodiated and disodiated under the constant current of 0.2 mA cm^{-2} and stopped at different preset voltage. After 24 h to reach equilibrium, the charged or discharged electrodes were carefully taken out from the cells, washed, and soaked in Dimethyl carbonate (DMC, Tomiyama Pure Chemicals Industries) for 3 hours. They were dried in the Ar-filled grove box under vacuum. To avoid any influence from air, all process from cell-assembling to measurements were conducted in an Ar-atmosphere with using an Ar-filled glovebox, air tight transfer vessel and holder.

The *ex-situ* XRD measurements were performed for the various charged and discharged states using Cu-Kα radiation (50 kV and 300 mA) from 2 θ = 10 - 80° with 0.02° step scan at a rate of 0.15 ° min^{-1}. All of the *ex-situ* XRD data were taken under Ar condition using an air-tight specimen holder (Bruker) in order to avoid any influence from air. IR spectrum for discharged or charged $Na_2C_6O_6$ was recorded using a Jasco FT/IR 680 plus infrared spectrophotometer combined to attenuated total reflectance (ATR) technique. All spectrums were scanned for 200 times with resolution of 4 cm^{-1} and AB mixed with PTFE was used for background adjustment. ^{13}C solid NMR studies were carried out for the sodiated and disodiated $Na_2C_6O_6$ positive electrodes on a CMX-300 spectrometer with a magnetic field of 7.0 T. The resonance frequency was 75.2 MHz and

spinning speed was 10 kHz with 34.130 msec of acquisition time and 180 sec of pulsing delay at room temperature with DD/MAS. The chemical shift was referenced to ^{13}C signals of 1.56 ppm Polymethylsiloxane (1.56 ppm). ^{23}Na solid NMR studies were carried out on a ECA800 spectrometer with using a magnetic field of 18.8 T. The resonance frequency was 211.65 MHz and spinning speed was 18 kHz with 5.12ms of acquisition time and 2 sec of pulsing delay. The chemical shift was referenced to ^{23}Na signal of sodium chloride saturated-solution. All the samples for solid NMR were measured immediately after the cell disassembling process to avoid time-degradation of the sample.

4.3. Results and discussion

4.3.1. Structure evolution of $Na_2C_6O_6$ during charge and discharge process

Figure 36 shows a typical discharge/charge profile of $Na_2C_6O_6$ between 1.5 – 2.9 V and measurement points for all studies. The plateau appeared at 2.0 V during the first discharge, after which the profile changed to stepwise curves and same stepwise-profiles were repeatedly observed. The discharge and charge reaction can be divided into two parts as mentioned above, suggesting that $Na_2C_6O_6$ goes through two phase reaction during first discharge at the 2.0 V plateau and changes to a new phase between 1.8 and 1.5 V, and then either insertion or other reaction occurs during following cycles.

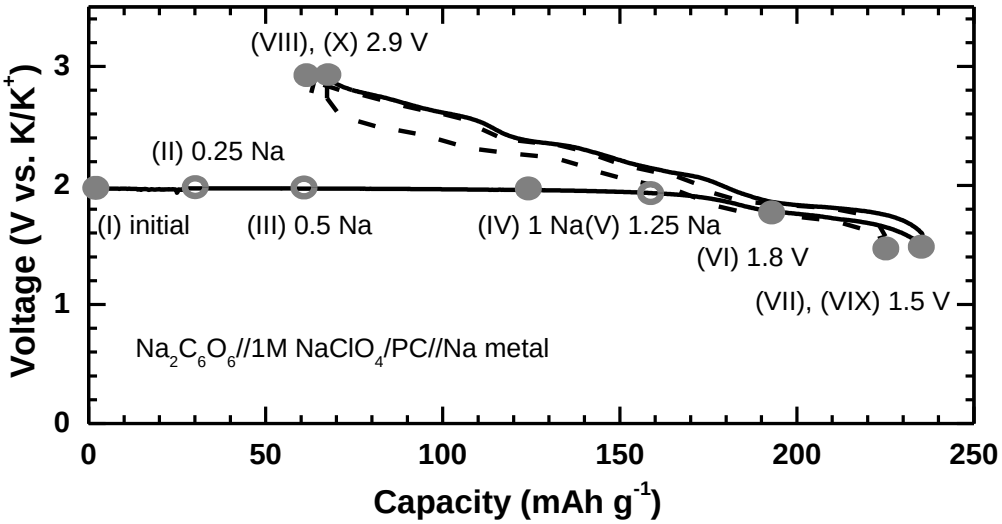

Figure 36. Charge and discharge profiles of $Na_2C_6O_6$ and measurement points for XRD, FT-IR, ^{23}Na and ^{13}C MAS-NMR. (I)-(III), (I), (IV) and (VI) – (X) are for XRD, (I) and (VII) – (X) are for FT-IR, and (V)- (X) are for MAS-NMR.

In order to investigate a phase evolution of $Na_2C_6O_6$ due to sodiation and desodiation, *ex-situ* XRD measurements were performed on the first and second cycles. Figure 37 shows the XRD profile patterns for charged and discharged $Na_2C_6O_6$ electrodes. For x > 2 region in $Na_xC_6O_6$, the coexistence of the 2 phases was seen as shown in Fig. 37(b). As for the pattern of $Na_2C_6O_6$ discharged for 1Na mol^{-1} (124 mAh g^{-1}) electrodes which was taken at the middle of plateau region at 2.0 V (Figure 36 (IV)), a new phase was detected with decrease of peak intensity from the original lattice (Fig 23 (a) and (b)). After discharge down to 1.8 V (Fig. 37(c)), the original disodium rhodizonate phase was disappeared and the flat discharge plateau was also lost (Fig. 36(V)). Then, the structure was totally changed to the new phase after being discharged down to 1.8 V. In the comparison of the *ex-situ* XRD patterns of $Na_2C_6O_6$ electrodes discharged at 1.8 V (Fig.

4(c)) and 1.5 V (Fig. 4(d)), their diffraction peaks took same 2θ positions with different intensity, implying difference in crystal growth orientation and/or distortion between the structure of the $Na_2C_6O_6$ electrodes discharge to 1.8 V and 1.5 V. Regarding the following charge process, the *ex-situ* XRD pattern of the electrode charged up to 2.9 V did not completely returned to the position of the original lattice (Fig. 37(e)). Consequently, the two-phase coexistence was confirmed only in the 2.0 V plateau region at the 1st discharge, and the following discharge and charge process would be carried out by solid solution like reaction, resulting in slope type charge and discharge curves with several steps. The XRD pattern of the electrodes at the following 2nd discharge and charge state (Fig. 36(VIV) and (X), respectively) were same as that of 1st 1.5 V discharged and 2.9 V charged states (Fig. 36(VII) and (VIII), respectively), implying the charge and discharge processes after 1st discharge were carried out based on the new phase as show in Fig. 37(d) – (g). We also checked the XRD profile for the condition in charging up to 3.2 V, and the intensity of the original peaks became stronger and any additional peaks were not observed. Two phase reactions are often observed in charge and discharge in organic materials and they are usually fully reversible. [64, 65, 70, 72] However $Na_2C_6O_6$ decomposed accompanying with coloration phenomenon before it completely returned to the original phase, although the structure kept being back to the original phase with charging. Actually, the XRD patterns of the charged state at 3.5 V was similar to that in the initial state, however the intensity was very small.

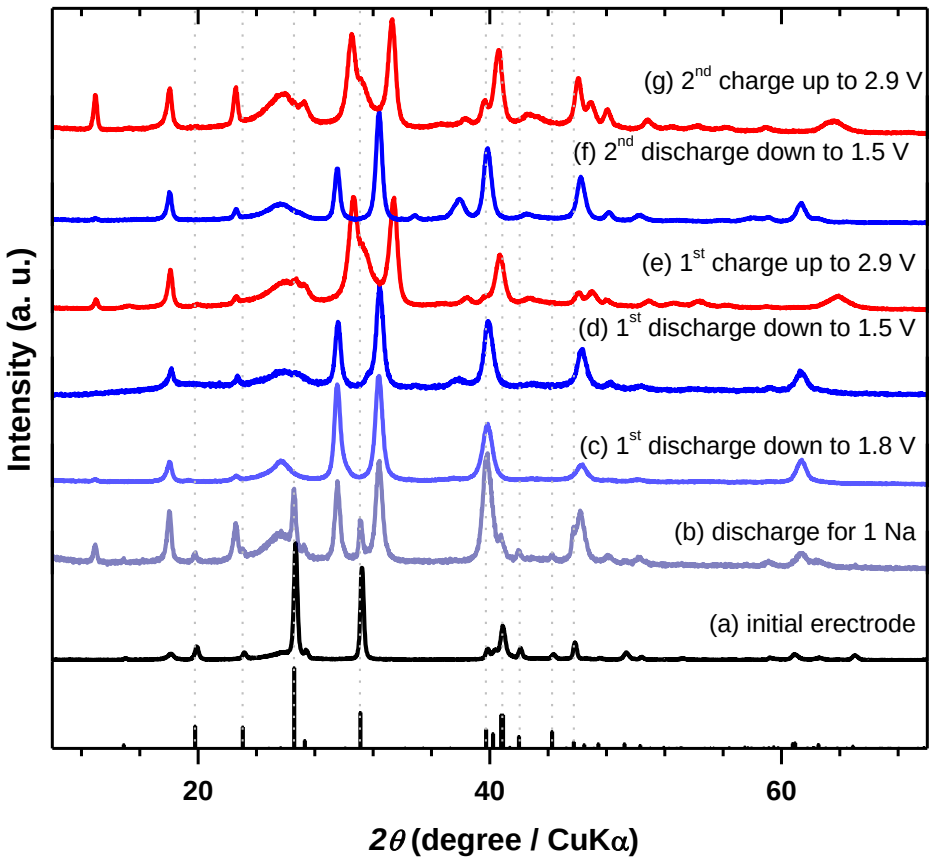

Figure 37. *Ex-situ* XRD patterns of $Na_2C_6O_6$ at the state of (a) initial, (b) discharge for 1 Na^+ insertion, (c) 1st discharge down to 1.8 V, (d) discharge down to 1.5 V, (e) 1st charge up to 2.9 V, (f) 2nd discharge down to 1.5 V and (g) 2nd charge up to 2.9 V.

4.3.2. Local structure change of $Na_2C_6O_6$ during charge and discharge process

FT-IR measurements was performed to observe changes in bond order of C=O in $Na_2C_6O_6$ during charge and discharge processes. Figure 38 shows the results for the $Na_2C_6O_6$ powder and discharged and/or charged $Na_2C_6O_6$ electrodes. In this experiment, base line was adjusted by the background spectrum of AB mixed with PTFE at the mass ratio of 25:5. The pure sample of $Na_2C_6O_6$ and its mixture containing AB and PTFE for the electrode equally showed a strong absorption from 1372 to 1465 cm^{-1}, and weak one

centered at 1062 cm^{-1}. The former absorption may arise from the peripheral six C-O bonds and the latter from the central six-membered C-C bonds. Notably, no significant IR absorption unique to the C=O stretching vibrations was observed. [121-123]. In the spectrum of the electrode sample discharged to 1.5 V, the former absorption (C-O) was shifted to lower energy region at 1372 cm^{-1}, and no significant new peaks appeared. In addition, only small shifts were observed in C-C stretching. X. Wu et al., have investigate the structure evolution accompanied with sodiation in $Na_2C_6H_2O_4$ and performed DFT calculation to propose a new Na storage mechanism in the organic materials. They have indicated that electrochemical phase transition of $Na_2C_6H_2O_6$ can be explained by the localization of π-electrons upon benzene ring in sodiated $Na_2C_6H_2O_4$ structure ($Na_4C_6H_2O_4$). [77] They mentioned that the electron transfer likely occurs at the central six-membered ring without any significant elongation of C=O bonds. However, the peropheral C-O bonds in $Na_2C_6O_6$ got involved and showed elongation in the C=O bond during discharge process on the bases of the FT-IR measurement.

Almost same chemical shifts was observed in the samples after 1st cycle, evidencing that the C-O and C-C bonds in $Na_2C_6O_6$ both accommodated reversible sodiation and desodiation between 1.5 – 2.9 V cycles. The discharge and charge profiles and *ex-situ* XRD patterns for 1st and 2nd cycles were totally different, however the IR spectrum after charge does not indicate an obvious local structure change of $Na_2C_6O_6$. As if the localization of electron injected after sodium insertion in $Na_2C_6O_6$ is not exactly same but close to the observation by X. Wu et al., the benzene rings can be also responsible for the redox reaction in $Na_2C_6O_6$ case. We therefore performed ^{13}C solid NMR of after charge and discharged NaC_6O_6 electrode to investigate change of C state.

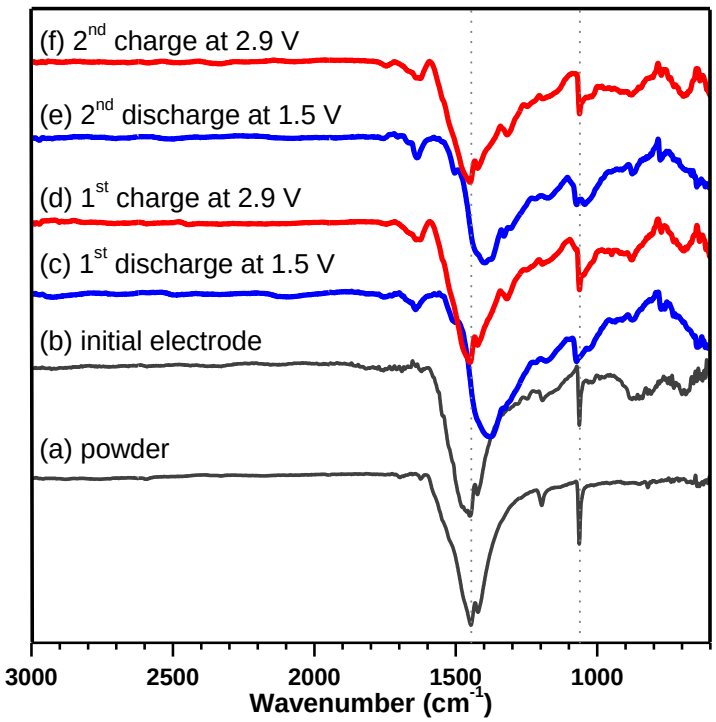

Figure 38. FT-IR peak change behaviors for $Na_2C_6O_6$ at the state of (a) powder, (b) initial (c) 1st discharge down to 1.5 V, (d) 1st charge up to 2.9 V, (e) 2nd discharge down to 1.5 V and (f) 2nd charge up to 2.9 V.

Figure 39 shows ^{13}C solid NMR spectra at room temperature for the $Na_2C_6O_6$ powder and samples of the discharged and charged $Na_2C_6O_6$ electrodes. C in $Na_2C_6O_6$ was located at two 4*a* sites according to the paper previously reported crystal structure refinements [107]. $C_6O_6^{2-}$, is generally written as cycloalkenone structures, however, it is more convenient to take into account resonance oxcarbon anion forms in the crystal structure of $Na_2C_6O_6$, as has already been pointed out by Sprenger et al. for the square case [124]. The Trascon group have also reported on ^{13}C solid NMR spectra in $Li_2C_6O_6$ and assigned C resonance at 175 ppm to C-O-C-O groups and at 180 ppm to carbonyl groups of C=O. [106] In contrast with the previous report on the solid-state ^{13}C NMR for $Li_2C_6O_6$, we

detected three distinct signals at 189, 179 and 175 ppm for the pure sample of $Na_2C_6O_6$. As explained by the Trascon group, 179 and 175 ppm spectra can be assigned to proton eliminated enediols of –C-(O^+)-C-(O^+) forms and the carbonyl group of C=O groups, respectively (inset in Fig. 39). However, the reason for the third peak observed at 189 ppm in the $Na_2C_6O_6$ powder, instead of two, has not been understood clearly. In general, the structure of $Na_2C_6O_6$ can be drawn to have four exocyclic C=O bonds connected with one enediolate unit as an extreme case. Therefore, the observed three peaks may reflect such a structure and two sodium atoms may be situated close to the enediolate unit but distant from any of other C=O bonds. Another possible reason would be the presence of two crystalline form of $Na_2C_6O_6$ as Chalmers et al. reported [125] and thus it could be arise from crystal field effects of twisted molecular $[C_6O_6]^{2-}$ structure or different crystal forms. Two peaks at 179 and 175 ppm, where usually peaks indicate carbonyl groups (180 – 160 ppm), were distinct, while the peaks around 150 ppm which is characteristic of aromatic compounds were not seen. For example, hygroscopic rhodizonic acid showed three signals at 175.0 (C=O) 173.9 (C=O) and 148.9 (C=C) ppm in the liquid state NMR [126]. For a reason of the disappearance of aromatic signals, it would be considered due to the influence from the strong conjugate property of $C_6O_6^{2-}$ and difference of C state in $Na_2C_6O_6$ in solid and liquid. $Na_2C_6O_6$ consists of proton eliminated forms of enediols −C(OH)=C(OH)− with carbonyl group, and dianionic charge is stabilized by resonance structure, and hence $Na_2C_6O_6$ showed strong carbonyl character rather than aromatic character in the solid state. Figure 39 shows the spectrum of electrodes consisting of AB, PTFE and $Na_2C_6O_6$ active materials. The peaks from AB and PTFE appeared from 100 to 120 ppm and they did not overlap with the peak from $Na_2C_6O_6$. The peaks of AB and PTFE were able to be therefore used as an internal standard peak. Peaks for all samples

were too weak and broaden to determine the detailed structure or C state, however some obvious change was observed as appearance of a new signal at 158 ppm. The new broad peak at 158 ppm appeared in the spectrum of the sample discharged down to 1.8 V where approximately 1.5 Na^+ was inserted into $Na_2C_6O_6$, and this peak became shaper and stronger in the sample discharged down to 1.5 V (approximately 1.9 Na^+ was inserted). The original signal from -C-(O^+)-C-(O^+) and C=O disappeared in the sample discharged down to 1.5 V. As mentioned above, usually peaks around 160 - 110 ppm are characteristic of aromatic compounds and especially the signal of oxygen-bonded aromatic compounds (Ar-O) is known to appear at 156 ppm. In addition, Yamashita et al. have proposed a $Na_4C_6O_6$ model stabilized by intermolecular bonding of C_6O_6 bilayer [112], and Wu et al. have also suggested electron localization on benzene ring of $Na_4C_6H_2O_6$ which is electrochemically 2-Na-inserted-form of $Na_2C_6H_2O_6$. [77] Hence, the chemical shift at 158 ppm would originate from electron localization on benzene ring, leading strong aromatic character as a result of loss of conjugated properties of $Na_2C_6O_6$. Electron localization and delocalization in the $C_6O_6^{-x}$ anion deeply involved in discharging process and the obtained ^{13}C NMR result got in a good agreement with the previous calculation result. [77, 112]

Figure 39(e) shows the spectrum of the sample charged up to 2.9 V after discharging down to 1.5 V (1 cycle). The peak around 158 ppm became weaker and broader shape and similar to the spectrum of the sample discharged down to 1.8 V, while the signals from C-O-C-O and C=O appeared again. After 1st cycle, the spectrum changes was almost same as 1st cycle, suggesting the reversibility of $C_6O_6^{-x}$ in $Na_2C_6O_6$. The signal around 189 ppm was not observed after 2nd charge to 2.9 V (Fig. 39(g)), and instead, a signal around 195 ppm was observed. We have not been able to determine that this signal is a

chemical shift of the third peak at 189 ppm or new peaks, and more precise measurement are required to elucidate the behaviors of this peaks. Another new peak was observed around 70 ppm in the sample after 2nd charge to 2.9 V (Fig. 39(g)), and usually the signal for compound with aliphatic carbon appears at around 70 ppm. Hence, theses peaks are supposed to some impurity or decomposition of electrolyte and binder. Combined the results from FT-IR and ^{13}C NMR measurement, reversibility of the $Na_2C_6O_6$ local structures after sodiation and desodiation were confirmed, and in addition, the resonance-stabilized form of the initial $Na_2C_6O_6$ became weaker while the aromatic character of $C_6O_6^{-2-x}$ got more pronounced as increasing in inserted-sodium. We could monitor repeatable de/localization behavior of electrons in the $C_6O_6^{-x}$ anions during charge and discharge process could be monitored by ^{13}C solid NMR measurement. In addition, C-(O^+)-C-(O^+) and C=O signal obviously remained in the electrode discharged 1.8 V (1.5 Na^+ inserted form of $Na_{3.5}C_6O_6$), which was corresponding to the state just after 2.0 V plateau, then these signals disappeared at 1.5 V ($Na_{3.9}C_6O_6$). The difference of inserted sodium amount was only 0.4 Na^+ between the 1.8 V and 1.5 V discharge states. Interestingly, the change of electron localization on $C_6O_6^{-x}$ anion did not gradually occurs, rather evoked after the end of the structure transformation to new phase observed in the *ex-situ* XRD pattern. After 2 phase reaction, the state of C dramatically changed as being inserted Na^+ ions. Since ^{23}Na NMR is an excellent tool of the electronic environment of sodium atom in the study of organometallic compounds [127], ^{23}Na solid NMR was perform in order to investigate change of sodium state after sodiation and desodiation of $Na_2C_6O_6$.

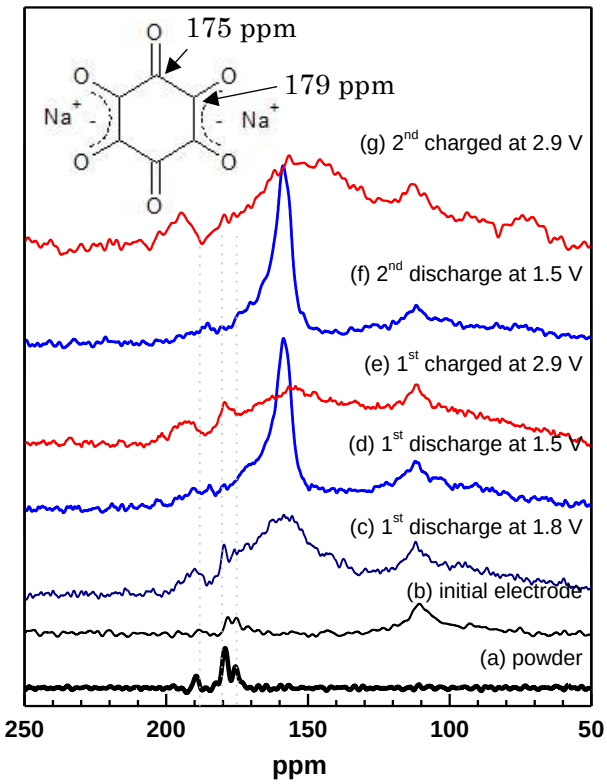

Figure 39. ^{13}C solid NMR spectrum for $Na_2C_6O_6$ at the state of (a) powder, (b) initial, (c) 1st discharge down to 1.8 V, (d) 1st discharge down to 1.5 V, (e) 1st charge up to 2.9 V, (f) 2nd discharge down to 1.5 V and (g) 2nd charge up to 2.9 V. (Inset) peak assignment on $C_6O_6^{2-}$ anion in $Na_2C_6O_6$.

Sodium (^{23}Na) is a spin 3/2 nucleus quadrupolar with medium sensitivity that yields slightly broad lines over a moderate chemical shift range. As a result, the signal width depends on asymmetry of the environment, and thus chemical shift is sensitive to the local environment of the atom of interest. For ^{23}Na nuclei in inorganic solids, correlations between chemical shifts and structural properties including type of neighboring atoms and bond strengths lengths and angles were reported in the literatures, such as correlation of ^{23}Na chemical shifts with a function of bond-strength sum and interatomic distances

[128] and the dynamics of Na diffusion based on number of Na sites [129]. Another studies were also conducted for elucidation of influence from of coordination number, Na-O distance on ^{23}Na chemical shifts, and in the bulk polymerization of sodium silicate. [130]. In the discussion on ^{23}Na in organic materials, A. Wong and G Wu obtained quantitative thermodynamic parameters for Na^+ cations at different sites on surface and in channel from ^{23}Na NMR results and discussed that Na inducted stability of stacking organic materials [131]. However, the reported ^{23}Na chemical shift or observed peak trends are not consistent. The main purpose to use ^{23}Na NMR is usually to determine the presence of sodium or the number of different chemical Na sites and to check for purity or quality, and hence studies have been discussed inconsistently. Regarding ^{23}Na chemical sift behaviors in battery systems, ^{23}Na NMR spectrum change accompanied by Na^+ extraction/insertion has been discussed from the view point of local structural characteristic such as the number of Na sites and ordering/disordering of Na^+ ion and transition metal in a layered tradition metal oxide active material [132-135].

Na^+ ion in the $Na_2C_6O_6$ structure is strongly delocalized, [121, 136, 137] which is required high resonance frequency. We tried solid NMR measurements by using an equipment with 300 - 400 MHz, but none of them brought reliable data except more than 600 MHz. Figure 40 shows ^{23}Na solid NMR spectra of the initial, sodiated and disodiated $Na_2C_6O_6$ electrodes at room temperature. The metal ^{23}Na peak at around 1000 ppm [109] was not observed in all spectra. A relatively sharp symmetric spectrum was seen in the initial sample at around -6 ppm (Figure 40(a)), and hence only one type of site for the Na^+ ions existed in the $Na_2C_6O_6$ structure. As for the spectrum changes in first plateau part at 2.0 V (Fig. 36(II and III)), which were corresponding to 0.25 and 0.5 Na^+ inserted states based on the discharge capacity, the original sharp peak around at -6 ppm decreased in

intensity. On the other hand, a new peak appeared at 270 ppm and continuously increased in discharging process as shown in Fig. 40(b) and (c), suggesting that two identical Na atomic sites existed in the 2.0 V plateau region. Interestingly, for the sample discharged for 1.25 Na, the original peak was completely disappeared and only 57 ppm peak was observed (Fig. 40(d)). These data implied the possibility of existence of stable or meta-stable $Na_{2+x}C_6O_6$ structure which probably has close symmetric structure of $Na_{2+x}C_6O_6$. In addition, the ^{23}Na signal changes well agreed with the observation of the two phase reaction seen in the XRD measurement (Fig. 37). After the 2.0 V plateau region, the signal shifted toward 0 ppm with discharging to deeper voltage of 1.8 V while broadening its shape, which indicated Na^+ ion might be affected by shielding effect from the surrounded environment to become more randomized or static with deeper discharge. To investigate the Na^+ ion site in the 1.8 V discharged state, we performed MQMAS NMR and the result will be discussed later. The spectrum of the sample discharged down to 1.5 V was a broad peak over -25 to 50 ppm. Although there was no big difference was observed in the lattice change based on the *ex-situ* XRD profile, the Na^+ ion state dramatically changed during discharge between 1.8 V and 1.5 V where approximately 0.5 Na^+ was inserted into the structure. In the case of the sample continually discharged down to 1.0 V, its spectrum shifted toward to 0 ppm and symmetric property of the signal was reduced.

The spectrum of the sample cycled between 1.5 – 2.9 V could be divided into two parts (Fig.40(g)); one was a sharp spectrum at near 0 ppm and the other was broad one at ~ 100 ppm. The peak near 0 ppm was also able to explain the structure change during charge where the sodiated $Na_{2+x}C_6O_6$ structure partially returned to the original phase. The broad peak ~ 100 ppm could not be distinguished as sites but probably it was caused by the anisotropic and/or asymmetric state of sodium ions. From the 2nd cycle, the almost same

chemical shift was observed, evidencing the reversibility of the Na^+ insertion/extraction process.

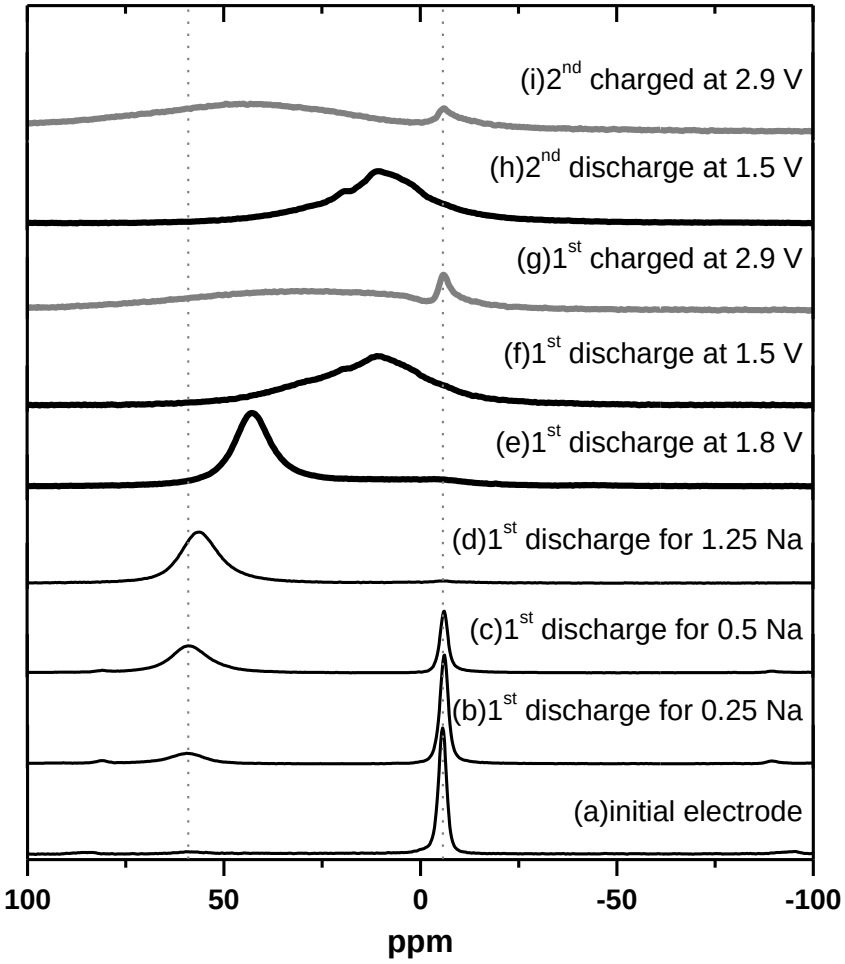

Figure 40. ^{23}Na solid NMR spectrum for $Na_2C_6O_6$ at the state of (a) initial, (b) discharge for 0.25 Na^+ insertion, (c) discharge for 0.5 Na^+ insertion (d) discharge for 1.25 Na^+ insertion, (e) 1st discharge down to 1.8 V, (f) 1st discharge down to 1.5 V, (g) 1st charge up to 2.9 V, (h) 2nd discharge down to 1.5 V and (i) 2nd charge up to 2.9 V.

To discuss more details of the sodium ion site, we performed MQMAS NMR and Fig. 41 shows the spectrum for the $Na_2C_6O_6$ samples which were discharged for 1.25 Na (Fig.

41 (a)) and 1.5 V (Fig. 41 (b)). Although only one peak was observed in the MAS NMR measurement in the sample discharged for 1.25 Na (Fig. 40(e)), 3 identical peaks were seen at -5.5 ppm, 5.4 ppm and 55.1 ppm in the MQMAS spectrum (Fig 41(a)). To investigate the difference in the results from MAS and MQMAS, we checked the time degradation of the discharged $Na_2C_6O_6$ sample. The sample were prepared as follows; after disassembling the cells and washing the electrode, the sample was (1) measured immediately in Ar condition within 20 minute from sample preparation to end of measurement, (2) left for 1, 2 and 3 week(s) in Ar glove box and measured in Ar condition, or (3) exposed in the air and measured in Air condition. Figure 42 shows MAS spectra of each $Na_2C_6O_6$ electrode samples described above. As shown in Fig. 42, intensity of the peaks at -5.5 ppm, 5.4 ppm became stronger as being left longer in Ar glove box, and the peak at 55.1 ppm totally disappeared in the sample exposed to the air. The peaks at -5.5 ppm, 5.4 ppm in MQMAS measurement were therefore attributed to sample degradation by CO_2, O_2, H_2O or other gas left in glove box. Thus, when the sample was discharged for 1.25 Na, we concluded that Na took one site or at least signal at 55.1 ppm originates from one sodium condition. On the other hand when the material was discharged down to 1.5 V, at least 3 identical peaks were observed suggesting the Na^+ ions took more than two states and symmetric property of the structure become more random after the 2 phase transformation. As considered with the result of ^{13}C NMR and *ex-situ* XRD, the conjugate property of $Na_{2+x}C_6O_6$ became rather aromatic property during 1.8 – 1.5 V discharge after two phase transformation ($x > 1.5$ in $Na_{2+x}C_6O_6$), and the structural symmetric in the crystal of $Na_{2+x}C_6O_6$ was decreased as result of electron delocalization on $C_6O_6^{x-}$ anion and localization or randomization of Na^+, which was observed as a step discharge profile between 1.8 to 1.5 V.

(a) (b)

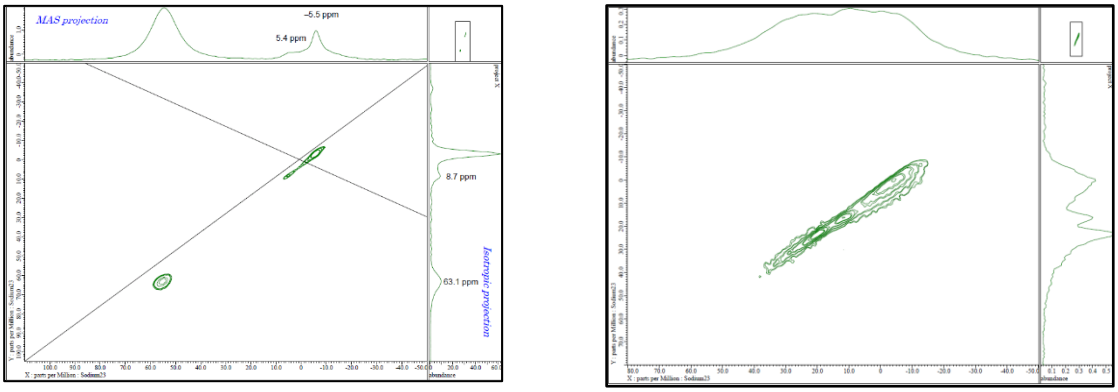

Figure 41. ^{23}Na MQMAS NMR spectrum for the $Na_2C_6O_6$ samples after being discharged for (a) 1.25 Na and down to (b) 1.5 V.

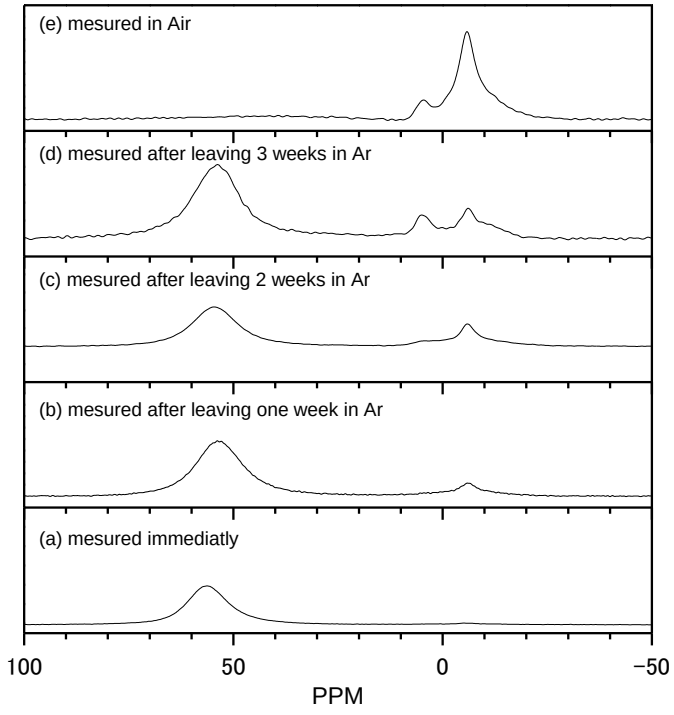

Figure 42. ^{23}Na NMR spectrum of discharged $Na_2C_6O_6$ sample for 1.25 Na. The sample was (a) measured immediately after dissembling a cell, and left for (b) 1, (c) 2 and (c) 3 week in Ar glove box and measured in Ar condition, and (e) exposed in the air and measured in Air condition.

4.4. Conclusion

Structural change of $Na_2C_6O_6$-based electrode was investigated using X-ray powder diffraction (XRD), Fourier transform infrared spectroscopy (FT-IR) and Solid state 23Na and 13C nuclear magnetic resonance (NMR). *Ex-situ* XRD data revealed that $Na_2C_6O_6$ first went through two-phase transformation reaction during the discharge down to 1.8 V, after which the charge and discharge reaction can be carried out by Na^+ insertion/extraction reaction in to the new structure. FT-IR and ^{13}C and ^{23}Na solid NMR studies suggested that discharging process proceeded with change of electron localization of $C_6O_6^{-x}$ rather than C=O group, leading enhancement in aromatic property from conjugated property of $Na_2C_6O_6$. In addition, those data provided evidence for repeatable charge and discharge process by monitoring the state at 1^{st} and 2^{nd} cycles. Overall, all data including charge and discharge profiles were well compromised each other.

Reference

[1] *M. S. Whittingham, Science., **192,** 4244 (1976) 1126.*

[2] K. Mizushima, P. C. Jones, P. J.Wiseman, J. B. Goodenough, *Mater. Res. Bull.* **15**, 6 (1980) 783.

[3] N.A. Godshall, *Solid State Ionics* **18-19**, 2, (1986) 788.

[4] *M. M. Thackeray, W. I. F.* David, *P. G. Bruce, J. B. Goodenough, Mater. Res. Bull., **18**, 4 (1983) 461.*

[5] *R. Yazami, P. Touzain, J. Power Sources, **9**, 3 (1983) 365.*

[6] US patent No.4668595, Yoshino; Akira, issued 10 May 1985, assigned to Asahi Kasei.

[7] T. B. Reddy , D. Linden , Linden's Handbook of Batteries, McGraw-Hill , 2010 (Book).

[8] M. D. Slater , D. Kim , E. Lee , C. S. Johnson, *Adv. Func. Mater.,* **23** 8 (review) (2012).

[9] C. Delmas, C. Fouassier, P. Hagenmuller, *Physica B C*, **99** (1980) 81.

[10] T. Shishikura, M. Takeuchi, Secondary batteries, ShowaDenko, K. K. Hitachi, Ltd., Japan (1987).

[11] K. Kubota, S. Komaba, *J. Electrochem. Soc.*, **162** (2015) A2538.

[12] D. A. Stevens, J. R. Dahn, *J. Electrochem. Soc*., **148** (2001), A803.

[13] A. K. Padhi, K. S. Nanjundaswamy, J. B. Goodenough, *J. Electrochem. Soc.*, **144**, 4 (1997) 1188.

[14] J. J. Braconnier, C. Delmas, C. Fouassier, P. Hagenmuller, *Mater. Res. Bull.*, **15 (**1980) 1797.

[15] C. Delmas, J.-J. Braconnier, C. Fouassier, P. Hagenmuller, *Solid State Ionics*, **3/4** (1981) 381.

[16] J. M. Paulsen, J. R. Dahn, *Solid State Ionics*, **126**, (1999), 3.

[17] R. Stoyanova, D. Carlier, M. Sendova-Vassileva, M. Yoncheva, E. Zhecheva, D. Nihtianova, C. Delmas, *J. Solid State Chem.*, **183** (2010) 1372.

[18] N. Yabuuchi, S. Komaba, *Science and Technology of Advanced Materials*, Review, (2014).

[19] S. Kumakura, Y. Tahara, K. Kubota, K. Chihara, S. Komaba, *Angew. Chem. Int.*

Ed. **55** (2016) 12760.

[20] L. Wang, T. Maxisch, G. Ceder, *Chem. Mater.*, **19 (**2007) 543.

[21] Y. Baba, S. Okada, J. Yamaki, *Solid State Ionics*, **148**, 3–4 (2002) 311.

[22] A. S. Andersson, J. O. Thomas, B. Kalska, L. Häggström, Electrochem. Solid-State Lett., **3**, 2 (2000) 66.

[23] M. S. Islam, D. J. Driscoll, C. A. J. Fisher, P. R. Slater, *Chem. Mater.*, **17** (2005) 5085.

[24] A. Sun, A. Manivannan, *ECS Transactions*, **35,** 32 (2011) 3.

[25] A. Whiteside, C. A. Fisher, S. C. Park, M. S. Islam, *Phys. Chem. Chem. Phys*., **16** (2014) 21788.

[26] S.-Min Oh, S.-Taek Myung, J. Hassoun, B. Scrosati Y.-Kook Sun, *Electrochem. Comm.*, **22** (2012) 149.

[27] K. Zaghib, J. Trottier, P. Hovington, F. Brochu, A. Guerfi, A. Mauger, C. M. Julien, *J. Power Sources*, **196** (2011) 9612.

[28] G. Ali, J.-H. Lee, D. Susanto, S.-W. Choi, B. W. Cho, K.-W. Nam, K. Y. Chung, *ACS Appl. Mater. Interfaces*, **8** (2016) 15422.

[29] J. N. Reimer, J. R. Dahn, *J. Electrochem. Soc.*, **139** (1992) 2091.

[30] J. Kim, D.-Hwa Seo, H. Kim, I. Park, J.-Keunoo, S.-Kyun Jung, Y.-Uk Park, W. A. Goddard III, and K. Kang, *Energy Environ. Sci.*, **8** (2015) 540.

[31] H. Yaghoobnejad, A. Choudhury, *RSC Adv.*, **4 (**2014) 37691.

[32] N. Recham, J.N. Chotard, L. Dupont, K. Djellab, M. Armand, J.M. Tarascon, *J. Electrochem. Soc.*, 156 (2009) A993.

[33] B. L. Ellis, W. R. M. Makahnouk, W. N. R.Weetaluktuk, D. H. Ryan, L. F. Nazar, *Chem. Mater.*, **22**, 3 (2010) 1059.

[34] R. Triphthi, S. M. Wood, M. S. Islam, L. F. Nazar, *Energy Environ. Sci.*, **6** (2013) 2257.

[35] Y. Kawabe, N. Yabuuchi, M. Kajiyama, N. Fukuhara, T. Inamasu, R. Okuyama, I. Nakai, S. Komaba, *Electrochem. Comm.* **13** (2011) 1225.

[36] A. K. Padhi, K. S. Nanjundaswamy, C. Masquelier, S. Okada, J. B. Goodenough, *J. Electrochem. Soc.*, **144**, 5 (1997) 1609.

[37] W. Yuan, J. Yan, Z. Tang, L. Ma, *Ionics*, **18** (2012) 329.

[38] W. Yuan, J. Yan, Z. Tang, O. Sha, J. Wang, W. Mao, L. Ma, *J. Power Sources*, **201** (2012) 301.

[39] T. Jiang, W. Pan, J. Wang, X. Bie, F. Du, Y. Wei, C. Wang, G. Chen, *Electrochim. Acta*, **55** (2010) 3864.

[40] S.-C. Yin, H. Grondey, P. Strobel, M. Anne, L. F. Nazar, *J. Am, Chem. Soc.*, **125** (2003) 10402.

[41] X. Rui, Q. Yan, M. S. Kazacos, T. M. Lim, *J. Power Sources*, **258** 15 (2014) 19.

[42] J. Gopalakrishnan, K. Kasthuri Rangan, *Chem. Mater.*, **4**, 4 (1992) 745.

[43] C. Masquelier, S. Patoux, C. Wurm, M. Morcrette, Lithium Batteries: Science and Technology, Editors: Gholam-Abbas Nazri, Gianfranco Pistoia, (2003) 445.

[44] Z. Jian, L. Zhao, H. Pan, Y.-S. Hu, H. Li, W. Chen, L. Chen, *Electrochem. Commun.*, 14 (2012) 86.

[45] L. S. Plashnitsa, E. Kobayashi, Y. Noguchi, S. Okada, J.-I. Yamaki, *J. Electrochem. Soc.*, **157** (2010) A536.

[46] K. Saravanan, C. W. Mason, A. Rudola, K. H. Wong, P. Balaya, *Adv. Energy Mater.*, **3** (2013) 444.

[47] J. Barker, M. Y. Saidi, J. L. Swoyer, *Electrochem. Solid-State Lett.* **6** (2003) A1.

[48] J. Barker, M. Y. Saidi, J. L. Swoyer, *J. Electrochem. Soc.*, **151** 10 (2004) A1670.

[49] J.-M. Le Meins, M.-P. Crosnier-Lopez, A. Hemon-Ribaud, G. Courbion, *J. Solid State Chem.*, **148** (1999) 260.

[50] F. Sauvage, E. Quarez, J.-M. Tarascon, E. Baudrin, Solid-State Science, **8** (2006) 1215.

[51] Y.-U. Park, D.-H. Seo, H.-S. Kwon, B. Kim, J. Kim,.H. Kim, I. Kim, H.-Ill Yoo, K. Kang, *J. Am. Chem. Soc.*, **135** (2013) 9 13870.

[52] J. Song, M. Xu, L. Wang, J. B. Goodenough, *Chem. Comm.*, **49** (2013) 5280.

[53] G. He, A. Huq, W. H. Kan, A. Manthiram, *Chem. Mater.*, **28** (2016) 1503.

[54] B. M. Azmi, T. Ishihara, H. Nishiguchi, Y. Takita, *J. Power Sources,* **146** (2005) 525.

[55] C. J. Allen, Q. Jia, C. N. Chinnasamy, S. Mukerjee, K. M. Abraham, *J. Electrochem. Soc.*, **158** (2011) A1250.

[56] D. Macinnes, M. A. Druy, P. J. Nigrey, D. P. Nairns, A. G. MacDiarmid, A. J. Heeger, *J. Chem. Soc., Chem. Commun.,* **7** (1981) 17.

[57] M. L. Liu, S. J. Visco, L. C. Dejonghe, *J. Electrochem. Soc.,* **138**, 7 (1991) 1891.

[58] N. Oyama, T. Tatsuma, T. Sato, T. Sotomura, *Nature,* **373**, 6515 (1995) 598.

[59] X. Y. Han, C. X. Chang, L. J. Yuan, T. L. Sun, J. T. Sun, **19**, 12 (2007) 1616.

[60] J. Y. Zhang, L. B. Kong, L. Z. Zhan, J. Tang, H. Zhan, Y. H. Zhou, *J. Power Sources*, **168**, (2007) 278.

[61] K. Nakahara, S. Iwasa, M. Satoh, Y. Morioka, J. Iriyama, M. Suguro, E. Hasegawa, *Chem. Phys. Lett.*, **359** (2002) 351.

[62] K. Nakahara, J. Iriyama, S. Iwasa, M. Suguro, M. Satoh, E. J. Cairns, *J. Power Sources*, **165**, (2007) 398.

[63] M. Armand, S. Grugeon, H. Vezin, S. Laruelle, P. Ribière, P. Poizot, J.-M. Tarascon, *Nature Mater.*, **8** (2009) 120.

[64] L. Zhao, J. Zhao, Y.-S. Hu, H. Li, Z. Zhou, M. Armand, L. Chen, *Adv. Energy Mater.*, **2 (**2012) 962.

[65] Y. Park, D. S. Shin, S. H. Woo, N. S. Choi, K. H. Shin, S. M. Oh, K. T. Lee, S. Y. Hong, *Adv Mater.,* **24**, 26 (2012) 3562.

[66] K. Chihara, N. Chujo, A. Kitajou, S. Okada, *Electrochimica. Acta*, **110** (2013) 240.

[67] A. Choi, Y.K. Kim, T.K. Kim, M.-S. Kwon, K.T. Lee, H.R. Moon, *J. Mater. Chem. A,* **2** (2014) 14986.

[68] V.A. Mihali,; S. Renault,; L. Nyholm,; D. Brandell, *RSC Adv.*, **4** (2014) 38004.

[69] K. Chihara, S. Kuze, T. Yamaguchi, A. Kitajou, S. Okada 64th Annual Meeting of the International Society of Electrochemistry (ISE) (2013).

[70] C. Luo,; Y. Zhu,; Y. Xu,; Y. Liu,; T. Gao,; J. Wang,; C. Wang, *J. Power Sources*, **250** (2014) 372.

[71] K. Chihara, M. Ito, A. Kitajou, and S. Okada, submitted to *Evergreen*

[72] M. Yao, K. Kuratani, T. Kojima, N. Takeichi, H. Senoh, T. Kiyobayashi, *Sci. Rep.*, **4** (2014) 3650.

[73] S. Renault, V.A. Mihali, K. Edström, D.Brandell, *Electrochem. Commun.*, **45** (2014) 52.

[74] S.Wang, L. Wang, Z.Zhu, Z. Hu, Q. Zhao, J.Chen, *Angew. Chem. Int. Ed.* **53** (2014) 5892.

[75] C. Guo, K. Zhang, Q. Zhao, L. Pei, J. Chen, *Chem. Commun.*, **51** (2015)10244.

[76] Z. Zhu, H. Li, J. Liang, Z. Tao, J. Chen, *Chem. Commun.*, **51** (2015) 1446.

[77] X. Wu, S. Jin, Z. Zhang,; L. Jiang, L. Mu,; Y.-S. Hu, H. Li,; X. Chen, M .Armand, L. Chen, *Sci. Adv.* **1** (2015) e1500330.

[78] A. Abouimrane, W. Weng, H. Eltayeb, Y. Cui, J. Niklas, O. Poluektov and K. Amine, *Energy Environ. Sci*., **5** (2012) 9632.

[79] W. Deng, J. Qian, Y. Cao, X. Ai and H. Yang, *Small*, **12** (2016) 583.

[80] V. A. Oltean, S. R., M. Valvo, D. Brandell, *Materials, Review*, **9**, 142 (2016).

[81] T. A. Kerr, J. Gaubicher, L. F. Nazarz, *Electrochem. Solid-State Lett.*, 3, (2000) 460.

[82] J. Gaubicher, T. L. Mercier, Y. Chabre, J. Angenault, M. Quartona, *J. Electrochem. Soc.*, **146** (1999), 4375.

[83] B. M. Azmi, T. Ishihara, H. Nishiguchi, Y. Takita, *J. Power Sources*, **273** (2003) 119.

[84] J. Barker, M. Y. Saidi, J. L. Swoyer, *J. Electrochem. Soc.*, **151**, (2004) A796.

[85] M.M. Ren, Z. Zhou, L.W. Su, X.P. Gao, *J. Power Sources*, **189**, 1, (2009) 786.

[86] N. Dupre, J. Gaubicher, T.L. Mercier, G. Wallez, J. Angenault, M. Quarton, *Solid State Ionics*, **140** (2001) 209.

[87] A. K. Padhi, V. Manivannan, J. B. Goodenough, *J. Electrochem. Soc*., 1998, 145, 5, 1518.

[88] J. Li, H. Zhan, L. Zhou, S. Deng, Z. Li, Y. Zhou, *Electrochem. Commun.*, **6**, (2004) 515.

[89] N. Yabuuchi, H. S.Yoshida, Komaba, *Electrochem.*, **80**, 10, (2012) 716.

[90] S. Komaba, N. Yabuuchi, T. Nakayama, A. Ogata, T. Ishikawa, I. Nakai, *Inorg. Chem.*, **51**, 11, (2012) 6211.

[91] R. Berthelot, D. Carlier, andC. Delmas, *Nature Materials*, **10** (2011) 74.

[92] Z. H. Lu andJ. R. Dahn, *J. Electrochem. Soc.*, **148** (7) (2001) A710.

[93] Zhao, J. Zhao, L. W. Dimov, N. Okada, S. Nishida, *J. Electrochem. Soc.*, **160**, 5, (2013) A3077.

[94] J. M. L. Meins, M. P. Crosnier-Lopez, A. H. Ribaud, G. Courbion, *J. Solid State Chem.* **148** (1999) 260.

[95] J Barker - US Patent 6,890,686, (2005)

[96] 智原 久仁子, 中本 康介, Irina D Gocheva, 岡田 重人, 山木 準一, 第52回電池討論会, (2011).

[97] G. Kresse, J. Furthmuller, *Phys. Rev. B*, **54**, 16 (1996) 11169.

[98] P.E. Blochl, *Phys. Rev. B*, **50**, 24 (1994) 17953-17979.

[99] G. Kresse, D. Joubert, *Phys. Rev. B*, **59**, 3 (1999) 1758.

[100] J.P. Perdew, K. Burke, *Phys. Rev. Lett.* **77,** 18 (1996) 3865.

[101] M. Bianchini, N. Brisset, F. Fauth, F. Weill, E. Elkaim, E. uard, C. Masquelier, L. Croguennec, *Chem. Mater.*, **26** (2014) 4238.

[102] G. T. K. Fey, T. L. Lu, F. Y. Wu, W. H. Li, *J. Solid State Electrochem.*, **12,** 7-8 (2008) 825.

[103] T. Kikuchi, K. Kurakane, T. Yamamoto, T. Hattori, M. Makidera, Japan Patent Kokai 2009-135074 (18.06.2009).

[104] C. Delmas, F. Cherkaoui, A. Nadiri and P. Hagenmuller, *C. Mat. Res. Bull.*, **22** (1987) 631-639.

[105] S. Il Parka, I. Gochevab, S. Okadaa, J. Yamakib, *J. Electrochem. Soc.*, **158**, 10 (2011) A1067.

[106] H. Chen, M. Armand, G. Demailly, F. Dolhem, P. Poizot, J.-M. Tarascon, *Chem. Sus. Chem.* **1** (2008) 348.

[107] R.-E. Dinnebier, H. Nuss, M. Jansen, *Acta Crystallographica*, **E61** (2005) 2148.

[108] P. Thomas, D. Billaud, *Electrochim. Acta*, **47** (2002) 3303.

[109] K. Gotoh, T. Ishikawa, S. Shimadzu, N. Yabuuchi, S. Komaba, K. Takeda, A. Goto, K. Deguchi, S. Ohki, K. Hashi, T. Shimizu, H. Ishida, *J. Power Sources*, **225** (2013) 137.

[110] N. Chujo, K. Chihara, S. Okada, S. Kuze, Japan patent JP2013-229321A.

[111] J.-S. Bridel, T. Azaïs, M. Morcrette, J.-M. Tarascon, D. Larcher, *Chem. Mater.*, **22**, 3 (2010) 1229.

[112] Yamashita

[113] H. S. Lee, X. Q. Yang, C. L. Xiang, J. McBereen, *J. Electrochem. Soc.*, **145** (1998), A1460.

[114] *Oxocarbons*, ed. R. West, Academic Press, New York, (1980).

[115] R. West, J. Niu, in *The Chemistry of the Carbonyl Group*, ed. J. Zabicky, Interscience, London 1970, vol. II, ch.4 (doi:10.1002/ 9780470771228.ch4).

[116] F. Sarratosa, *Acc. Chem. Res.*, **16**, (1983) 170.

[117] G. Seitz, P. Imming, *Chem. Rev.*, **92**, (1992) 1227.

[118] Q. Zhao, J. Wang, Y. Lu, Y. Li, G. Liang, J. Chen, *Angew. Chem. Int. Ed.*, **55**, (2016) 12528.

[119] S. Kikkawa, S. Miyazaki, M. Koizumi, J. Solid State Chem., **62**, 1, (1986) 35.

[120] P. v. R. Schleyer, K. Najafian; B. Kiran, H. Jiao, *J. Org. Chem*., **65** (2000) 426.

[121] J. Coates, Interpretation of Infrared Spectra, A Practical Approach, in Analytical Chemistry, R.A. Meyers, Ed., ed. Chichester: John Wiley & Sons Ltd, (2000) 10815.

[122] R. T. Bailey, *J. Chem. Soc. B*, (1971) 627.

[123] M. Takahashi, K. Kaya, M. Ito, *Chem. Phys.*, **35**, 3, (1978) 293.

[124] H. E. Sprenger, W. Ziegenbe, *Angew. Chem. Int. Ed.*, **7**, 7 (1968) 583.

[125] R. A. Chalmers, G. M. Telling, *Mikrochim. Acta*, **6**, (1967) 1126.

[126] W. Stadeli, R. Hollenstein, W. V. Philipsborn, *Helv. Chim. Acta*, **60**, 3 (1977) 948.

[127] J. M. Willans, R. W. Schurko, *J. Phys. Chem. B*, **107** (2003) 5144.

[128] H. Koller, G. Engelhardt, A. P. M. Kentgens, J. Sauer, *J. Phys. Chem.*, **98**, 6 (1994) 1544.

[129] J.F. Stebbins, J.B. Murdoch, E. Schneider, I.S. Carmichael, A. Pines, *Nature*,

314 (1985) 250.

[130] X. Xue, J.F. Stebbins, *Phys. Chem. Minerals,* **20** (1993) 297.

[131] A. Wong, G. Wu, *J. Am. Chem. Soc.,* **125** (2003) 13895.

[132] R. Siegel, J. Hirschinger, D. Carlier, M. Menetrier, C. Delmas, *Solid State Nucl. Mag*., **23**, 4 (2003) 243.

[133] J. Cabana, N. A. Chernova, J. Xiao, M. Roppolo, K. A. Aldi, M. S. Whittingham, C. P. Grey, *Inorg. Chem.*, **52**, 15 (2013) 8540.

[134] I. R. Mukhamedshin, H. Alloul, G. Collin, N. Blanchard, *Phys. Rev. Lett.*, **93**, 16 (2004) 7601.

[135] P. Stallworth, S. Greenbaum, Y. Ma, L. Ding, M. Doeff, S. Visco, *Solid State Ion.*, **86**, 8 (1996) 797.

[136] R. West, H.Y. Niu, D. L. Powell, M. V. Evans, *J. Am. Chem. Soc.*, **82**, 23, (1960) 6204.

[137] A. Moyano, F. Serratosa, *J. Mol. Struct. (Theochem)*, **7**, 1-2, (1982) 131.

Chapter 5 General conclusions

The application fields of LIBs have been expanding to larger scale devises such as electric vehicles (EVs) and a smart grid system utilizing renewable and sustainable green energies. As a result, the increasing demand for lithium associated with new and large-scale applications leads future concern on the price of lithium and even political conflict rerated to lithium reserves. Rechargeable SIBs have been, therefore, aggressively studied for past few years and considered as an alternative candidate to LIBs due to the abundant reserve and even-distribution of Na resources. The SIBs would provide minor-metal-free cathode material, leading achievement of ecofriendly and inexpensive battery system.

The main propose of this thesis was search for new cathode materials for SIBs including inorganic and organic compounds, and inorganic materials of $Na_3V_2(PO_4)_2F_3$, and organic materials of $Na_2C_6O_6$ and $Na_2C_5O_5$ can be considered the potential candidate for the active materials for SIBs. Here, the conclusions in each chapter are summarized as follows.

In chapter 2, $Na_3M_2(PO_4)_2F_3$ [M = Ti, V, and Fe] were obtained by the solid state reaction and their electrochemical performance was evaluated in Na cells. Since $Na_3V_2(PO_4)_2F_3$ showed excellent cathode properties in Na cells, further investigation was carried out in Na-ion full cells. $Na_3M_2(PO_4)_2F_3$. $Na_3V_2(PO_4)_2F_3$ showed the large rechargeable capacity of 120 mAh g^{-1}, which corresponds to the capacity from 2 Na^+ extraction/insertion reaction with two-step discharge voltage plateaus at 4.1 V and 3.6 V in 4.3– 2.3 V and 4.6 2.3 V. It also showed good cyclability even between 2.3 V and 4.6 V and the discharge capacity at the 40^{th} cycle was 115.12 mAh g^{-1} corresponding to 94% from the initial discharge capacity. These performance were confirmed in Na half- and Na-ion full cells configuration. In addition, our structural study confirmed that $Na_3V_2(PO_4)_2F_3$ has the

structure capable enough to accommodate large sodium extraction and insertion with extension and shrinkage along with *c*-axis. The result obtained in this research suggest strong possibility of $Na_3V_2(PO_4)_2F_3$ as a cathode material for SIBs.

Organic compounds have received less attention as potential active materials in LIBs due to its low conductivity and large volume density. However, given the new requirements in the development of SIBs, such as low production costs and structure limitation for large sodium ions, organic compounds have several advantages, including multiple electron reaction, their chemical diversity, layer staking structure, and cost-effective aspects. In order to explore new host materials for SIBs, oxcarbon-based compounds were focused and $Na_2C_xO_x$ [x = 4, 5, and 6] and $K_2C_6O_6$ were selected as target active materials in Chapter 3. Among them, $Na_2C_6O_6$ and $Na_2C_5O_5$ exhibit stable charge and discharge cycles with ca. 200 mAh g^{-1} and $Na_2C_xO_x$ was able to function in Na-ion cells with Na-predoped hard carbon anode. In addition, $Na_2C_6O_6$ possessed extremely good conductivity which is rale as organic compound, achieving good rate performance under 5C rate.

In chapter 4, crystal and local structure change of $Na_2C_6O_6$ were investigated by using XRD, FT-IR, and ^{13}C and ^{23}Na solid NMR. *Ex-site* XRD data revealed that $Na_2C_6O_6$ first went through two-phase transformation reaction during the discharge down to 1.8 V, after which the charge and discharge reaction can be carried out by Na^+ insertion/extraction reaction in to the new structure. Result from FT-IR and ^{13}C and ^{23}Na solid NMR suggested that discharging process was carried out by electron localization on $C_6O_6^{-x}$ rather than C=O group reactivity, leading enhancement in aromatic property from conjugated property of $Na_2C_6O_6$. In addition, those data provided evidence for repeatable charge and discharge process by monitoring the state at 1st and 2nd cycles. Overall, all data including

charge and discharge profiles were well compromised each other.

Acknowledgments

First, I would like to express my special appreciation and respect to my advisor, Prof. Shigeto Okada. Thank all for his advises, support, effect and passion, which always lead me to carry on the thesis. I would also like to thank Pro. Masato Ito. He gave many advice and suggestion especially on the research of organic active materials, and his ideas inspired me to open new concept on the material designing. I would like to express my heartfelt gratitude for prof. Yoon, prof. Tanaka, and prof. Ito in Kyushu University who kindly supported to finalize my thesis as co-research advisors. Their technical and academic advices have drown out the better publication. I would also like to extend my appreciation to Okada group's staff and students. I especially to thank Dr. Ayuko Kitajyo and Mr. Kousuke Nakamoto for discussion and their kind comments and help to motivate me to carry out this thesis.

I also deeply appreciated the technical support and advices from Ms. Keiko Ideta in Kyushu University who is the skillful specialist of solid NMR

Special thanks are also extended to Prof. Ying Shirley Meng of University of California San Diego and her students Mr. Chuze Ma and Ms. Judith Alvarado for their comments and help during my internship.

Finally, a special thanks to my family, my parents and especially, my husband. Without his support, I had never be able to accomplish my thesis. Thousands of thanks to all of them.

February, 2016 Kuniko Chihara